博士論文

Data-driven study on abrupt termination events in fusion plasmas
（核融合プラズマの突発的崩壊現象に関するデータ駆動型研究）

横山 達也

Contents

List of Tables

List of Figures

Chapter 1

Introduction

1.1 Nuclear fusion energy

1.1.1 Nuclear fusion

Nuclear fusion is one of advanced energy sources and has been being continuously studied towards practical use of it as an electrical source. It is the process in which multiple light nuclei are combined to be a heavy nucleus. The deuterium-tritium (DT) reaction, which is shown in the following equation, is thought to be the most effective fusion reaction for the use of fusion energy on the earth.

$$\mathrm{D} + \mathrm{T} \longrightarrow {}^{4}\mathrm{He}(3.52\,\mathrm{MeV}) + \mathrm{n}(14.06\,\mathrm{MeV}). \tag{1.1}$$

The product of the DT reaction is a helium4 (${}^{4}\mathrm{He}$) nucleus and a neutron (n). It is known that the fusion reactivity $\langle \sigma v \rangle$ is a function of temperature. The reactivity of DT reaction has a peak at nearly 50 keV and takes higher value around 10 keV than other candidate fusion reaction such as deuterium-deuterium reaction and deuterium-helium3 reactions. Here, σ and v are reaction cross section and relative velocity of ions, respectively. Therefore, extremely high-temperature plasma in the order of 10 keV is necessary to utilize fusion energy.

Here, energy confinement is an important concept for nuclear fusion in magnetic confinement plasma. Assume the plasma consisting of the 50-50 mixture of deuterium and tritium. Thermal energy of the plasma per unit volume W_p is described as following equation, where n, T_i and T_e are plasma density, ion temperature, and electron temperature. Note that the temperatures are in units of energy, eV.

$$W_\mathrm{p} = \frac{3}{2} n (T_\mathrm{i} + T_\mathrm{e}). \tag{1.2}$$

Plasma energy confinement time τ_{E} is defined as

$$\tau_{\mathrm{E}} \equiv \frac{W_{\mathrm{p}}}{P_{\mathrm{loss}}} \approx \frac{3nT}{P_{\mathrm{loss}}}, \tag{1.3}$$

where P_{loss} is energy loss per unit volume and unit time, and $T_{\mathrm{i}} = T_{\mathrm{e}} = T$ is assumed.

In one DT reaction, an alpha particle that has $Q_\alpha = 3.52\,\mathrm{MeV}$ and an neutron that has $Q_{\mathrm{n}} = 14.06\,\mathrm{MeV}$ are created. Since the created alpha particles are charged, they remain in the plasma and heat electrons and ions by Coulomb collision. The heating power by alpha particle per unit volume is denoted as $P_\alpha = n_{\mathrm{D}} n_{\mathrm{T}} \langle \sigma v \rangle Q_\alpha$, where n_{D} and n_{T} are density of deuterium and tritium ions. By the assumption that the density of deuterium and tritium is equal to each other, i.e., $n_{\mathrm{D}} = n_{\mathrm{T}} = n/2$, P_α is denoted as follows:

$$P_\alpha = \frac{n^2}{4} \langle \sigma v \rangle Q_\alpha. \tag{1.4}$$

To sustain fusion reaction without any external input power, $P_\alpha \geq P_{\mathrm{loss}}$ is required. Therefore, the following conditional expression is derived:

$$n\tau_{\mathrm{E}} \geq \frac{12T}{\langle \sigma v \rangle Q_\alpha}. \tag{1.5}$$

This expression is called Lawson criterion, which is a criterion to sustain fusion reaction without any external heating [6].

As an extension of this criterion, “fusion triple product” $nT\tau_{\mathrm{E}}$ is often used because it is proportional to fusion energy gain factor. Fusion energy gain factor is defined as $Q = P_{\mathrm{fusion}}/P_{\mathrm{in}}$, where P_{fusion} and P_{in} are fusion power and input power, respectively. P_{fusion} is the sum of the powers which alpha particles and neutrons have and is five times of P_α. Therefore, the definition of Q is deformed as follows:

$$P_{\mathrm{in}} = \frac{P_{\mathrm{fusion}}}{Q} = \frac{5P_\alpha}{Q}. \tag{1.6}$$

Assuming a steady-state fusion plasma, the power balance is described as following equation.

$$P_{\mathrm{in}} + P_\alpha = \frac{W_{\mathrm{p}}}{\tau_{\mathrm{E}}}. \tag{1.7}$$

Considering (1.2), (1.4), and (1.6), the power balance equation is deformed as follows:

$$\begin{aligned} \frac{1}{Q} &= \frac{1}{5} \frac{W_{\mathrm{p}}/\tau_{\mathrm{E}}}{P_\alpha} - \frac{1}{5} \\ &\propto \frac{W_{\mathrm{p}}/\tau_{\mathrm{E}}}{P_\alpha} \propto \frac{nT/\tau_{\mathrm{E}}}{n^2 \langle \sigma v \rangle}. \end{aligned} \tag{1.8}$$

Here, $\langle \sigma v \rangle$ can be approximated as proportional to T^2 around 10 eV [7]. Therefore, the proportional relationship between the fusion triple product and fusion gain factor is obtained from (1.8).

$$Q \propto \frac{n^2 T^2}{nT/\tau_\mathrm{E}} = nT\tau_\mathrm{E}. \tag{1.9}$$

1.1.2 Magnetic confinement fusion

Since plasma is gas consisting of charged particles, that are ions and electrons, the plasma can be confined by magnetic field. One major concept of magnetic confinement is to confine plasma with torus-shape twisted magnetic field. There are several types of magnetic confinement fusion devices. The most progressed ones are tokamak and stellarator-heliotron. Both tokamak and stellarator-heliotron devices confine plasma in a torus-shape magnetic field.

Plasma is confined by twisted magnetic field which is superposition of toroidal magnetic field B_t and poloidal magnetic field B_p. In tokamak devices, the toroidal magnetic field B_t along with the core curve of the torus (toroidal direction) and formed by toroidal coils surrounding the axis of the torus. The poloidal magnetic field B_p is induced by the plasma current which flows along the toroidal direction. Generally, it is assumed that the magnetic field forms nested surfaces, which are called "flux surfaces." The axis of the cross sections of the nested surface is called "magnetic axis." The distance from the axis of the torus to the magnetic axis is called the major radius R, while the radius of the tube is called minor radius a. The ratio of R and a is called aspect ratio $A \equiv R/a$. On each flux surface, the number of poloidal transits per single toroidal transit of a magnetic field line is called the rotational transform $\iota/2\pi$, and defined as follows:

$$\frac{\iota}{2\pi} = \frac{R}{r}\frac{B_\mathrm{p}}{B_\mathrm{t}} \tag{1.10}$$

Here, r is the minor radius of the flux surface. In tokamak studies, the safety factor $q \equiv 2\pi/\iota$ is useful. The flux surface where the safety factor is a rational number $q = m/n$ is called "rational surface," and it is known that the magnetohydrodynamic (MHD) instability with toroidal and poloidal mode numbers of (m, n) can grows through resonance.

Tokamaks have an advantage in heating plasma by this large plasma current of the order of MA, while tokamak plasma can be unstable by the existence of the large plasma current. The tokamak experimental device, JT-60SA was built in Naka city, Japan in 2020. Also, the largest tokamak device, ITER, is now being built in Saint Paul-lez-Durance, France under the international collaboration to prove the scientific and technological feasibility of fusion energy.

On the other hand, magnetic field in stellarator-heliotron devices is formed only by external coil. Large Helical Device (LHD) is the largest stellarator-heliotron experimental device with superconducting coils and is located in Toki city, Japan [8]. Stellarator-heliotron devices have the advantage of stable confinement magnetic field compared to tokamak devices, but another difficulty exists in constructing complex-shaped helical coils.

Research on magnetic confinement fusion plasmas continues with the aim of achieving high-performance plasmas, such as high density n or high pressure nT, to obtain high fusion triple product. However, there are operational limits and abrupt plasma terminations occur in high-performance plasma.

1.2 Abrupt plasma termination events and operational limits

1.2.1 Disruption

There are several abrupt termination events in fusion plasma, which prevent confining plasma stably. The most distinguished termination event in tokamaks is disruption, which is the sudden collapse of plasma current [9]. The disruption event consists of two phases, i.e., thermal quench and current quench. In the first phase, thermal quench, the energy stored in the core plasma is released quickly, typically within 1 ms, and the plasma temperature decreases. Here, plasma electric resistivity is inversely proportional to the 3/2 power to plasma temperature. Therefore the decrease of plasma temperature makes plasma resistivity increase, which accelerates the decay of plasma current, and eventually, the plasma current shutdown in time scale of a few tens of milliseconds. This is the current quench, the second phase of disruption.

Disruption causes severe damage to the tokamak device. The thermal quench caused by a disruption dumps an excessive heat load on the first wall and the in-vessel components. The rapid decrease in plasma current also generates a large magnetic force on the vacuum vessel. Also, runaway electrons, which are generated in current quench phase, can cause melting when they hit on the in-vessel components [10, 11].

Disruption is classified into several types according to its causes. The typical causes are follows:

- Vertical displacement events (VDE) [12]
  Tokamak plasma with vertically elongated cross section can be unstable against the vertical displacement, which is called VDE. When VDE occurs, plasma shrinks as it moves vertically, the safety factor q decreases, and finally, plasma disrupts.

- Disruption caused by radiative loss [13]
  In high-density plasma or plasma with contamination of impurities, radiative loss from plasma increases, and the balance between radiative loss and heating power is lost. This unbalance causes the shrinkage of plasma and leads to magneto-hydrodynamic (MHD) instability. The best-known density limit in tokamak plasma is the Greenwald limit n_{G}, defined with plasma current I_{p} as follows [14]:

  $$n_{\mathrm{G}}[10^{20}\,\mathrm{m}^{-3}] = \frac{I_{\mathrm{p}}[\mathrm{MA}]}{\pi a[\mathrm{m}]^2}, \tag{1.11}$$

- Low-q disruption
  When surface q decreases, the rational surface where instability can easily grows approaches to the surface and the plasma becomes easy to disrupt by the kink instability.

- Disruptions driven by plasma pressure
  When plasma pressure becomes high, MHD instabilities, such as a ballooning instability and a resistivity wall mode (RWM), occurs to lead plasma to disruption.

Here, the ratio of the plasma pressure to the magnetic pressure is often used as indicator of plasma performance, symbolized by β:

$$\beta = \frac{\langle p \rangle}{B^2/2\mu_0}, \tag{1.12}$$

where $\langle p \rangle$ is the mean plasma pressure, B the mean total magnetic field strength, and μ_0 is the vacuum permeability. The β against toroidal field $\beta_t = \langle p \rangle / \left(B_{\mathrm{t}}^2/2\mu_0\right)$ and against poloidal field $\beta_p = \langle p \rangle / \left(B_{\mathrm{p}}^2/2\mu_0\right)$ are called toroidal beta and poloidal beta, respectively. Usually, the normalized beta β_{N} is used to discuss the limit of plasma performance in tokamaks.

$$\beta_{\mathrm{N}} = \frac{\beta_{\mathrm{t}}[\%]}{I_{\mathrm{p}}[\mathrm{A}]/a[\mathrm{m}]B_{\mathrm{t}}[\mathrm{T}]}. \tag{1.13}$$

The denominator of the right-hand side of (1.13) is called Troyon limit [15].

1.2.2 Radiative collapse and density limit in stellarator-heliotron plasma

No disruptions occur in stellarator-heliotron plasmas since the large plasma current is not required to sustain plasmas. Instead, radiative collapse is the main cause of the termination and limits the operational density in stellarator-heliotron plasmas. The Sudo density is the best-known empirical density limit in stellarator-heliotron plasma, which has been formulated from the observations in medium-sized stellarator-heliotron devices, i.e., Heliotron E, Wendelstein VII-A, L2, and Heliotron DR [16].

$$n_{\mathrm{e}}^{\mathrm{Sudo}}[10^{20}\,\mathrm{m}^{-3}] = 0.25\sqrt{\frac{PB}{a^2R}}. \tag{1.14}$$

Here, P is the absorbed heating power (MW), B is the magnetic field strength on the magnetic axis (T), a is the average minor radius (m), and R is the major radius (m). The Sudo scaling suggests that the balance between heating power and radiated power loss is a key together with robust confinement capability such as plasma volume and magnetic field. It is thought that the radiative collapse in LHD occurs because of drop of temperature in plasma edge region, and light impurities such as oxygen and carbon play an essential role in this phenomena [17]. Therefore, the limit of electron density in the plasma edge region, considering that the density where the electron temperature is around 100 eV is important, has been proposed [18].

The density limit in stellarator-heliotron plasmas are also studied theoretically [19, 20]. One theory formulates the relation between the critical density of detachment and the minor radius where impurity radiation loss fully reaches the heating power [21]. Radiation loss power by impurities is calculated by the following equation.

$$P_{\mathrm{rad}} = \int n_{\mathrm{e}} n_{\mathrm{imp}} L_Z(T_{\mathrm{e}}) dV \tag{1.15}$$

Here, n_{e}, n_{imp}, and V are electron density, density of target impurity ion, and plasma volume, respectively. L_Z is a coefficient specific to impurity species and is a function of electron temperature T_{e}, referred to the cooling rate [5]. According to this theory, the critical density has been evaluated in W7-AS, which is a stellarator device operated in Germany from 1988 to 2002 [22], as follows [23],

$$n_{\mathrm{c}} \propto \left(\frac{P}{V}\right)^{0.40} B^{0.32} \iota_{2/3}^{0.16}, \tag{1.16}$$

where $\iota_{2/3}$ is the rotational transform at $r = 2a/3$. It seems to be supported that the balance between heating power and radiant power loss is an important mechanism for the occurrence of collapse by the fact that this equation is close to Sudo scaling (1.14).

In an early research on the density limit in LHD, electron density limit has been indicated to be greater than Sudo limit by 40% [24]. This result suggests that the contributions of operational parameters other than taken into account in the Sudo scaling and the theoretical studies, such as wall condition and impurity concentration, may be hidden behind these expressions.

1.3 Data-driven research on plasma termination events

Prediction and avoidance of these termination events are important as well as mitigation of the damaging effect of these to realize fusion reactor. However, the physical mechanism of these termination events have not been clearly identified. Various phenomena in plasma, such as transports, MHD, and atomic processes, are complicatedly involved to the occurrence of these termination events. Therefore, it is too difficult to describe these termination events by differential equations completely. It will also be a problem that the plasma experiment data are too large to treat in clasical statistical method because of improvement of diagnositcs and plasma control. In ITER, the amount of experiment data is expected to be more than 1TB per discharge [25]. Therefore, the data-driven approach using machine learning techniques and a huge amount of experiment data is attracting attention, especially in the study of disruption.

Feedforward neural network (FNN) models were used to predict disruptions in some tokamaks, as early studies of this topic [26–30]. In DIII-D, which is operating in San Diego, the US, an FNN model was trained to predict β_N value at the moment of the occurrence of disruption [26]. The stability against disruption was predicted by multiple FNNs in JT-60U, which stopped the operation in 2008 in Naka, Japan [30]. For mitigation of the damage caused by disruption, an FNN predictor model was tested in ASDEX-Upgrade, which is a medium-sized tokamak in Garching, Germany [27].

In Joint European Torus (JET), which is a tokamak device in Culham, the UK, a real-time disruption predictor named Advanced Predictor of Disruptions (APODIS) was developed and deployed in the JET real-time network [31, 32]. APODIS consists of multiple support vector machines (SVMs). In the JET, some advanced studies using APODIS were conducted, e.g., the parameters to train the SVM model were selected by a genetic algorithm [33], and the prediction performance was compared changing the condition of the inner wall of JET [34]. In recent years, disruption predictor models based on an SVM model and a classification tree model were developed in JET with a concept called adaptive learning, in which the machine learning model is retrained after every false prediction [35, 36].

In DIII-D, disruption predictor model was developed based on random forest (RF) algorithm [37], which is one of ensemble learning algorithms [38]. The model was named Disruption Prediction using Random Forests (DPRF) and applied to the real-time prediction of disruptions [39]. One advantage of using the random forest to predict disruption is that the result is interpretable by analyzing the contributions of each parameter to the prediction. It is important to be interpretable the prediction result for developing a physically reliable, not black-boxed, predictor in a future fusion reactor.

Here, the importance of cross-machine analysis of the predictor is well known because the future predictor model is required to predict disruptions in unknown devices like ITER, DEMO, or future fusion reactor. The adaptive predictors developed in JET were applied to experiments in ASDEX-Upgrade [40]. The performance of random forest predictor was evaluated using experiment data in tokamaks such as Alcator C-Mod, EAST, and JET as well as DIII-D [41–43]. In EAST, which is a tokamak device in Hefei, China, the DPRF was used to predict disruption in real-time [44].

As another approach, "disruptivity" was proposed to define the likelihood of a disruption in JET [45] and NSTX [46]. The disruptivity here is defined as the number of disruptions that occur in a specific parameter space divided by the duration time that the plasma is in that state. The relationships between disruptivity and operational boundaries has been discussed statistically. Recently, the onset of tearing instability, which is one of the major causes of disruption, has been characterized using hazard function based on the survival analysis method [47] in DIII-D [48].

It is recognized that appropriate selection of the input data would be quite important to improve the prediction performance. Once the parameters that optimize the prediction is selected, these parameters are expected to be relevant to the physical mechanism of termination events. In other words, parameter selection can give some insight into physical discussions and prevent the predictor from being totally black-boxed.

1.4 Outline of this research

The main purpose of the data-driven approach is to predict abrupt termination events with the data-driven approach by machine-learning techniques and experiment data accumulated in fusion experimental devices. On the other hand, the physical background of the termination events have been studied continuously. The present study is approaching both improving the prediction performance and facilitating the physical discussion of the prediction results through parameter selection using sparse modeling.

In this thesis, prediction and feature extraction of both radiative collapse in LHD and high-beta disruption in JT-60U are discussed to show that the data-driven approach can be applied to a variety of abrupt terminations phenomena. The prediction of these abrupt terminations has been treated as to classify plasma state into two states: stable and approaching the termination. The exhaustive search, which is one of sparse modeling techniques, has been employed to extract feature parameters of the termination events. To pave the way for applying the prediction to plasma control, the classification model is extended to continuous probability, called "likelihood" of the occurrence of the termination event.

The machine-learning techniques used in the present research are explained in chapter 2. A support vector machine has been used as a binary classifier. In this chapter, sparse modeling, which is a framework of data-driven science, is also described. It exploits the inherent sparseness in all high-dimensional data to extract the information from the data [49].

In chapter 3, prediction and feature extraction of plasma termination events in stellarator-heliotron plasma are described. The experiment data of with radiative collapse in LHD has been used here. The plasma experiment in LHD to avoid radiative collapse using the prediction model is also explained in this section. To understand the physical background of radiative collapse, simulation results by the EMC3-EIRENE code are also discussed.

Prediction and feature extraction of disruption in tokamak plasmas are described in chapter 4. Disruptions in high-beta plasma in JT-60U has been mainly investigated in this chapter. The result of the prediction of high-beta disruption in JT-60U is compared with the result in DIII-D in this section.

Finally, chapter 5 concludes this thesis.

Chapter 2

Machine learning techniques

2.1 Classification by machine learning

2.1.1 Selection of machine-learning algorithm

In previous researches mentioned in section 1.3, various machine-learning algorithms were employed to develop predictor models of disruptions, e.g., artificial neural network, support vector machine (SVM), and random forest. In the present research, a linear SVM has been employed as a binary classifier to classify plasma state into stable or not. It is mainly because classification criteria can be expressed as a simple equation by a linear SVM. The simple expression makes it easy to discuss the physical background of the phenomena based on the expressions, as well as to apply the prediction to a real-time plasma control by reducing calculation cost.

2.1.2 Linear support vector machine

SVM is one of the supervised machine learning techniques [50]. The term "supervised" means that the machine learning model works with the dataset labeled in advance. The most basic use of the SVM is a binary classifier that divides data into two classes. Consider a dataset containing N sets of a d-dimensional vector data $\boldsymbol{x}_i \in \mathbb{R}^d$ and a label $y_i \in \{-1, 1\}$ describing the class to which the data belong. The classifier $g(\boldsymbol{x})$ is defined by the following decision function, where $f : \mathbb{R}^d \to \mathbb{R}$:

$$g(\boldsymbol{x}) = \begin{cases} 1, & \text{if } f(\boldsymbol{x}) > 0, \\ -1, & \text{if } f(\boldsymbol{x}) < 0. \end{cases} \tag{2.1}$$

The decision boundary of the classifier $g(\boldsymbol{x})$, defined as $f(\boldsymbol{x}) = 0$, is a d-dimensional hyperplane.

In the present research, a linear SVM, whose decision function is a linear function as following equation, has been used as a binary classifier.

$$f(\boldsymbol{x}) = \boldsymbol{w} \cdot \boldsymbol{x} + b, \tag{2.2}$$

where the coefficients $\boldsymbol{w} \in \mathbb{R}^d$ and $b \in \mathbb{R}$ are called "weight" and "bias", respectively. The process to optimize the weight and the bias is called "training" the SVM model.

Suppose that there is a pair of $\boldsymbol{w}$ and b that can correctly classify all data, in other words, the dataset is "separable". Under this assumption, the signs of the value of decision function $f(\boldsymbol{x}_i)$ and the label y_i must be equal for each pair of the data $\boldsymbol{x}_i$ and the label y_i. Therefore, there exists $f(\boldsymbol{x})$ such that $y_i f(\boldsymbol{x}_i) > 0$ for all $i = 1, \cdots, N$. Here, in general, multiple decision boundaries that can separate the dataset correctly can exist. When training the SVM, the parameters of the boundary hyperplane are selected to maximize the distance between the boundary and the data points closest to the boundary. The closest data points are called the "support vectors", and the distances between the hyperplane and the support vector is called the "margin". This concept to select the boundary is called "margin maximization." Figure 2.1 shows a schematic diagram of an SVM with a separable dataset.

A distance between the decision boundary $f(\boldsymbol{x}) = 0$ and a data $\boldsymbol{x}_i$ is denoted as follows:

$$\frac{|\boldsymbol{w} \cdot \boldsymbol{x}_i + b|}{||\boldsymbol{w}||}. \tag{2.3}$$

To classify all data correctly, $y_i f(\boldsymbol{x}_i) \geq M$ holds with an $M > 0$. Since M is no more than all $y_i(\boldsymbol{w} \cdot \boldsymbol{x}_i + b)$, the maximum M is equal to the minimum $y_i(\boldsymbol{w} \cdot \boldsymbol{x}_i + b)$ among all i. When $y_i(\boldsymbol{w} \cdot \boldsymbol{x}_i + b)$ takes the minimum value with $i = i'$, the distance between the boundary and the data closest to the boundary is described as follows:

$$\frac{|\boldsymbol{w} \cdot \boldsymbol{x}_{i'} + b|}{||\boldsymbol{w}||} = \frac{y_{i'}(\boldsymbol{w} \cdot \boldsymbol{x}_{i'} + b)}{||\boldsymbol{w}||} = \frac{M}{||\boldsymbol{w}||}. \tag{2.4}$$

Therefore, the margin optimization is formulated as

$$\begin{aligned} &\max_{\boldsymbol{w},b,M} \frac{M}{||\boldsymbol{w}||}, \\ &\quad \text{s.t. } y_i(\boldsymbol{w} \cdot \boldsymbol{x}_i + b) \geq M \ (i = 1, \cdots, N). \end{aligned} \tag{2.5}$$

When $\boldsymbol{w}$ and b are replaced by $\boldsymbol{w}/M$ and b/M, respectively, the objective function is expressed as $1/||\boldsymbol{w}||$ with redefining $\boldsymbol{w}/M$ and b/M as $\boldsymbol{w}$ and b. Since maximizing $1/||\boldsymbol{w}||$ is equivalent to minimizing $||\boldsymbol{w}||^2$, the optimization problem (2.5) is denoted as the following equation.

$$\begin{aligned} &\min_{\boldsymbol{w},b} ||\boldsymbol{w}||^2, \\ &\text{s.t. } y_i(\boldsymbol{w} \cdot \boldsymbol{x}_i + b) \geq 1 \ (i = 1, \cdots, N). \end{aligned} \tag{2.6}$$

The above explanation (2.6), which is called “hard margin,” assumes that all data can be completely divided by the boundary hyperplane. However, this is rarely the case in practice. For a more realistic data separation, we extend this concept to “soft-margin” optimization, where some data can inhabit the opposite side of the boundary hyperplane. To specify the maximum amount of data that can reside on the opposite side, a parameter called the regularization parameter $\xi_i \geq 0 (i = 1, \cdots, N)$ is introduced and the constraint of (2.6) is changed as follows:

$$y_i(\boldsymbol{w} \cdot \boldsymbol{x}_i + b) \geq 1 - \xi_i \ (i = 1, \cdots, N). \tag{2.7}$$

When $\sum_{i=1}^{N} \xi_i$ is no more than an integral number K, the maximum number of the data across the boundary is K or less. It means that the number of miss classifications can be reduced by keeping $\sum_{i=1}^{N} \xi_i$ as small as possible. Therefore, the optimization problem of the SVM with soft margin is denoted as follows:

$$\begin{aligned} &\min_{\boldsymbol{w},b} \frac{1}{2}||\boldsymbol{w}||^2 + C\sum_{i=1}^{N} \xi_i, \\ &\text{s.t. } y_i(\boldsymbol{w} \cdot \boldsymbol{x}_i + b) \geq 1 - \xi_i \ (i = 1, \cdots, N), \\ &\quad \xi_i \geq 0 \ (i = 1, \cdots, N). \end{aligned} \tag{2.8}$$

The parameter $C > 0$ is called “regularization parameter.” The larger C means the strict suppression of miss classifications. When $C \to \infty$, the optimization problem is equivalent to the optimization problem of a hard margin SVM.

2.1.3 Preprocessing

Physical phenomena frequently expressed in exponential form like power law. However, the decision boundary that the linear SVM returns is a hyperplane, as mentioned above. Also, in general, the normalization of the dataset is important to improve the performance of the machine learning model and to accelerate the training process. Therefore, in the present study, the dataset has been taken logarithms and min-max normalized as following equation before training the linear SVM.

$$\hat{x_i} = \frac{\ln x_i - \ln x_i^{min}}{\ln x_i^{max} - \ln x_i^{min}}. \tag{2.9}$$

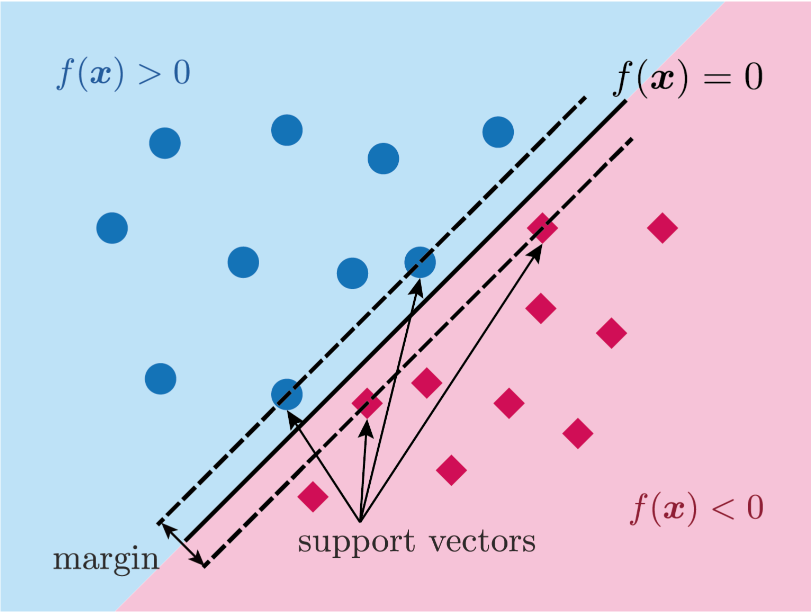

Figure 2.1: The schematic diagram of SVM.

Here, x_i is the i-th parameter of a data $\boldsymbol{x}$ and $\hat{x}_i$ is the i-th parameter of a corresponding normalized data $\hat{\boldsymbol{x}}$. The superscript "max" and "min" mean the maximum and minimum values of x_i in the dataset, respectively.

By this preprocessing, the boundary equation is deformed into $f_{\mathrm{exp}}(\boldsymbol{x}) = 1$, using the exponential decision function $f_{\mathrm{exp}}(\boldsymbol{x})$, weight $\boldsymbol{w}' = (w'_1, \cdots, w'_d)$, and bias b' shown in the following equations.

$$f(\boldsymbol{x}) = \sum_{i=1}^{d} (w\hat{x}_i) + b = \ln\left(e^{b'} \cdot \prod_{i=1}^{d} x_i^{w'_i}\right), \tag{2.10}$$

$$f_{\mathrm{exp}}(\boldsymbol{x}) = \exp\left(f(\boldsymbol{x})\right) = e^{b'} \cdot \prod_{i=1}^{d} x_i^{w'_i}, \tag{2.11}$$

$$w'_i = \frac{w_i}{\ln x_i^{max} - \ln x_i^{min}}, \tag{2.12}$$

$$b' = b - \sum_{i=1}^{d} \frac{w_i \cdot \ln x_i^{min}}{\ln x_i^{max} - \ln x_i^{min}}. \tag{2.13}$$

Table 2.1: Confusion matrix.

		True label	
		Positive (+1)	Negative (-1)
Predicted label	Positive (+1)	True Positive (TP)	False Positive (FP)
	Negative (-1)	False Negative (FN)	True Negative (TN)

2.1.4 Metrics of classification

The classification results are divided into four categories, that is, True Positives (TP), False Positives (FP), True Negatives (TN), and False Negatives (FN). Here, “True” and “False” correspond to that the classification results are true of false, “Positives” and “Negatives” correspond to the label $\{0, 1\}$ that the classifier model returns. These four categories of the result are often shown in a table named “confusion matrix” to show the performance at a glance, which is shown in Table 2.1.

There are several metrics to express the performance of classification. The best simple one is the accuracy (ACC), that is the ratio of the number of correct classifications to the total number of data,

$$\mathrm{ACC} = \frac{TP + NP}{TP + FP + TN + FN}. \tag{2.14}$$

The ACC is not so useful when the numbers of data with each label are uneven. To evaluate the sensitivity of the classifier, the metric called “recall” is used, that is the ratio of the number of data correctly classified as positive to the total number of positive data,

$$\mathrm{Recall} = \frac{TP}{TP + FN}. \tag{2.15}$$

The reliability of the prediction to be positive is expressed by “precision,” that is the the ratio of the number of data correctly classified as positive to the total number of the data predicted as positive,

$$\mathrm{Precision} = \frac{TP}{TP + FP}. \tag{2.16}$$

To evaluate the performance of classification by the SVM in the present study, F1-score [51], which is one of the metrics commonly used to evaluate machine learning classifier, has been used. When the positive class is detected accurately and the negative class is not detected as positive falsely, F1-score approaches to one. F1-score is denoted as follows:

$$\text{F1-score} = \frac{2 \times \text{Recall} \times \text{Precision}}{\text{Recall} + \text{Precision}} = \frac{TP}{2TP + FN + FP}. \tag{2.17}$$

This definition is interpreted as the F1-score is the harmonic mean of the recall and precision.

2.2 Sparse modeling

2.2.1 Concept of sparse modeling

For all machine learning tasks, it is known that finding essential explanatory variables from a large number of candidate variables is important [52]. Sparse modeling is one of the effective frameworks of data-driven science. In the sparse modeling, the sparseness inherent in all high-dimensional data is exploited to extract the maximum amount of information from the data. Specifically, a combination of parameters that reduces the number of parameters is searched automatically to match the data well [49, 53].

2.2.2 Exhaustive search

When selecting input parameters in a classification problem, it is important to consider combination effects among parameters as well as individual distributions of each parameter. Figure 2.2 schematically shows a example of parameter selection in classification problem. Consider the problem of classifying two types of four-dimensional data according to their labels, blue and orange. The distributions of each parameter is shown along each axis in Fig. 2.2. Here, parameter Nos. 1 and 3 follow the same distribution. Parameter Nos. 2 and 4 also follow the same distribution, but a quite different distribution from that of Nos. 1 and 3, which is not well separated. When dividing these data into two groups, division using No. 1 and No. 2 is no better than assigning all data to No. 1, according to the black line in the left scatter plot in Fig. 2.2. This means that the parameter No. 2 is not relevant to the classification. On the other hand, separation using Nos. 3 and 4 is more effective than assigning all data to No. 3, even the distribution of No. 4 is as same as that of No. 2. In conclusion, when selecting the input parameters for the classification, both their individual distributions and combinations should be considered.

The exhaustive search (ES) is one of the sparse modeling techniques, in which all possible combinations of parameters are compared each other by generalization performance to obtain the optimal combination of parameters [54].

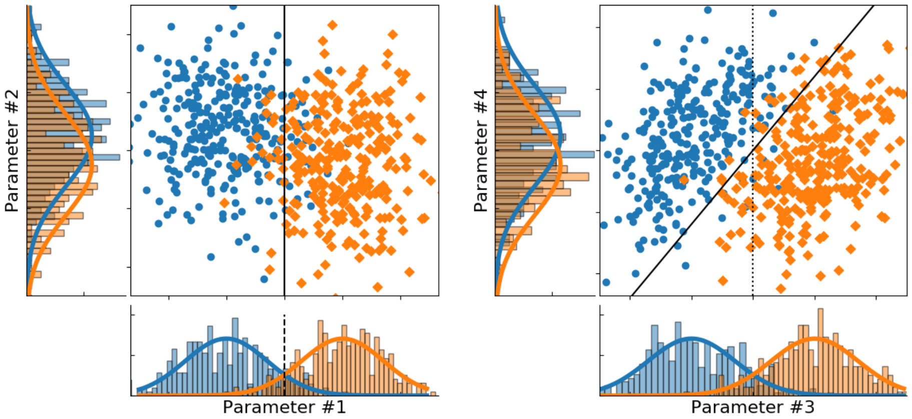

Figure 2.2: The schematic example of the parameter selection in classification problem.

To express each combination of parameters, indicator vector $\boldsymbol{c}$ is defined as p-dimensional binary vector shown in the following equation.

$$\boldsymbol{c} = (c_1, \cdots, c_N) \in \{0, 1\}^N , \tag{2.18}$$

where N is the number of parameters. Each element c_i tales 0 or 1. If the i-th parameter belongs to the combination, $c_i = 1$. Otherwise, $c_i = 0$. In the ES using SVM (ES-SVM), the SVM model is trained and tested for all combinations. The input vector $\boldsymbol{x}$ and the weight $\boldsymbol{w}$ is replaced by $\boldsymbol{x} \circ \boldsymbol{c}$ and $\boldsymbol{w} \circ \boldsymbol{c}$, respectively, for each combination. Here, the symbol $\circ$ represents the Hadamard product defined as $(\boldsymbol{x} \circ \boldsymbol{c}) = x_i c_i$.

To obtain the optimal combination of performance, the combinations must be compared in generalization performance, which is the performance on data outside the training data of the machine-learning models. Therefore, the classification performance is evaluated by M-fold cross validation (CV) for each combination, which is shown in Fig. 2.3. In M-fold CV, the finite available data is divided into M pieces. In the present study, M is fixed to 10. The machine-learning model is trained with $M - 1$ pieces of data. Subsequently, the trained model is evaluated with the remained data. This training and testing process is repeated M times changing the remaining piece of data. Finally, M performances obtained by M repetition are averaged to represent the generalization performance for the case using the combination.

Summarizing the above, the ES is the method to find out the optimal combination by the following procedure: all possible combinations are expressed

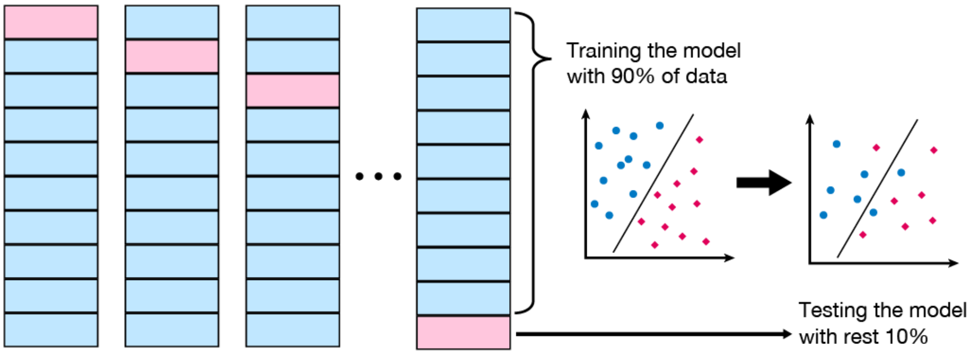

Figure 2.3: The schematic diagram of 10-fold cross validation.

by indicator vectors, the generalization performance is evaluated by CV for each combination, and finally, all generalization performances are compared each other.

2.2.3 K-sparse exhaustive search

For N parameters, the number of possible combinations is

$$2^N - 1 = {}_NC_1 + {}_NC_2 + \cdots + {}_NC_N. \tag{2.19}$$

Therefore, the number of calculations of the ES rises exponentially with the amount of data. To overcome this combination explosion risk, the K-sparse exhaustive search (ES-K) method has been applied [49]. This method assumes that the optimal combination of parameters is K-sparse, i.e., a combination of K out of N parameters is optimal.

Figure 2.4 shows the concept of the ES-K. In the ES-K, the ES method is applied to ${}_NC_K$ combinations for each K to obtain the optimal combination in ${}_NC_K$ combinations. The advantage of the ES-K is that the structure of the combination can be easily extracted by comparing the result of ES at different Ks as well as the reduction of the number of calculations by stopping at K smaller than N.

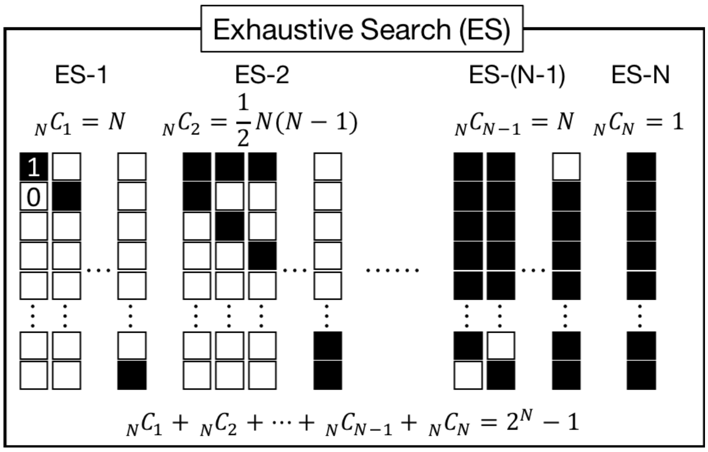

Figure 2.4: The schematic diagram of ES-K [4].

Chapter 3

Prediction and feature extraction of radiative collapse in stellarator-heliotron plasmas

3.1 Feature extraction of radiative collapse

3.1.1 Density ramp-up experiment in LHD

Large Helical Device (LHD) is the largest stellarator-heliotron experimental device with superconducting coils and is located in Toki city, Japan [8]. Radiative collapse mainly happens in high-density plasma in LHD. Therefore, data of density ramp-up experiments in hydrogen, deuterium, and helium plasmas has been accumulated to construct the dataset. In this study, the magnetic axis position R_{ax} was fixed at 3.6 m and magnetic field at magnetic axis in vacuum was either 1.375 T or 2.75 T. Fuels were supplied to plasma by gas-puff [55], and the electron cyclotron resonance heating (ECRH) and the neutral beam injection (NBI) were used to heat plasma. The ECRH was mainly used to initiate plasmas. The numbers of discharges with and without collapse considered in the dataset are shown in Table 3.1.

Table 3.1: Numbers of discharges considered in the dataset.

Species	With collapse	Without collapse
H	31	10
D	39	17
He	30	23

To classify data by SVM, it is necessary to label data into classes before the training. Here, each data has been labeled into either "stable" or "close-to-collapse" according to the plasma state. In the case of discharges without radiative collapse, built-up plasma discharge excluding initialization and termination phases have been used as "stable" data. Consequently, 706 "close-to-collapse" data and 3424 "stable" data have been considered in the dataset.

On the other hand, the data in discharges with collapse have been labeled according to the normalized time derivatives of radiation power $x_{\mathrm{rad}} = \dot{P}_{\mathrm{rad}}/P_{\mathrm{rad}}$. Here, the dots indicate the time derivative. This index is similar to the density exponent $x_{\mathrm{density}} = (\dot{P}_{\mathrm{rad}}/P_{\mathrm{rad}})/(\dot{\bar{n}}_{\mathrm{e}}/\bar{n}_{\mathrm{e}})$ since the temporal change of density is slower than that of radiation power. The density exponent is a criterion that shows a relationship between radiation power and plasma density, and it is known that a thermal instability occurs in the plasma as x_{density} becomes three or above [17]. In the present research, the phase with $x_{\mathrm{rad}} > 2.5$ has been labeled as "close-to-collapse" and included in the dataset. And the plasma is regarded as "stable" against radiative collapse before x_{rad} reaches 2. The "stable" data in the same time duration as "close-to-collapse" phase before x_{rad} reaches 2 have been taken into account to construct the dataset. The typical waveform of a discharge with radiative collapse is shown in Fig. 3.1. In Fig. 3.1, "close-to-collapse" and "stable" regions are hatched in red and blue, respectively.

To construct a dataset for ES, experiment data in hydrogen and deuterium plasmas have been considered first. The 15 plasma parameters listed in Table 3.2 have been considered in the dataset. Here, line averaged electron density $\bar{n}_{\mathrm{e}}$ is usually obtained by the far-infrared (FIR) laser interferometer [56]. The range of $\bar{n}_{\mathrm{e}}$ is 0.2×10^{19} to $1.4 \times 10^{20}\,\mathrm{m}^{-3}$.

A brief explanation of other parameters are following: Absorbed heating power P_{abs} is evaluated as the sum of the absorbed ECRH input power P_{ECH}, absorbed tangential NBI power $P_{\mathrm{NBI,tangential}}$, and absorbed perpendicular NBI power $P_{\mathrm{NBI,perpendicular}}$. Absorbed heating power of NBI is estimated by simple analytics based on results from FIT3D [57], and absorbed ECRH power is estimated by "LHDGauss", which is the ray-tracing code to calculate power deposition of ECRH and microwave beam propagation in LHD [58]. The range of P_{abs} is 0.76 to 15 MW. The radiation loss P_{rad} is measured by bolometer diagnostics [59]. The diamagnetic beta value is calculated based on the diamagnetic flux measurement [60]. Impurity line intensities of multiple wavelengths, that correspond to radiation caused by carbon, oxygen, and iron ions, have been included in the dataset. These line intensities are measured by the vacuum ultraviolet (VUV) spectroscopy [61]. Also, the ratio of deuterium ion to the sum of hydrogen and deuterium ions $\mathrm{D}/(\mathrm{H}+\mathrm{D})$ is evaluated by line intensities of H_α and D_α. The ion saturation current $I_{\mathrm{sat}}^{(7\mathrm{L})}$ is measured by Langmuir probes

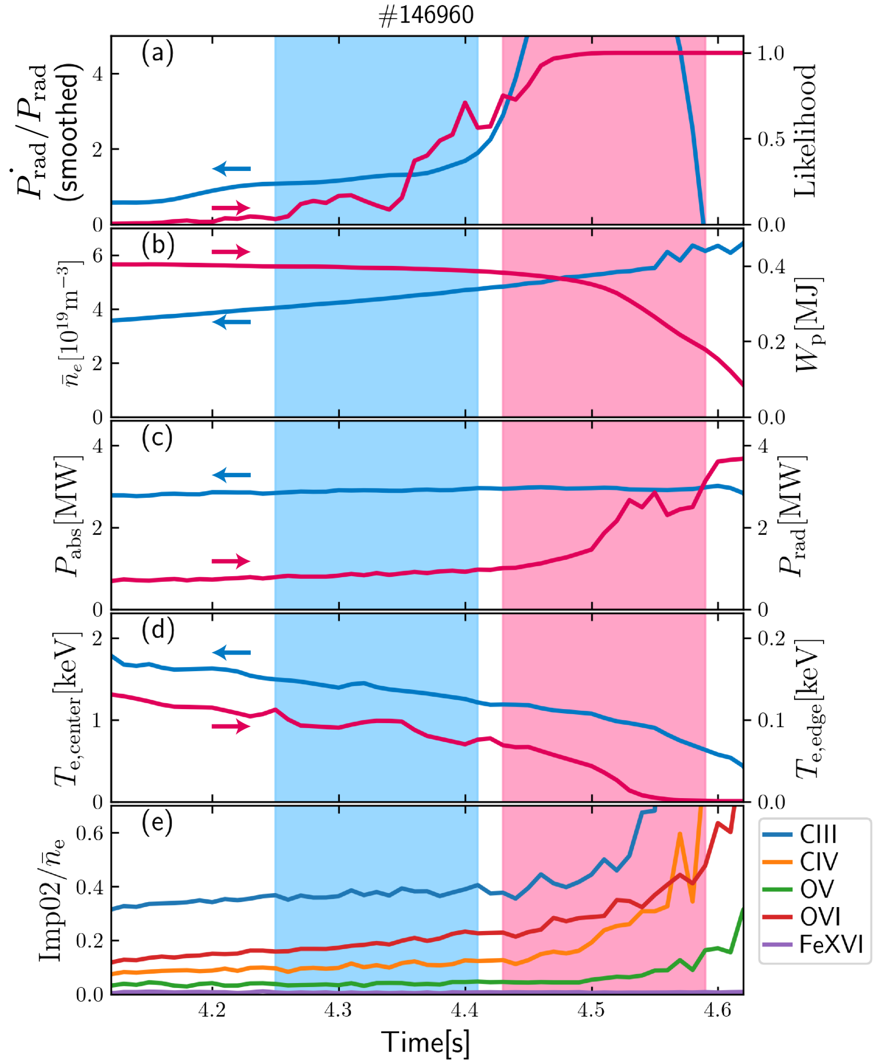

Figure 3.1: Typical discharge with a radiative collapse in the dataset. The red and blue regions are “close-to-collapse” region and “stable” regions, respectively [1]. (a) The normalized time derivative of radiation power is shown in blue and collapse likelihood (described in sec 3.1.3) is shown in red. (b) Line-averaged electron density $\bar{n}_{\rm e}$ is shown in blue, and diamagnetic stored energy $W_{\rm p}$, in red. (c) Absorbed heating power $P_{\rm abs}$ is shown in blue,4 and radiation loss $P_{\rm rad}$, in red. (d) Electron temperature at the plasma center $T_{\rm e,center}$ is shown in blue, and that at plasma edge $T_{\rm e,edge}$, in red. (e) Visible impurity line intensities normalized by $\bar{n}_{\rm e}$ are shown.

Table 3.2: Plasma parameters used in the dataset of radiative collapse [1].

Expression	Description
$\bar{n}_\mathrm{e}$	Line averaged electron density [$10^{19}\mathrm{m}^{-3}$]
B	Magnetic field at magnetic axis in vacuum [T]
$P_\mathrm{rad}/P_\mathrm{abs}$	Radiation loss normalized by absorbed input power
P_abs	Absorbed input power [MW]
β_dia	Diamagnetic beta value
Δ_sh	Shafranov shift [m]
a_{99}	Minor radius defined by the radius encompassing 99% of the stored energy [m]
CIII	CIII ($2\mathrm{s}^2\ {}^1\mathrm{S} - 2\mathrm{s}2\mathrm{p}\ {}^1\mathrm{P}$, 97.7 nm) line intensity normalized by $\bar{n}_\mathrm{e}$
CIV	CIV ($2\mathrm{s}\ {}^2\mathrm{S} - 2\mathrm{p}\ {}^2\mathrm{P}$, 154.9 nm) line intensity normalized by $\bar{n}_\mathrm{e}$
OV	OV ($2\mathrm{s}^2\ {}^1\mathrm{S} - 2\mathrm{s}2\mathrm{p}\ {}^1\mathrm{P}$, 63.0 nm) line intensity normalized by $\bar{n}_\mathrm{e}$
OVI	OVI ($2\mathrm{s}\ {}^2\mathrm{S} - 2\mathrm{p}\ {}^2\mathrm{P}$, 103.4 nm) line intensity normalized by $\bar{n}_\mathrm{e}$
FeXVI	FeXVI ($3\mathrm{s}\ {}^2\mathrm{S} - 3\mathrm{p}\ {}^2\mathrm{P}$, 33.5 nm) line intensity normalized by $\bar{n}_\mathrm{e}$
$I_\mathrm{sat}^\mathrm{(7L)}$	Ion saturation current on a divertor target plate [A]
$\mathrm{D}/(\mathrm{H}+\mathrm{D})$	Ratio of deuterium ion to the sum of hydrogen ion and deuterium ions
$T_\mathrm{e,edge}$	Electron temperature at the LCFS in vacuum [keV]

installed on the divertor plate [62]. The edge electron temperature $T_\mathrm{e,edge}$ is the mean value of T_e at inboard and outboard sides of last closed flux surface (LCFS) at vacuum, measured by the Thomson scattering measurement [63]. Here, the geometry of flux surfaces is calculated by VMEC code [64]. The data were resampled at 10 ms intervals to match the FIR measurements. For each parameter, the distributions of the data labeled either "close-to-collapse" and "stable" are shown in Fig. 3.2.

3.1.2 Result of feature extraction of radiative collapse

ES-K using SVM (ES-K-SVM) has been conducted with the dataset described in the above section. Figure 3.3 shows the summary of the result. The best F1-score among combinations of K parameters are shown in the left graph of Fig. 3.3 for each K. According to the graph, the F1-score almost saturated at around $K = 5$, and it reached almost the same as that with all 15 parameters at $K = 6$. The combination that gives the best F1-score among combinations of K parameters,

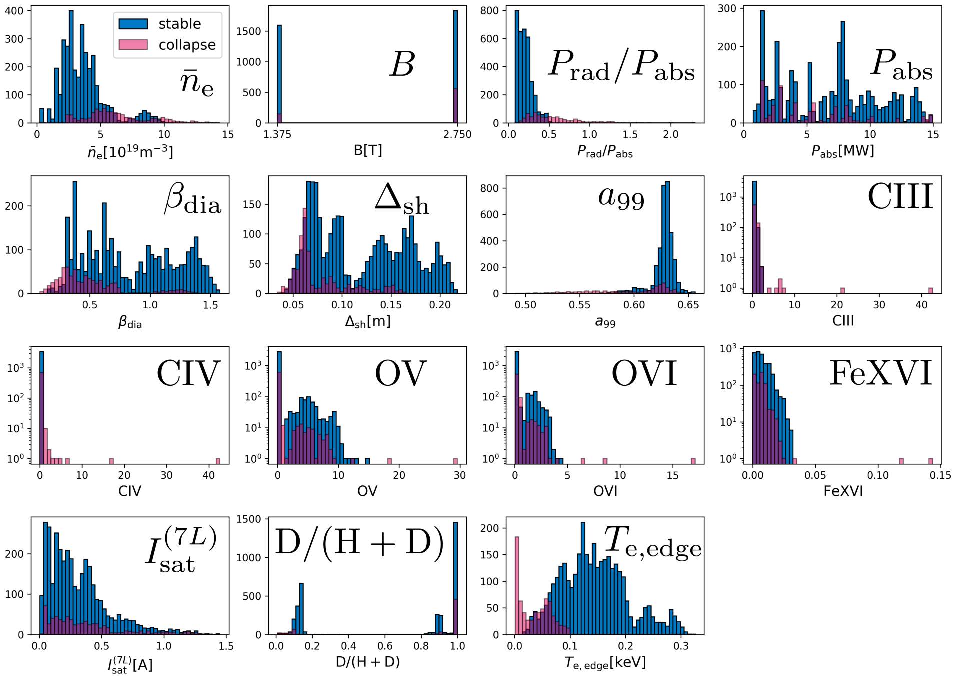

Figure 3.2: The distributions of the data labeled either "close-to-collapse" and "stable" for each parameters in the dataset. Note that vertical axes of impurity line emissions (CIII, CIV, OV, OVI, and FeXVI) are logarithmic [2].

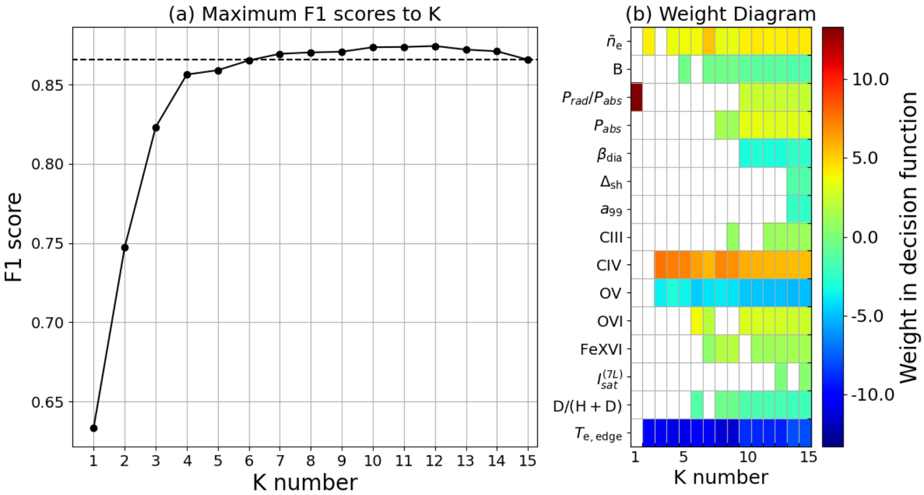

Figure 3.3: The summary of ES-K-SVM result [2]. The left graph shows the best F1-score among combinations of K parameters. The horizontal dashed line shows the F1-score with all 15 parameters ($K = 15$). The right diagram shows the combination that gives the best F1-score among combinations of K parameters, which correspond to the left graph. The color corresponds to the weight w' in eq. 2.12.

which correspond to the left graph, is shown in the right diagram of Fig. 3.3. Each column corresponds to each combination. The parameters included in each combination are colored according to the weight w' in the decision function (2.12). Around $K = 5$, four parameters are included in common in the top combination for each K, those are, $\bar{n}_\mathrm{e}$, CIV, OV, and $T_{\mathrm{e,edge}}$.

Figure 3.4 shows the result of ES-6, which is ES-K with $K = 6$. The left histogram shows the distributions of F1-score with six parameters by blue bars. The right diagram shows the top 20 combinations in the F1-score, from left to right. Each column corresponds to each combination. The parameters included in each combination is shown are colored according to the weight w' in the decision function (2.12). As shown in the right diagram, most of the top combinations includes some parameters in common with relatively high weight, that are, $\bar{n}_\mathrm{e}$, CIV, OV, and $T_{\mathrm{e,edge}}$. The combinations including these four parameters show better F1-score than other combinations, according to the red bars in the left diagram of Fig. 3.4. Therefore, these four parameters are relevant to the prediction of radiative collapse as the key parameters. The boundary between "close-to-collapse" and "stable" in the multi-dimensional space with these four

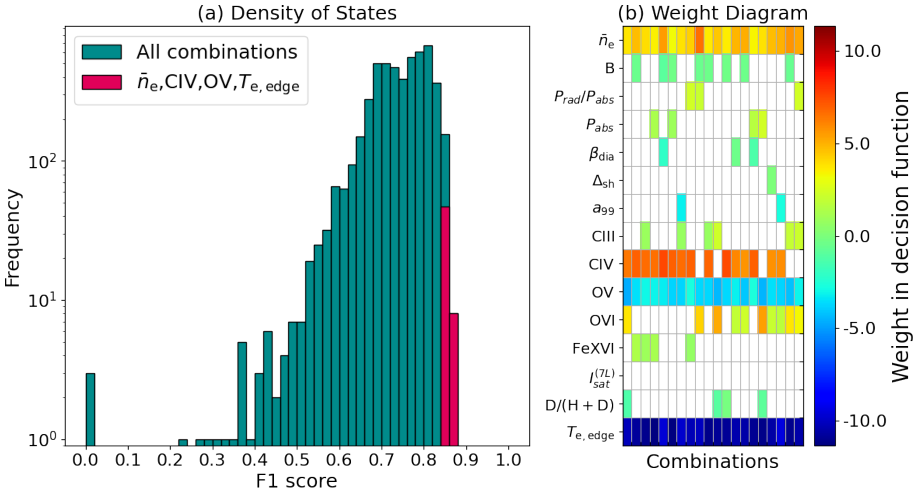

Figure 3.4: The result of ES when $K = 6$. The blue and red bars in the left diagram show the distributions of F1-score with six parameters and that with the combinations including $\bar{n}_e$, CIV, OV, and $T_{e,edge}$, respectively. The right diagram shows the parameters included in th top 20 combinations in the F1-score. The color bar corresponds to the weight w' in eq. 2.12.

key parameters is expressed as $f_{exp}(\boldsymbol{x}) = 1$ using the decision function $f_{exp}(\boldsymbol{x})$ defined as follows:

$$f_{exp}(\boldsymbol{x}) = \exp(-5.89)\bar{n}_e^{0.864}\mathrm{CIV}^{0.995}\mathrm{OV}^{-0.395}T_{e,edge}^{-1.85}. \tag{3.1}$$

Note that the coefficients in (3.1) correspond to the combination that showed the best F1-score in ES-4 and the constant normalization factor is multiplied and the weights of parameters are converted following (2.13).

3.1.3 Collapse likelihood

The likelihood of the radiative collapse has been quantitatively evaluated to take the continuous value from zero to one corresponding to the distance from the boundary. This makes it easy and flexible to apply the binary classifier model to predictor model.

The distribution of values of the decision function (3.1) for “close-to-collapse” and “stable” data in the dataset is shown in the lower panel of Fig. 3.5. Note that the histogram is normalized to make the sum of each label unity. Here, the decision function value corresponds to the distance from the boundary between

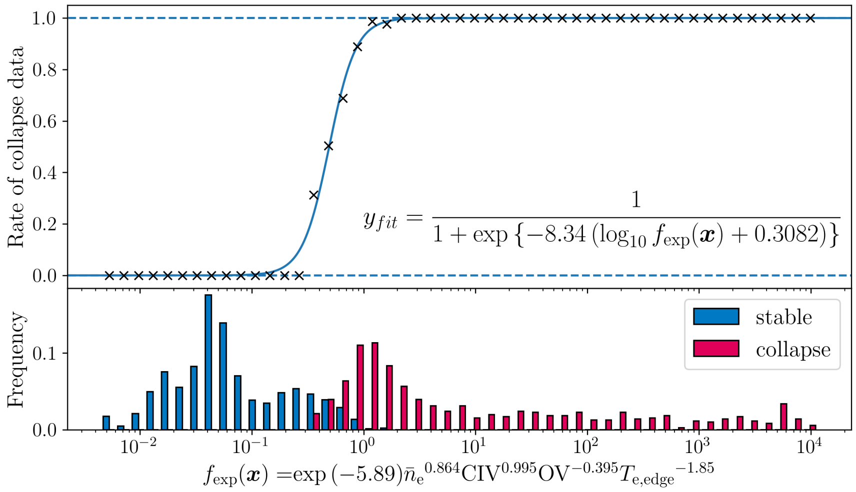

Figure 3.5: (lower) The distribution of the decision function values in the dataset. The red and blue bars show the “close-to-collapse” and “stable” data, respectively. (upper) The percentage of “close-to-collapse” data in each region of bins. The curve in the upper figure is a fitted curve of the percentage of “close-to-collapse” data. The expression function is also shown in the figure [2].

two labeled regions, and $f_{\rm exp}(\boldsymbol{x}) = 1$ means the data $\boldsymbol{x}$ is on the boundary. The “close-to-collapse” and “stable” data distribute mainly above and bellow one, respectively.

In the upper panel of Fig. 3.5, the ratio of “close-to-collapse” data against the sum of “stable” and “close-to-collapse” data in each region of bins is shown by crosses. Note that these histograms are normalized to make sums of all bins become unity for each label. This ratio is interpreted that the probability that the data is approaching to collapse when the value of decision function is given, and referred as “collapse likelihood”. Therefore, the collapse likelihood is corresponding to the distance from the boundary and has been fitted by the sigmoid function in the following equation, which is also shown by blue curve in the upper panel of Fig. 3.5.

$$\text{Likelihood} = \frac{1}{1+\exp\{-8.34\,(\log_{10} f_{\rm exp}(\boldsymbol{x}) + 0.3082)\}}. \tag{3.2}$$

Note that the likelihood is a function of the decision function $f(\boldsymbol{x})$, which is a function of vector of selected plasma parameters $\boldsymbol{x}$, and takes the continuous value from zero to one.

The critical density corresponding to the value of collapse likelihood is denoted as following equation by substituting the decision function (3.1) into the collapse likelihood (3.2).

$$\bar{n}_{\mathrm{e}}(\mathrm{Likelihood}) \propto \mathrm{CIV}^{-1.151}\mathrm{OV}^{0.458}T_{\mathrm{e,edge}}^{2.146}. \tag{3.3}$$

This expression of operational density limit is shown as a color contour in Fig. 3.6. The data in the training dataset is plotted above the color contour by dots and crosses, according to their labels, “stable” and “close-to-collapse”. Note that the critical density mentioned above is not the achievable density limit or the power balance limit, such as Sudo scaling, but a practical density limit to secure safe operation of the LHD plasma.

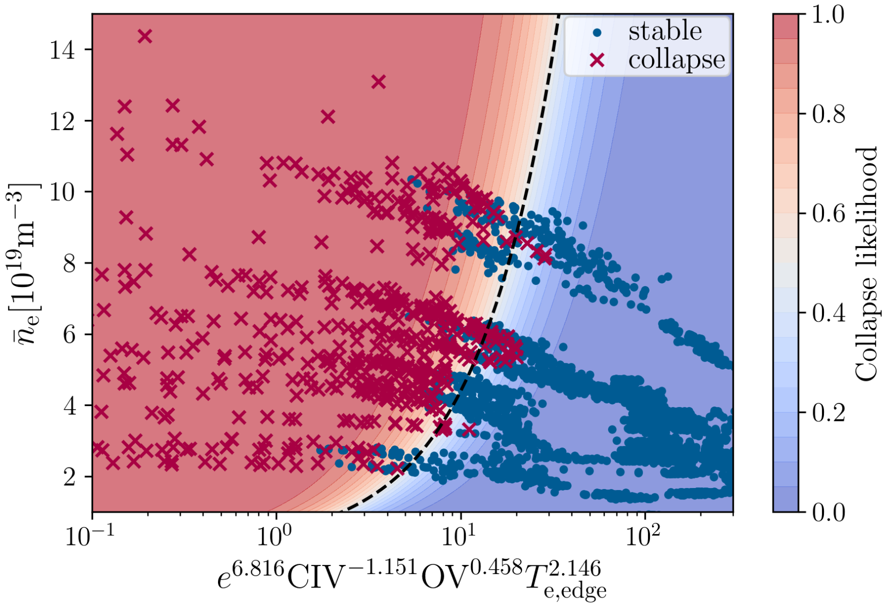

Figure 3.6: Color contour of the likelihood of radiative collapse against line averaged density and the term of other extracted parameters. The dashed line corresponds to likelihood of 0.5. The “stable” and “close-to-collapse” data in the dataset are plotted by dots and crosses, respectively.

3.1.4 Validation of collapse likelihood

The collapse likelihood has been validated with LHD experiment data other than included in the training dataset. The target discharges in the validation is selected as following rules.

- The shot number is between 159129 and 160770. This means shots after the investigated shots in the same experimental campaign (the 22nd cycle).

- The same arrangement of magnetic configuration such as the magnetic axis position R_ax of 3.6 m
- No impurity pellets are injected during the discharge.

The predictor does not include the information of discharges that are used in the validation since all discharges were performed after the discharge used for the dataset.

In validation, each discharge has been labeled as either collapsed discharge, stable discharge, or error discharge. As a criterion of plasma termination, the estimated plasma stored energy $W_\mathrm{dia}^\mathrm{ISS04}$ has been used, denoted as the following equation.

$$W_\mathrm{dia}^\mathrm{ISS04} = P_\mathrm{abs}\tau_\mathrm{E}^\mathrm{ISS04} \tag{3.4}$$

Here, $\tau_\mathrm{E}^\mathrm{ISS04}$ is the energy confinement time given by the ISS04 scaling law [65]. In order to calculate $\tau_\mathrm{E}^\mathrm{ISS04}$, $\bar{n}_\mathrm{e}$ measured by thomson scattering measurement has been used to avoid fringe jump in interferometer measurement.

The discharges in which W_dia fall below 30% of mean value of $W_\mathrm{dia}^\mathrm{ISS04}$ over the last 100 ms before the heating ends are labeled as collapsed discharges, while other discharges have been labeled as stable discharges. The time when W_dia falls below the threshold value has been defined to be the moment when the collapse occurs. Considering reliability of thomson scattering measurement in low-density regime, discharges in which mean $\bar{n}_\mathrm{e}$ in the 100 ms before the discharge ends is less than $0.5 \times 10^{19}\,\mathrm{m}^{-3}$ have been excluded from the validation as error discharges. Also, discharges with measurement failure have been excluded from the validation as error discharges. Consequently, 91 collapse discharges and 444 stable discharges have been taken into account.

Figure 3.7 shows the mean temporal changes of the collapse likelihood in (a) stable discharges and (b) collapse discharges used in the validation. According to Fig. 3.7 (b), the likelihood grows as the plasma approaches the collapse in average.

Table 3.3 shows the performance of prediction as the threshold likelihood is changed. When the likelihood exceeds the threshold value, it is treated as an alarm is raised. The results of prediction in collapse discharges are categorized into four cases as follows:

- Success alarm is the alarm that does not correspond to any of the following categories raised in collapse discharge.
- Missed alarm is the case in which the likelihood does not reach the threshold before the occurrence of the collapse.

- Tardy alarm is the alarm raised less than 30 ms before the collapse occurs is considered as a tardy alarm.

- Early alarm is the alarm raised more than 500 ms before the occurrence of the collapse.

Missed and tardy alarms are both equivalent to having missed the collapse.The alarms raised in the stable discharges are categorized as false alarms. Both early and false alarms are thought to be interruptions of stable plasma, which are undesirable. In this validation, more than 85% of collapse has been predicted before occurrence successfully with the threshold value of 0.8 or less. At the same time, false alarm has been 5–10% of the number of stable discharges.

In Table 3.4, the mean and standard deviation values of the time margin by the collapse occurred from the alarms are raised are shown as the threshold likelihood is changed. On average, there is a margin of 100 to 150 ms to manage to the collapse. This averaged margin time is in the same level of energy confinement time τ_{E} in these experiments. This predicting capability is supposed to be relevant to control of avoidance of radiative collapse.

Missed and tardy alarms are essentially the same failure of prediction since they overlook the collapse. When the threshold likelihood is set as 80%, there are nine overlooked collapses in the validation, and six among them were helium discharges. There are only eight helium discharges included in the validation and the others are hydrogen discharge with helium and deuterium contamination. In the rest helium discharges, the likelihood reached 80% just 30 ms before the collapse is detected that means this discharge is on the border between tardy and success alarm. This result shows the model trained with data in hydrogen and deuterium plasma has not been quite successful for helium discharges yet. The improvement of the prediction considering helium discharges is described later.

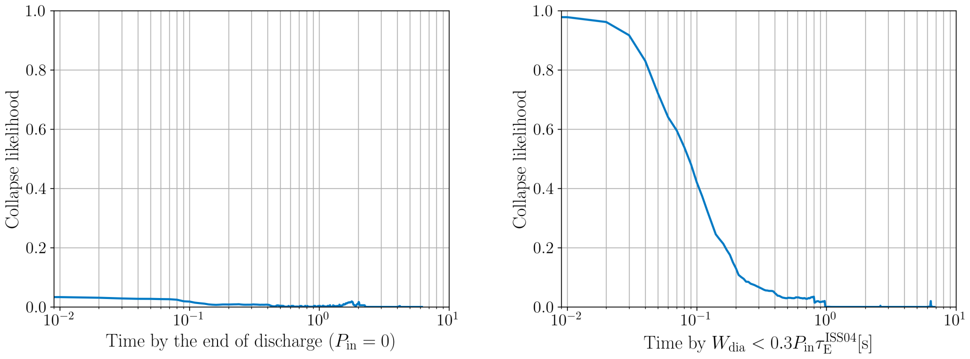

(a) (b)

Figure 3.7: (a) The collapse likelihood against time remaining until the end of the discharge in stable discharges. (b) The collapse likelihood against time remaining until the collapse in collapse discharges.

Table 3.3: Result of validation with data outside of the dataset [2].

Threshold likelihood	Success rate[%]	Missed rate[%]	Tardy rate[%]	Early rate[%]	False rate[%]
0.1	96.7	0.0	1.1	2.2	8.3
0.2	94.5	1.1	2.2	2.2	7.9
0.3	90.1	1.1	6.6	2.2	6.3
0.4	89.0	2.2	6.6	2.2	6.1
0.5	87.9	2.2	7.7	2.2	5.9
0.6	87.9	2.2	7.7	2.2	5.4
0.7	87.9	2.2	7.7	2.2	5.2
0.8	87.9	2.2	7.7	2.2	5.0
0.9	84.6	2.2	11.0	2.2	4.3

Table 3.4: Alarm time of prediction in validation with data outside of the dataset [2].

Threshold likelihood	Mean[ms]	Std[ms]
0.1	142.5	147.9
0.2	131.6	142.4
0.3	123.1	139.3
0.4	118.5	138.1
0.5	115.3	137.0
0.6	110.9	135.7
0.7	107.8	135.5
0.8	101.5	127.4
0.9	89.9	98.9

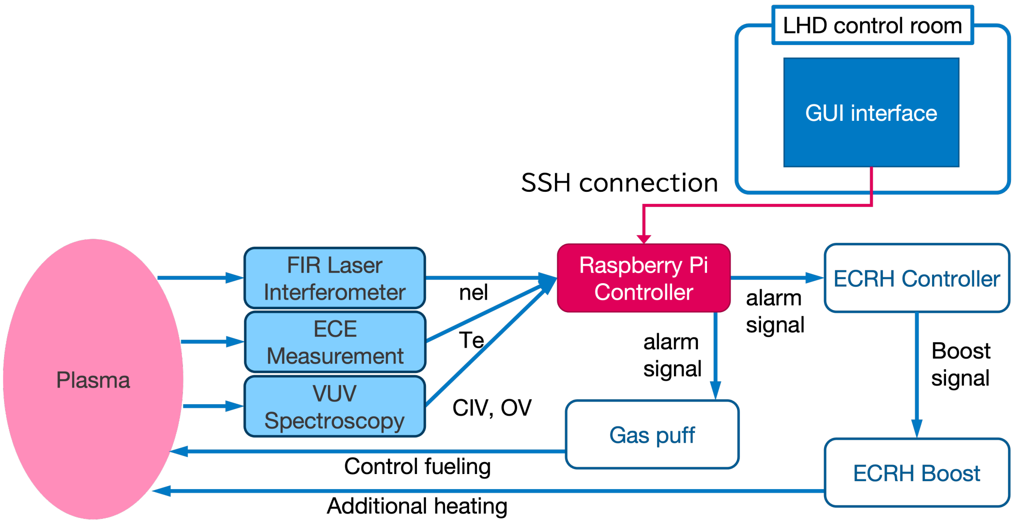

Figure 3.8: Schematic diagram of the collapse avoidance control system.

3.2 Real-time control to avoid radiative collapse in LHD

3.2.1 Collapse avoidance control system

A control system to avoid radiative collapse in high-density experiment in LHD has been developed based on the collapse likelihood. According to the decision function (3.1) and the collapse likelihood (3.2), reducing plasma density and raising edge temperature will be effective to reduce the likelihood, in other words, to prevent the occurrence of collapse. This control corresponds to shifting the plasma state in the direction toward the lower right in the Fig. 3.6. Therefore, gas puff fueling and ECRH have been employed as actuators of the control system.

The schematic diagram of the control system is shown in Fig. 3.8. The signals of plasma parameters which are selected by the feature extraction are input to the controller, i.e., $\bar{n}_e$, CIV, OV, and T_e. The controller calculates the collapse likelihood based on the input signals and compares the likelihood with the threshold value in real-time. When the likelihood exceeds the threshold, the output alarm signal turns gas puff on and the ECRH off.

Inpurt parameters

As input signals, $\bar{n}_e$, CIV, OV, and T_e have been used in the control system. As in the dataset for the machine learning, $\bar{n}_e$ is obtained by the FIR laser interferometer, and CIV and OV are obtained by the VUV spectroscopy.

As T_e, $T_\mathrm{e,edge}$ measured by the Thomson scattering measurement has been used in the dataset. However, its time resolution is 30 Hz, which is lower than the requirement of the control system. Therefore, $T_\mathrm{e,edge}$ has been replaced by $T_\mathrm{e,ECE}$, which is obtained by electron cyclotron emission (ECE) measurement with the channel that detects 146.5 GHz. Figure 3.9 shows the relationship $T_\mathrm{e,edge}$ and $T_\mathrm{e,ece}$ in the training dataset. The correlation coefficient of these parameters is 0.964, indicating a high linear relationship, so that it is reasonable to substitute $T_\mathrm{e,ece}$ for $T_\mathrm{e,edge}$. The $T_\mathrm{e,ECE}$ corresponds to the electron temperature near the center of the plasma, and only available in experiments with B_t =2.75 T. Here, changing the parameter requires recalculating the decision function and the collapse likelihood. The SVM has been trained again with $\bar{n}_\mathrm{e}$, CIV, OV, and $T_\mathrm{e,ECE}$ using available data in the training dataset. The decision function and the collapse likelihood for the control system, $f_\mathrm{ctrl}(\boldsymbol{x})$ and Likelihood$_\mathrm{ctrl}$, are calculated as follows:

$$f_\mathrm{ctrl}(\boldsymbol{x}) = \exp(2.10)\bar{n}_\mathrm{e}^{-0.600}\mathrm{CIV}^{1.31}\mathrm{OV}^{-0.129}T_\mathrm{e,ECE}^{-1.89}, \tag{3.5}$$

$$\mathrm{Likelihood}_\mathrm{ctrl} = \frac{1}{1+\exp\{-14.9\,(\log_{10} f_\mathrm{ctrl}(\boldsymbol{x}) + 0.283)\}}. \tag{3.6}$$

The prediction performance of Likelihood$_\mathrm{ctrl}$ is worse by about 5–10% than that of Likelihood: about 80% of collapse discharges more than 30 ms before the occurrence of the collapses.

Controller

A single-board computer, Raspberry Pi 4 Model B, with quad-core CPU, 8GB RAM, and general-purpose input/output (GPIO) interface, has been used as a controller[1]. The control programs which runs on the Raspberry Pi controller have been written in Python 3. Since Raspberry Pi does not have any analog input/output interfaces, an analog-digital converter (ADC) with 24-bit resolution[2] has been used to convert input analog signals into digital signals.

Voltage adjustment circuits have been employed to adjust the voltages of input signals to the input range of ADC, between 0 and 5 V. The diagram of the voltage adjustment circuits is shown in Fig. 3.10. Op-amp #1 (OA1) is for voltage follower circuit, while op-amp #2 (OA2) is for subtraction circuit. Here, V_input and V_out are the input and output signal, respectively. V_bias is the bias voltage of 15 V, which is common to the power supply to op-amps. As op-amps, NJM4556A has been used. The parameters of components in the circuit are described in Table 3.5. Figure 3.11 shows the photographs of the controller.

---

[1] `https://www.raspberrypi.org/products/raspberry-pi-4-model-b/`

[2] `https://www.seeedstudio.com/Raspberry-Pi-High-Precision-AD-DA-Board.html`

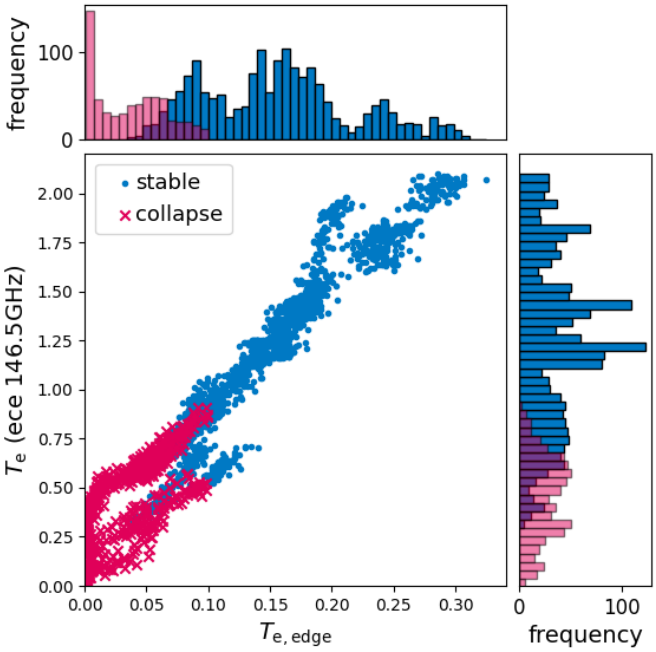

Figure 3.9: Relationship between $T_{\mathrm{e,edge}}$ and $T_{\mathrm{e,ece}}$ in the training dataset. Blue dots and orange crosses show “stable” and “close-to-collapse” data, respectively.

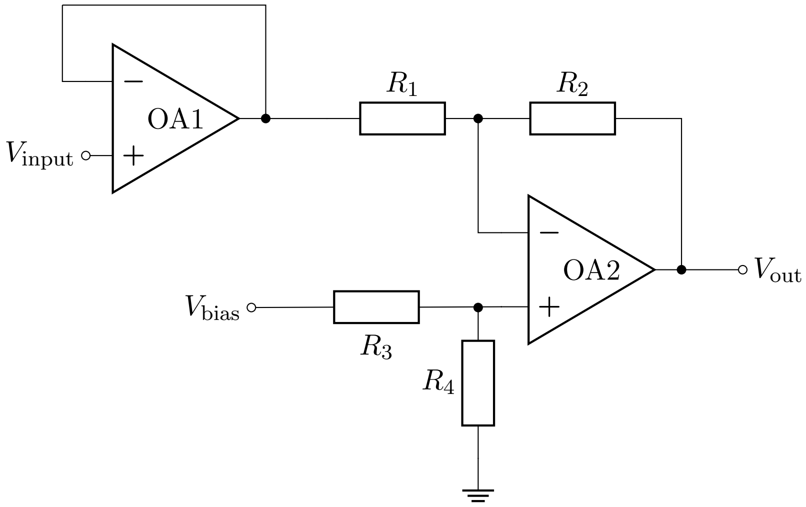

Figure 3.10: The circuit diagram of the voltage adjustment circuit.

Table 3.5: The parameters of components in the voltage adjustment circuit.

Parameters	V_{input} range	R_1	R_2	R_3	R_4
$\bar{n}_{\text{e}}$	±10 V	5 kΩ	1 kΩ	6.2 kΩ	1 kΩ
CIV, OV, and T_{e}	±5 V	5 kΩ	2 kΩ	7.4 kΩ	1 kΩ

The time interval of calculation is limited not only by the speed of the CPU on the Raspberry Pi but also by the speed of data transition between Raspberry Pi and ADC using Serial Peripheral Interface (SPI). In the present case, the time interval is about 8 ms, which is enough for control.

The threshold value and the parameters for calculating the likelihood can be changed through the SSH connection using the GUI interface, which runs on a computer connected to a local network.Figure 3.12 shows the GUI interface. When the “Start” button in the GUI interface is clicked, the Raspberry Pi controller becomes a trigger-wait state. Here, the trigger is sent when the plasma discharge starts, and is used in common in the LHD system. The controller starts to calculate the likelihood and output the alarm signal after the trigger is input.

Actuators

When the alarm signal is sent from the controller, the gas-puff control system turns off the fueling and additional power is injected by the ECRH. The gas puff is one of the main fueling source in LHD [55].

As ECRH, 77 GHz gyrotrons for the fundamental O-mode heating and 154

(a) (b)

Figure 3.11: Photographs of the controller. (a) The power source (left) and the case containing the Raspberry Pi and the voltage adjustment circuit (right). (b) The circuit board of the voltage adjustment circuit.

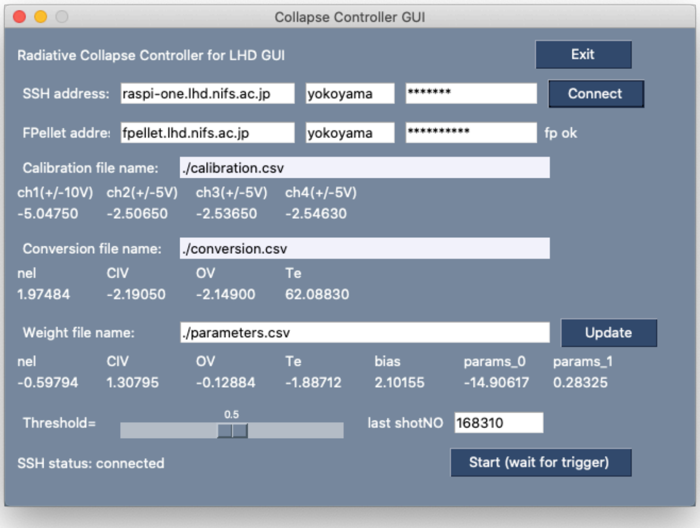

Radiative Collapse Controller for LHD GUI

SSH address: raspi-one.lhd.nifs.ac.jp yokoyama *******

FPellet addre: fpellet.lhd.nifs.ac.jp yokoyama ********** fp ok

Calibration file name: ./calibration.csv

ch1(+/-10V)	ch2(+/-5V)	ch3(+/-5V)	ch4(+/-5V)
-5.04750	-2.50650	-2.53650	-2.54630

Conversion file name: ./conversion.csv

nel	CIV	OV	Te
1.97484	-2.19050	-2.14900	62.08830

Weight file name: ./parameters.csv

nel	CIV	OV	Te	bias	params_0	params_1
-0.59794	1.30795	-0.12884	-1.88712	2.10155	-14.90617	0.28325

Threshold= 0.5

last shotNO 168310

SSH status: connected

Figure 3.12: The GUI interface for the control to avoid radiative collapse.

GHz for the second-harmonic X-mode heating are available. These are controlled by a real-time interlock system [66, 67]. Note that the time duration in which ECRH can be turned on is limited by its technical capability and the interlock system to avoid a blank injection.

3.2.2 Collapse avoidance experiment

The collapse avoidance with the control system has been attempted in density ramp-up experiments in LHD. Figure 3.13 shows two typical discharges in hydrogen plasma, with and without collapse avoidance control. In these discharges, the plasma has been sustained by gas-puff fueling and NBI heating. The ECRH has been used to initiate plasma, while two 154 GHz gyrotrons have been reserved for boost injection.

In the discharge without control, shown by the dashed blue line, radiative collapse occurred in the early phase of the density ramp-up at around 3.6 s. In this case, the gas puff was injected constantly until a preset time (about 4.5 s).

On the other hand, in the discharge with control, shown by the solid red line, the radiative collapse in the early phase was avoided successfully by turning gas puff off and boosting ECRH. In this case, the threshold of the likelihood has been set as 0.9, which is shown by the dashed horizontal line in the top panel of Fig. 3.13.

Figure 3.14 shows close-up of collapse in early phase (3.45–3.65 s) in discharge without control shown in Fig. 3.13. According to Fig. 3.14, the change of the plasma towards the collapse in the early ramp-up phase, which is shown by the dotted line, was detected about 65 ms before the change occurred, which is earlier enough for margin of 30 ms for control. In the discharge with control, the gas puff was turned off within 10 ms after the controller detected the collapse. On the other hand, the boost ECRH was injected about 20 ms later the controller detected the collapse, while it is earlier enough than the collapse.

As shown in Fig. 3.15, the likelihood for the control system (Likelihood$_{\mathrm{ctrl}}$ in (3.6)) is compared with the likelihood calculated with $T_{\mathrm{e,edge}}$ (Likelihood in (3.2)), in the discharge with the collapse avoidance control system around the early phase collapse. At the moment of the collapse detection in the early phase, Likelihood$_{\mathrm{ctrl}}$ lagged Likelihood by tens of ms. This difference implies that the detection of the collapse can be made earlier by using original likelihood.

In the latter part of the discharge with control, the radiative collapse has been avoided only by turning on/off gas puff and $\bar{n}_{\mathrm{e}}$ was developed above $1.2 \times 10^{20}\,\mathrm{m}^{-3}$. In this phase, the ECRH was not available because of the technical limitation of duration time. When the change of NBI heating power occurred at around 5.3 s and 6.3 s, the predictor detected the occurrence of the radiative collapse and the high-density plasma was successfully sustained by the control. When

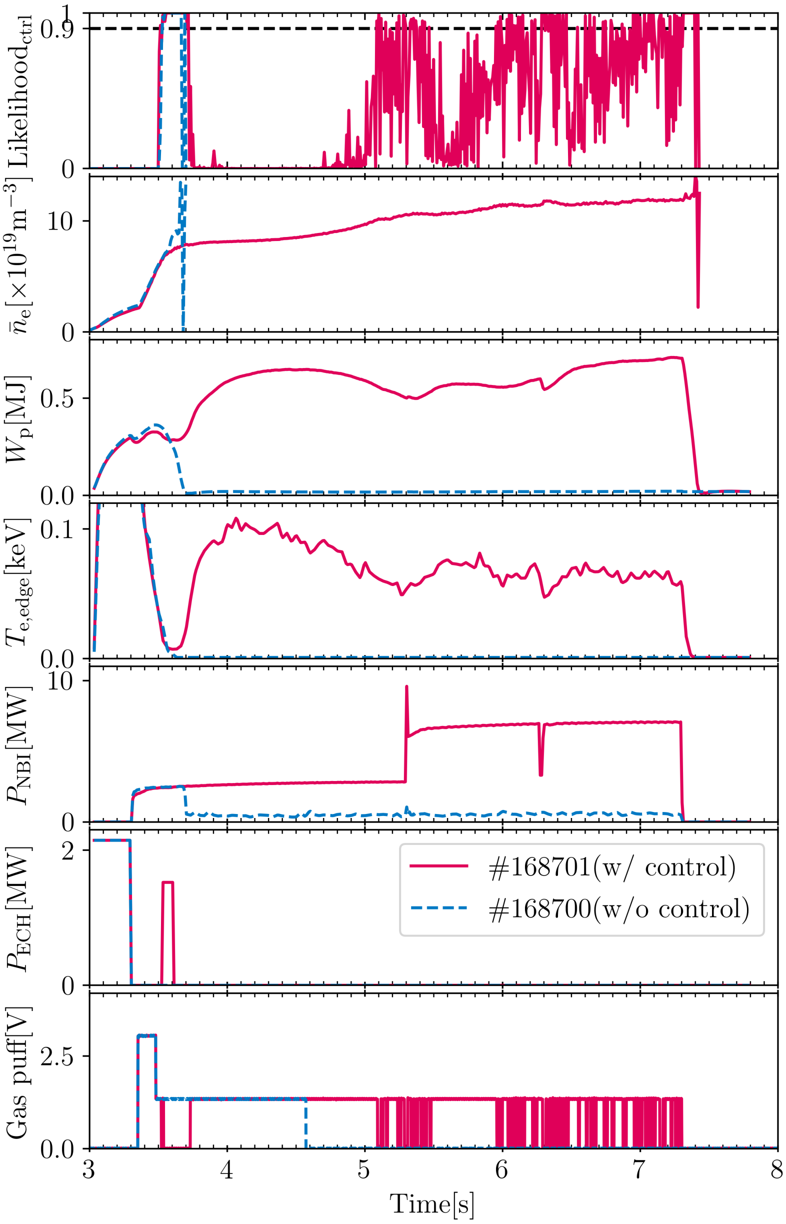

Figure 3.13: The discharges with and without collapse avoidance control in hydrogen plasma, shown by red and blue lines, respectively.

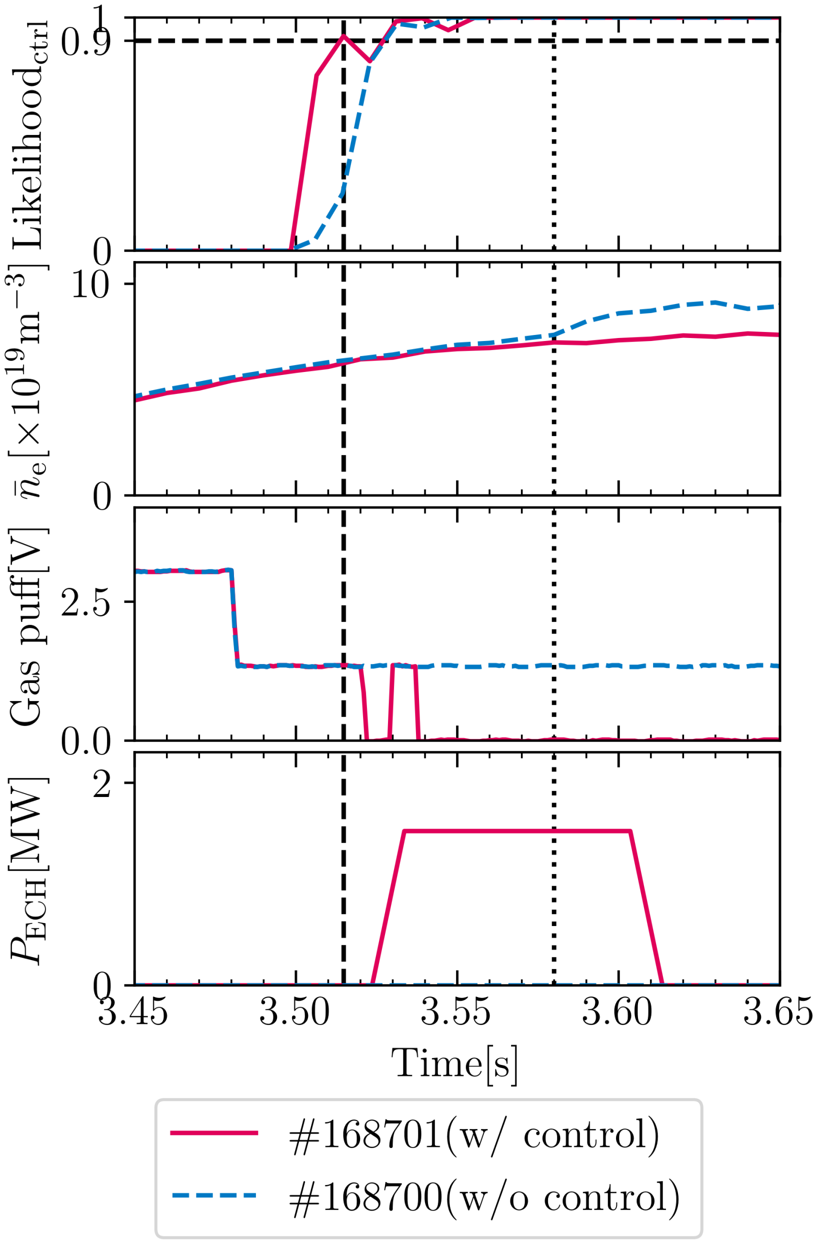

Figure 3.14: Close-up of early phase (3.45–3.65 s) of discharges shown in Fig. 3.13. The vertical dashed and dotted lines show the moment when the predictor detected the collapse and when the plasma density in #168700 started to increase toward the collapse, respectively.

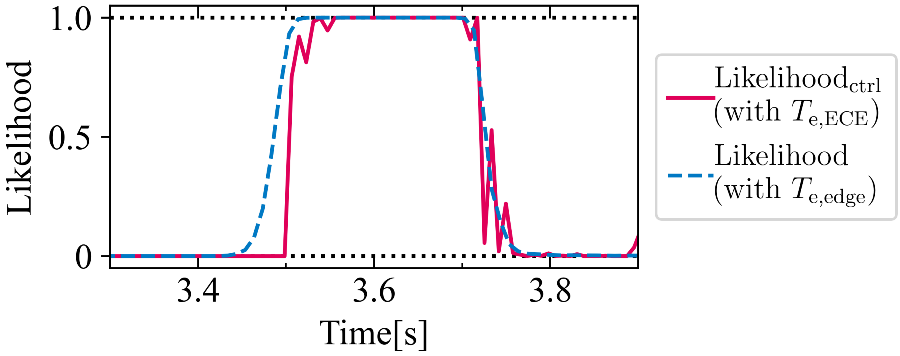

Figure 3.15: The likelihood in discharge with collapse avoidance control system (#168701) from 3.3 s to 4.0 s. The likelihood used in the control system and the original one are drawn by red-solid line and blue-dashed line, respectively.

the collapses were avoided, the recoveries of electron temperature $T_{\text{e,edge}}$ and diamagnetic energy W_{p} were observed.

Impact of boost ECRH on collapse avoidance

Collapse avoidance with only boost ECRH has been attempted in other discharges with hydrogen plasma. In these cases, the collapse in early phase has not been avoided to date. The typical discharge in which collapse avoidance was attempted with only boost ECRH is shown in Fig. 3.16. The deposited power density of ECRH heating shown in panel (iv) is calculated by upgraded version of LHDGauss code [68]. According to Fig. 3.16, ECRH power was deposited at $r_{\text{eff}}/a_{99} \sim 0.1$. The ECRH power was stopped at 3.6 s by the interlock without avoiding collapse. This fact indicates that the heating core plasma is not effective to avoid radiative collapse. This agrees with the result of feature extraction that implies the edge temperature and low-Z impurity radiation are important in the collapse, described in section 3.1. Therefore, the collapse may be avoided by heating the plasma edge efficiently. To resolve this problem, off-axis injection of ECRH has been attempted.

Additional experiments to avoid radiative collapse by off-axis ECRH have been conducted in deuterium plasma discharges. Figure 3.17 shows the results of these experiments. In these experiments, the number of 154 GHz gyrotrons reserved for boost ECRH has increased by one to three, and thus the injected ECRH power has increased from the previous experiments, which is shown in Fig. 3.16. It should be also noted that the measurement position of $T_{\text{e,ECE}}$ was moved outward by a few centimeters because the frequency that is detected by the ECE measurement to obtain $T_{\text{e,ECE}}$ was changed from 146.5 GHz to

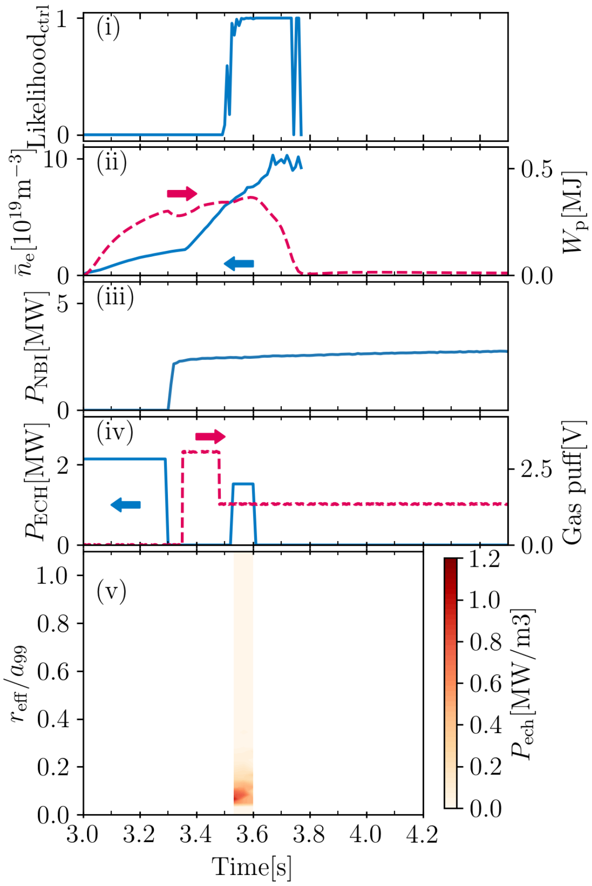

Figure 3.16: (i)Collapse likelihood calculated in real-time, (ii) line averaged electron density $\bar{n}_{\mathrm{e}}$ and stored energy W_{p}, (iii) NBI port through power , (iv) ECRH power P_{ECH} and gas puff signal, and (v) deposited ECRH power density calculated by LHDGauss code in the typical discharge in which collapse avoidance was attempted with only boost ECRH (#168698).

145.5 GHz by technical reason. In addition, the evacuation was improved by divertor pump in these experiments.

In Fig. 3.17 (a), off-axis injection of focusing at $r_{\mathrm{eff}}/a_{99} \sim 0.4$ has been attempted. The achieved electron density is lower than the previous experiments. In this discharge, the NBI injection power has been doubled to achieve higher density, as shown in the panel (iii) of Fig. 3.17 (a). The radiative collapse detected as shown in the likelihood (shown in panel (i)) has not been avoided, while the ECRH power is deposited at around $r_{\mathrm{eff}}/a_{99} \sim 0.4$ as designed.

In the discharge shown in Fig. 3.17 (b), off-axis injection of focusing at $r_{\mathrm{eff}}/a_{99} \sim 0.6$ has been attempted. The NBI injection power has been similar to the previous discharge, as shown in the panel (iii) of Fig. 3.17 (b). At around 3.6 s, a collapse was detected and avoided by only boost ECRH. At this point, the ECRH power is deposited at around $r_{\mathrm{eff}}/a_{99} \sim 0.6$ as designed. Here, significant recovery of W_{p} is observed. Afterward, another collapse occurred at around 3.9 s, which the boost ECRH could not help. At this point, ECRH heating power is deposited in outer region ($r_{\mathrm{eff}}/a_{99} \sim 0.8$) and deposited power density is much smaller than that at around 3.6 s. It is probable that the collapse could not be avoided because of the small deposited power. One possible explanation of this is that the effectivity of ECRH is lower than designed value because of high electron density. The cut off density of the 154 GHz second-harmonic X-mode electron cyclotron (EC) wave is about $1.5 \times 10^{20}\,\mathrm{m}^{-3}$, which is larger than $\bar{n}_{\mathrm{e}}$ achieved in these experiments, but the ray of EC wave can be bent in high-density plasma, so that the ray cannot resonance as designed.

Consequently, the collapse can be avoided by off-axis boost ECRH pointing $r_{\mathrm{eff}}/a_{99} \sim 0.6$ in relatively low-density plasma. In high-density plasma, it is difficult to avoid the collapse by only ECRH because the ray of EC wave may be bent. It is required to control the polarization of ECRH considering the bending of rays according to the electron density to avoid collapse in high-density plasma by only ECRH.

Collapse avoidance in long-pulse discharge

The collapse avoidance control system has been applied to long-pulse discharge sustained only by ECRH, which is the major subject of LHD. In this case, the main ion was helium, not hydrogen or deuterium. In these discharges, a 154 GHz gyrotron has been reserved for boost injection, and another 154 GHz gyrotron and two 77 GHz gyrotrons have been used to sustain the plasma. As a result, the control system detected the occurrence of the radiative collapse, which is shown by the dashed line in Fig. 3.18. However, the detection of the collapse was too late to avoid it. This result is consistent with the validation of the collapse likelihood, described in section 3.1.4. The cause of this overlook is not identified

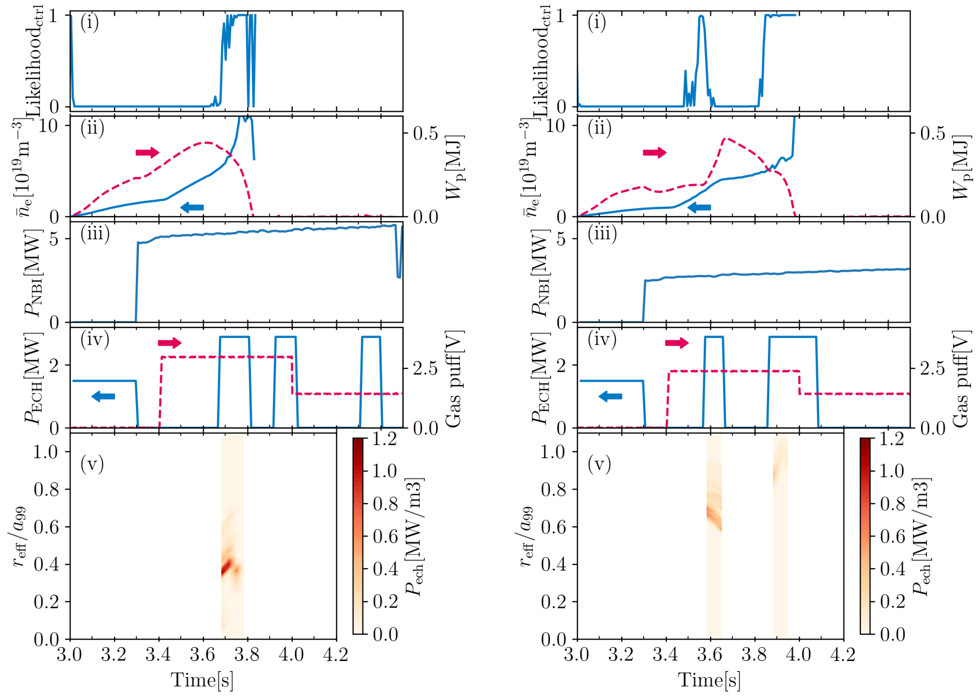

(a) #172450

(b) #172460

Figure 3.17: (i)Collapse likelihood calculated in real-time, (ii) line averaged electron density $\bar{n}_{\mathrm{e}}$ and stored energy W_{p}, (iii) NBI port through power, (iv) ECRH power P_{ech} and gas puff signal, and (v) deposited ECRH power density calculated by LHDGauss code in two discharges with off-axis ECRH injection. In (b) #172460, ECRH antenna is pointing more outwards than in (a) #172450.

yet, but control of fueling rate in helium plasma is generally difficult due to the high recycling of helium. The improvement of the prediction considering helium discharges is described later.

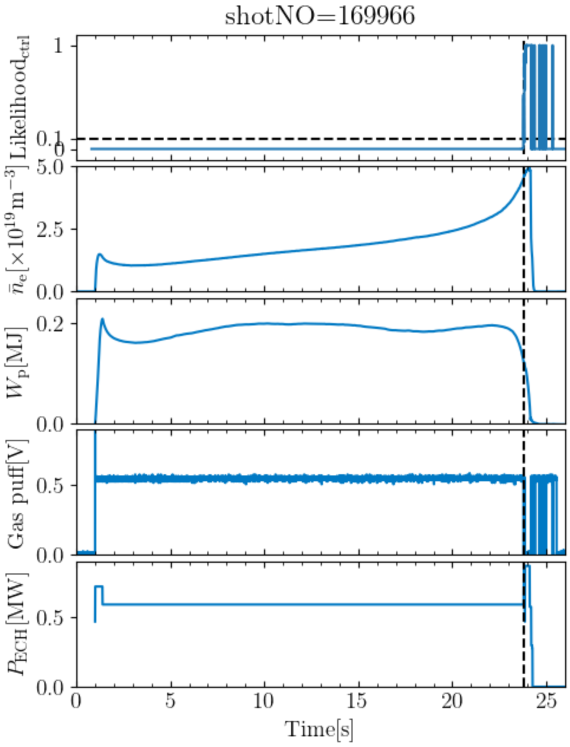

Figure 3.18: The long-pulse discharges with collapse avoidance control in helium plasma. The vertical dashed line shows the moment when the predictor detected the collapse.

3.2.3 Discussions of collapse avoidance

The behavior of collapse likelihood

The radiative collapse is likely to occur when $\bar{n}_{\mathrm{e}}$ is high according to (3.1), thus the reduction of $\bar{n}_{\mathrm{e}}$ is one possible way to avoid radiative collapse. However, the recovery of the likelihood was not accompanied with the decrease of $\bar{n}_{\mathrm{e}}$ according to Fig. 3.13. This is also seen in the contour plot of the likelihood against $\bar{n}_{\mathrm{e}}$ and other feature parameters, shown in Fig. 3.6. Figure 3.19 shows the trajectory of the discharges with and without control in the two-dimensional plane same as Fig. 3.6. Note that the likelihood shown in Fig. 3.6 is calculated with $T_{\mathrm{e,edge}}$

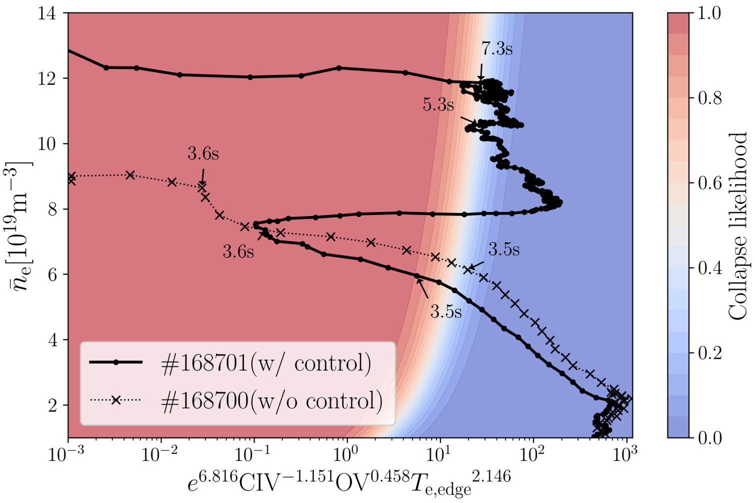

Figure 3.19: The trajectory of the discharges with and without control on the color contour which shows the likelihood of radiative collapse against line averaged density and other extracted parameters. The solid and dotted lines show the discharges with and without control, respectively.

and different from the likelihood used in the real-time control. In the discharge without control, which is shown by crosses in Fig. 3.19, once plasma entered the unstable (red) region, plasma went towards collapse. On the other hand, it is seen that the plasma returns from the unstable (red) region to the stable (blue) region by the control. Figure 3.20 shows that $\bar{n}_\mathrm{e}$ kept increasing ($\mathrm{d}\bar{n}_\mathrm{e}/\mathrm{d}t > 0$) even while the gas-puff fueling was turned off. During this time, recycling was reduced but not extinguished, as shown by H_α line emission in Fig. 3.20. This suggests that the fuel was supplied by the recycling from the vessel wall during the plasma was getting back to the stable region.

In the latter phase of the controlled discharge, the plasma stayed in the stable region near the boundary while the density increased. After the heating stopped at around 7.3 s, the plasma went into the unstable region and was terminated. This result shows that modulating gas-puff fueling is effective to keep plasma to stay in the stable region, and suggests that the higher plasma density can be achieved by the control system.

Particle transport analysis

Figure 3.21 shows the close-up of early phase of the discharge with collapse avoidance control system. According to the color contour plots of profiles of T_e and n_e, the plasma shrinkage was observed when the plasma approached collapse.

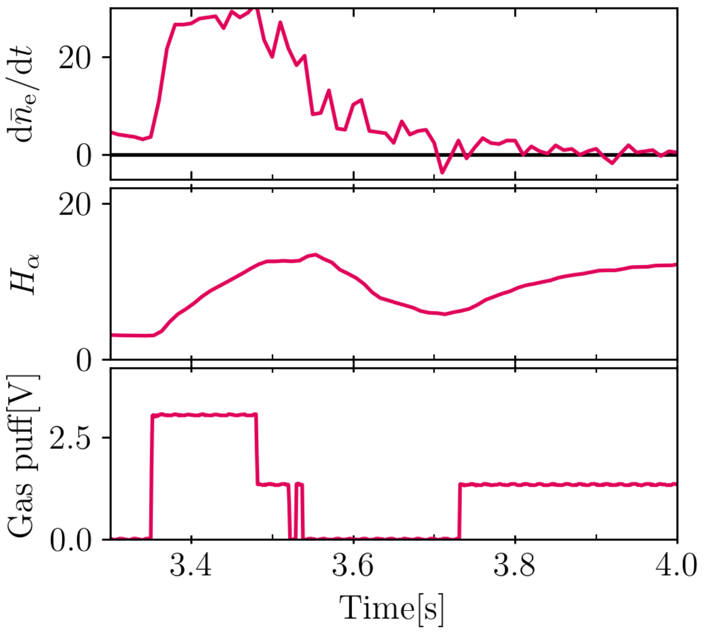

Figure 3.20: The temporal changes of $\bar{n}_\mathrm{e}$, H_α line emission, and the voltage signal that controls the gas puff in the discharge with collapse avoidance control system (#168701).

At the same time, humping high-n_e region appeared between plasma axis and edge region. When the plasma recovered, the shrinkage and the peak of n_e disappeared. To discuss these behaviors, particle transport has been analysed.

At a certain position represented by the minor radius r, equation of continuity of electron is expressed as follows:

$$\frac{\partial n_\mathrm{e}}{\partial t} = -\nabla \cdot \Gamma_\mathrm{e} + s_\mathrm{e}. \tag{3.7}$$

Here, Γ_e is the particle flux crossing the magnetic surface at that position and s_e is the source of electrons. The particle flux is denoted as follows:

$$\Gamma_\mathrm{e} = -D_\mathrm{e}\frac{\partial n_\mathrm{e}}{\partial r} + n_\mathrm{e} v_\mathrm{e}, \tag{3.8}$$

where D_e and v_e are the diffusion coefficient and convection velocity of electrons. Deforming (3.8), a linear relationship between $(-1/n_\mathrm{e}\mathrm{d}) \cdot (n_\mathrm{e}/\mathrm{d}r)$ and $\Gamma_\mathrm{e}/n_\mathrm{e}$ is expressed as follows:

$$\frac{\Gamma_\mathrm{e}}{n_\mathrm{e}} = D_\mathrm{e}\left(-\frac{1}{n_\mathrm{e}}\frac{\partial n_\mathrm{e}}{\partial r}\right) + v_\mathrm{e}. \tag{3.9}$$

Figure 3.22 shows the temporal change of relationship between $(-1/n_\mathrm{e}\mathrm{d}) \cdot (n_\mathrm{e}/\mathrm{d}r)$ and $\Gamma_\mathrm{e}/n_\mathrm{e}$ in the discharge with collapse avoidance control system at $r_\mathrm{eff} = 0.6\,\mathrm{m}$. Here, the electron flux Γ_e was calculated from (3.7). Applying Gauss's theorem to (3.7), Γ_e was denoted as follows:

$$\Gamma_\mathrm{e}(r) = \frac{1}{A(r)}\int_0^{V(r)}\left(s_\mathrm{e} - \frac{\partial n_\mathrm{e}}{\partial t}\right) dV \tag{3.10}$$

Here, $A(r)$ is the surface area of the flux surface at the radial position r.

The source term s_e has been evaluated with a diffusion model of neutral atoms for 1-dimensional cylindrical plasma [69]. The model considers the balances of particle and energy to give a distribution of neutral hydrogen atom. In this model, the ionization rate coefficient and charge exchange rate coefficient are assumed to be fixed to $1.0 \times 10^{-14}\,\mathrm{m^3/s}$. To calibrate the distribution, it has been assumed that the estimated outermost neutral pressure is equal to the neutral pressure measured in LHD.

In Fig. 3.22, the inclination and intercept of the regression line correspond D_e and v_e, respectively. In the shrinkage phase (between 3.4 s and 3.6 s), the data points are in line. The result of regression in this time range shows that $D_\mathrm{e} = 0.19\,\mathrm{m^2/s}$ and $v_\mathrm{e} = -1.9\,\mathrm{m/s}$.

Figure 3.23 shows the result of the particle transport analysis in a discharge without collapse in the early ramp-up phase. In this case, the inward convection velocity of $-1.4\,\mathrm{m/s}$ has been observed, which is slightly smaller than that in

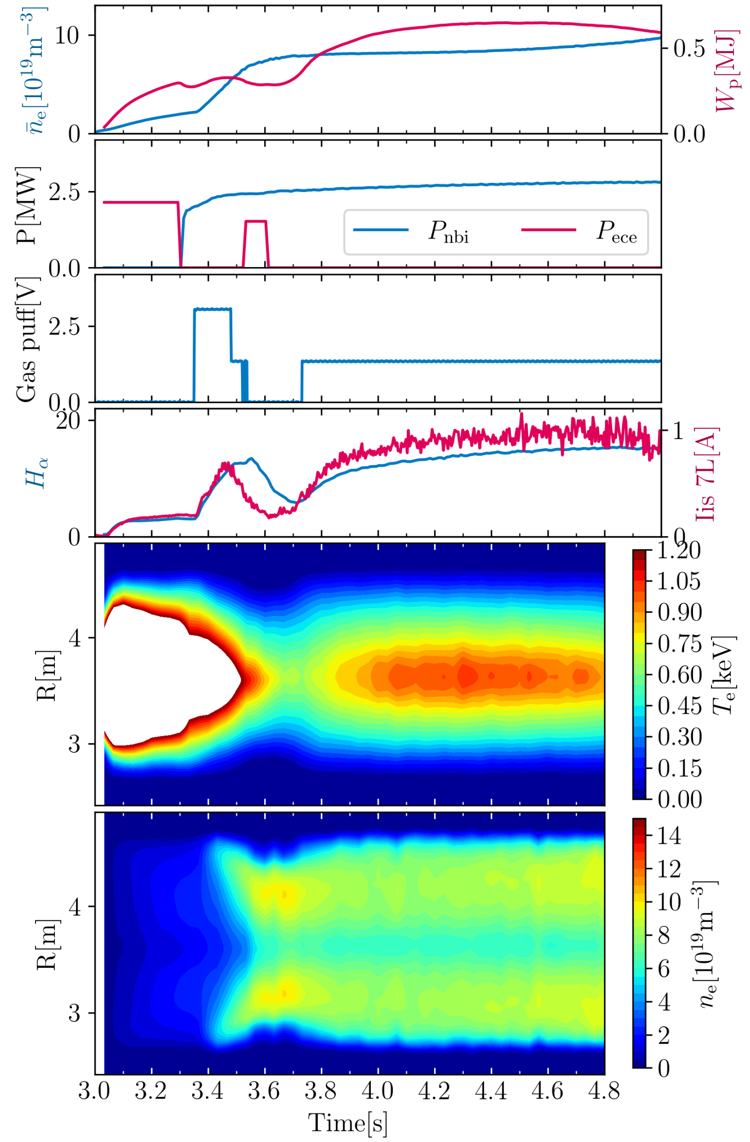

Figure 3.21: Close-up of early phase of the discharge with collapse avoidance control system (#168701). The profiles of T_e and n_e are shown as color contours.

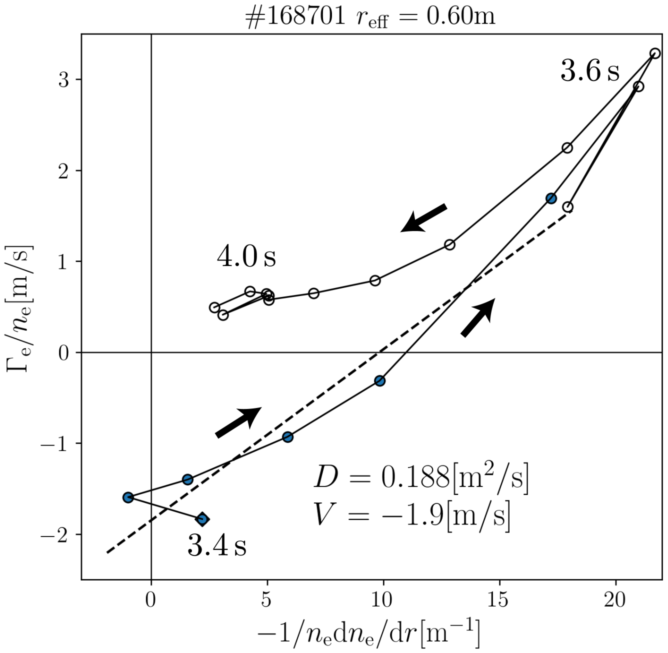

Figure 3.22: Temporal change of relationship between $-1/n_{\mathrm{e}}\mathrm{d}n_{\mathrm{e}}/\mathrm{d}r$ and $\Gamma_{\mathrm{e}}/n_{\mathrm{e}}$ in the discharge with collapse avoidance control system (#168701) from 3.4 s to 4.0 s. The dashed line is the regression line of colored data points.

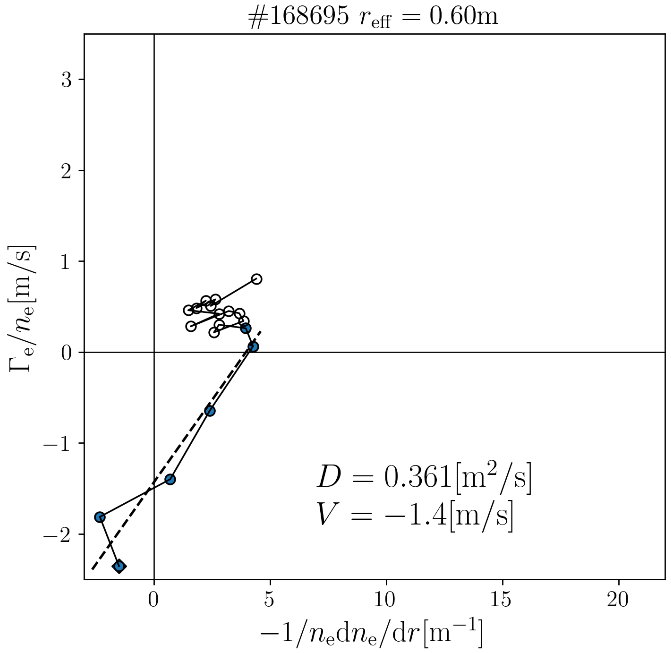

Figure 3.23: Temporal change of relationship between $-1/n_{\mathrm{e}}\mathrm{d}n_{\mathrm{e}}/\mathrm{d}r$ and $\Gamma_{\mathrm{e}}/n_{\mathrm{e}}$ in the discharge without collapse in early ramp-up phase (#168695) from 3.4 s to 4.0 s. The dashed line is the regression line of colored data points.

the collapse discharge. On the other hand, the diffusion coefficient is about twice larger than that in collapse discharge ($D_{\mathrm{e}} = 0.36\,\mathrm{m}^2/\mathrm{s}$). These result suggests that the imbalance between inward convection velocity and diffusion at the plasma edge region cause the shrinkage of plasma and the peak of n_{e}, which lead to collapse. After avoiding collapse, the inward convection was disappeared, which seems to correspond to the recovery of the plasma from the collapse.

Density fluctuation analysis

To investigate more about the cause and recovery process of radiative collapse, density fluctuation has been investigated using a two-dimensional phase contrast imaging (2D-PCI) measurement [70–72]. The 2D-PCI is one of laser scattering techniques, and $\mathrm{CO_2}$ laser is used for 2D-PCI in LHD.

Figure 3.24 and 3.25 show profiles of $\bar{n}_{\mathrm{e}}$ and $\mathrm{d}n_{\mathrm{e}}/\mathrm{d}r$, density fluctuation amplitude measured by 2D-PCI, power spectrum of fluctuation, and estimated radial electric field E_r. E_r is usually measured by CXS with perpendicular NBI in LHD. However, in the collapse avoidance experiment, no perpendicular NBI was used to make it easy to cause collapse. Therefore, E_r was estimated from equation of radial force balance. In typical fusion plasma with relatively low temperature of about $T_\mathrm{i} \sim T_\mathrm{e} \sim 1\,\mathrm{keV}$ and high n_e above $3 \times 10^{19}\,\mathrm{m}^{-3}$, E_r can be assumed as follows:

$$E_r \sim \frac{\nabla p_i}{Z_i e n_i}. \tag{3.11}$$

It is shown that the assumed E_r is in good agreement with the measured E_r in the edge region in stellarators [73], as well as tokamaks [74].

In the discharge with control shown in Fig. 3.24, the growth of density fluctuations and negative phase velocities were observed around the plasma between 3.5 s and 3.7 s when the plasma approached decay. In the reference discharge shown in Fig. 3.25, density fluctuation was observed in the same region as in the collapse discharge, but the fluctuation did not grow in this case.

Since PCI measurement is sensitive to high-frequency fluctuation, the observed fluctuation is thought to be a ion scale turbulent fluctuation, e.g., ion temperature gradient (ITG) mode and trapped electron mode (TEM). Note that it is difficult to identify the instability driving the fluctuation only by PCI measurement alone.

In this section, it is assumed that the measured density fluctuation is driven mainly by ITG mode. ITG mode is one of the drift wave instabilities that destabilized by ion temperature gradient [75]. Since the ITG mode is considered to be suppressed by radial electric field E_r in stellarator-heliotron devices [76], the relationship between the fluctuation and E_r is discussed bellow.

To discuss growth of ITG mode, ion temperature gradient normalized by density gradient η_i is usually used.

$$\eta_\mathrm{i} = \frac{\mathrm{d}T_\mathrm{i}/\mathrm{d}r}{T_\mathrm{i}} \frac{n_\mathrm{i}}{\mathrm{d}n_\mathrm{i}/\mathrm{d}r} = \frac{\mathrm{d}\ln T_\mathrm{i}}{\mathrm{d}\ln n_\mathrm{i}}. \tag{3.12}$$

Note that electron temperature and density have been used instead of ion temperature and density in this discussion because ion temperature and density have not been measure in the control experiments because of absence of tangential NBIs required to use CXS measurement.

According to theoretical studies, the radial electric field shear, which is equivalent to the mean $E \times B$ flow, plays an important role for the suppression of the turbulence [77]. The $E \times B$ shearing rate $\omega_{E\times B}$ is defined as follows:

$$\omega_{E\times B} = \frac{r}{q}\frac{\partial}{\partial r}\left(\frac{q}{r}\frac{E_r}{B}\right). \tag{3.13}$$

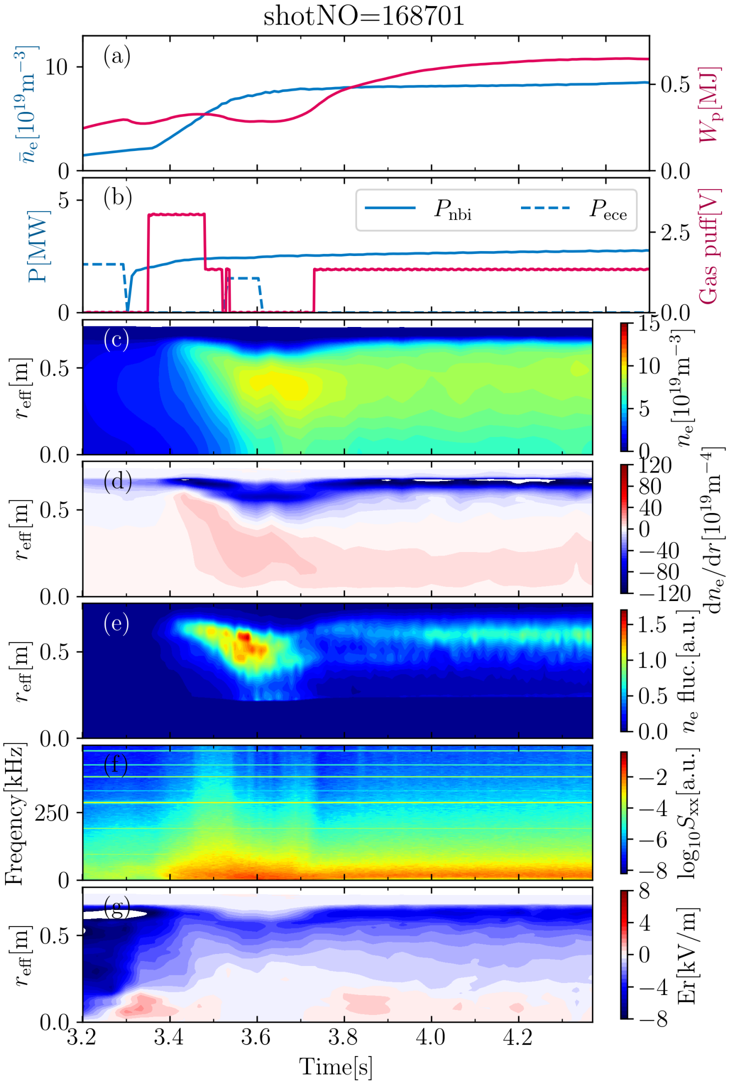

Figure 3.24: Time histories of (a) $\bar{n}_e$ and W_p, (b) input power and gas puff, (c) n_e profile, (d) $\mathrm{d}n_e/\mathrm{d}r$ profile, (e) density fluctuation amplitude, (f) power spectrum of fluctuation, and (g) radial electric field E_r in the discharge with collapse avoidance control system (#168701).

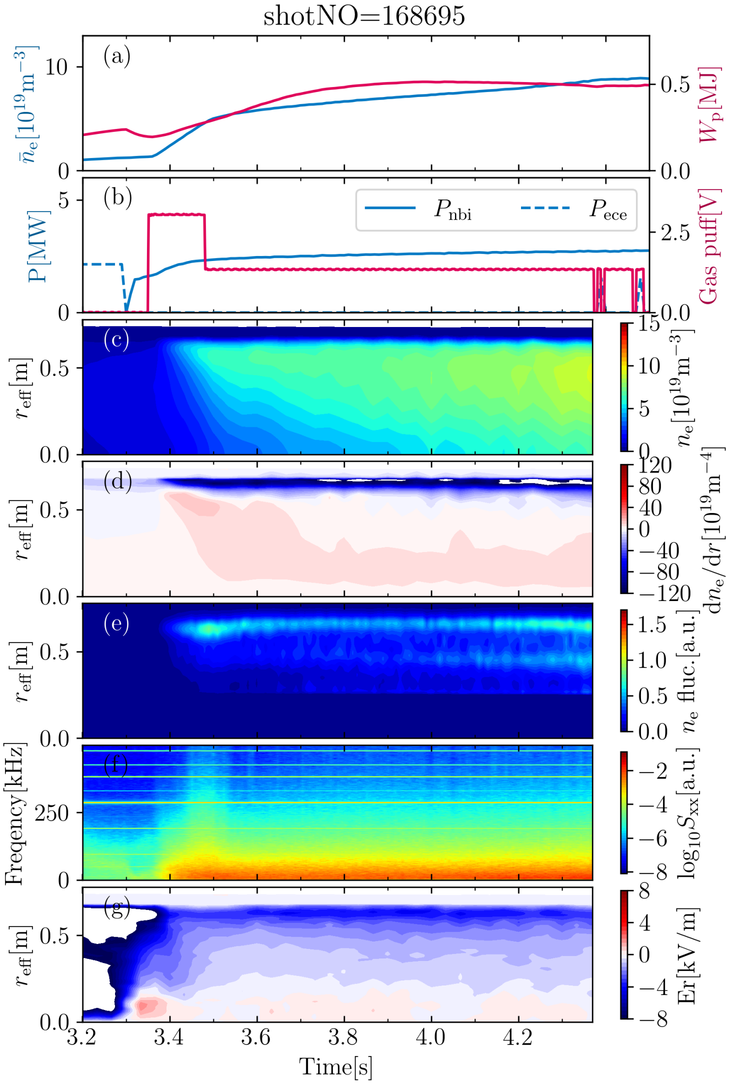

Figure 3.25: Time histories of (a) $\bar{n}_e$ and W_p, (b) input power and gas puff, (c) n_e profile, (d) $\mathrm{d}n_e/\mathrm{d}r$ profile, (e) density fluctuation amplitude, (f) power spectrum of fluctuation, and (g) radial electric field E_r in the discharge without collapse in early ramp-up phase (#168695).

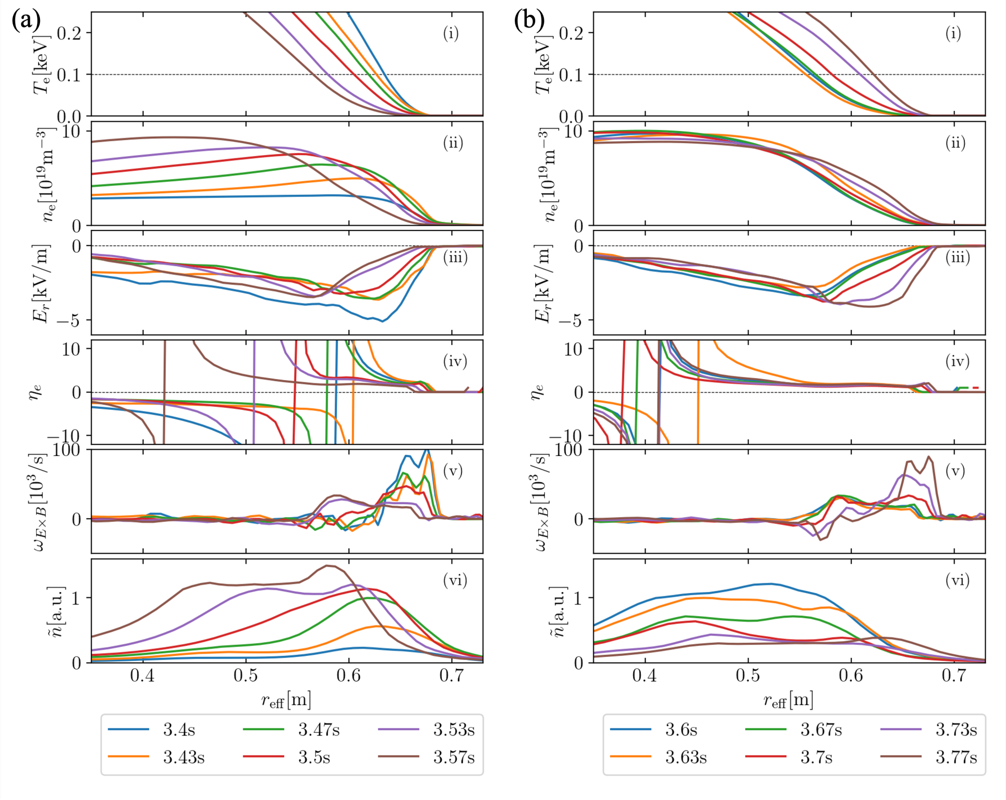

Figure 3.26: Radial profiles of (i) electron temperature T_e, (ii) electron density n_e, (iii) radial electric field E_r, (iv) temperature gradient parameter η_e, (v) $E \times B$ shearing rate $\omega_{E\times B}$, and (vi) density fluctuation amplitude when (a) plasma approached collapse and (b) plasma recovered from collapse.

Figure 3.26 shows the radial profiles of parameters related to ITG mode. When plasma was approaching collapse (shown in Fig. 3.26 (a)), density fluctuation first appeared in the edge region ($r_\mathrm{eff} > 0.6\,\mathrm{m}$) and propagated inward along with the region where the η_e is large. At the same time, edge $\omega_{E\times B}$ decreased. When plasma was recovering from collapse, edge $\omega_{E\times B}$ increased while the change of the region with large η_e is not so large.

Figure 3.27 shows the relationships between density fluctuation and absolute value of $E \times B$ shearing rate $|\omega_{E\times B}|$ at $r_\mathrm{eff} = 0.6\,\mathrm{m}$ in (a) the discharge in which collapse was avoided by control and (b) the stable discharge. In the collapse discharge shown in Fig. 3.27 (a), density fluctuation grew when $|\omega_{E\times B}|$ decreased. Then $|\omega_{E\times B}|$ increased and the fluctuation diminished, which is opposite to the outer position. Finally, $|\omega_{E\times B}|$ returned to low value, which is similar position

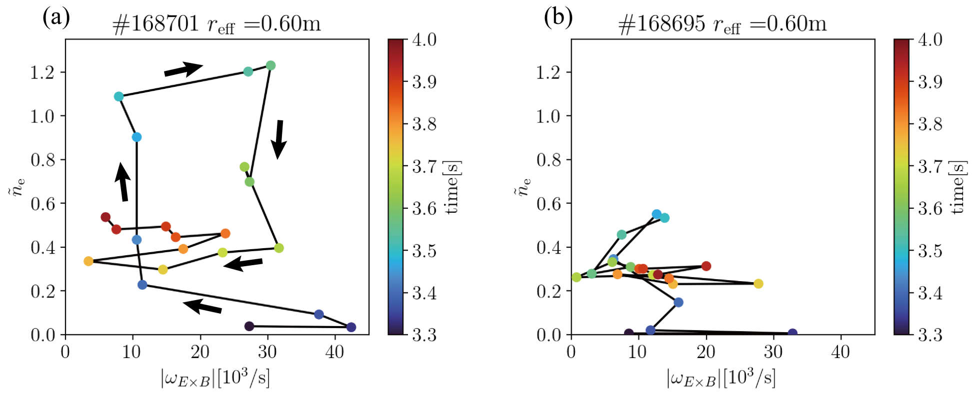

Figure 3.27: Relationships between density fluctuation and absolute value of $E \times B$ shearing rate $|\omega_{E\times B}|$ at $r_{\text{eff}} = 0.6\,\text{m}$ in (a) the discharge in which collapse was avoided by control and (b) the stable discharge. The colors of points correspond to the measuring times of Thomson scattering measurement.

as in the stable discharge shown in Fig. 3.27 (b).

According to prior researches in tokamak plasmas, the gradient of E_r when the instability is suppressed is larger than that measured in this discharge, and is on the order of $10^3\,\text{kV/m}^2$ [78, 79]. It is interesting that the increase and decrease of $|\omega_{E\times B}|$ seems to be related to the growth of turbulence while the observed $|\omega_{E\times B}|$ is not enough to suppress turbulence.

The characteristics in the plasma with collapse avoidance control discussed in the present section are summarized in Table 3.6. Further investigation focusing on impurity transport and MHD instabilities is required to explain how these features contribute to the onset of the radiative collapse.

Table 3.6: Characteristics of radiative collapse discussed in the present section. D_e and v_e are in the ramp-up phase.

Characteristics	Collapse discharge (#168701) Approaching collapse (3.5 s)	 Recovering from collapse (3.6 s)	Stable discharge (#168695) $\tilde{n}_\mathrm{e}$ and $\omega_{E\times B}$ are at 3.6 s
$D_\mathrm{e}[\mathrm{m}^2/\mathrm{s}]$	0.19	-	0.36
$v_\mathrm{e}[\mathrm{m/s}]$	-1.9	-	-1.4
$\tilde{n}_\mathrm{e}[\mathrm{a.u.}]$	1.09	0.699	0.310
$\omega_{E\times B}[10^3/\mathrm{s}]$	7.90	27.3	-8.78

3.3 Improvement of prediction of radiative collapse

It was shown that the radiative collapse prediction based on experiment data in hydrogen and deuterium plasma has not been quite successful for helium discharges yet in the sections above. Therefore, to improvement of the predicting model, the dataset to train the machine learning model was improved with data in helium plasma experiments.

In general, helium plasma can have higher electron density than hydrogen and deuterium plasma. When the FIR laser interferometer operates at a high electron density, a measurement miss so-called "fringe jump" is likely to happen at the moment of fast change of density. To avoid fringe jumps, line averaged electron density $\bar{n}_{\mathrm{e}}$ was obtained by the Thomson scattering measurement instead of FIR laser interferometer. Other changes of parameters considered in the dataset from Table 3.2 are as follows:

- HeI line intensity has been added.
- $I_{\mathrm{sat}}^{(7\mathrm{L})}$ has been removed.
- D/(H+D) has been removed.
- Effective mass M_{eff} and effective ion charge Z_{eff} have been added.

First, a new dataset has been constructed including experiment data in hydrogen, deuterium, and helium plasmas, shown in Table 3.1. The result of ES with this new dataset is shown in Fig. 3.28. According to Fig. 3.28, the F1-score is not so much improved from the result shown in Fig. 3.3, and the F1-scores that exceed the F1-score for using all parameters are seen for $K > 8$, which is more than the result with the conventional dataset. Consequently, the prediction has not been much improved by just adding data in helium plasma to the dataset.

Second, three datasets have been constructed considering only hydrogen, deuterium, and helium plasma data. The result of ES with this new dataset is shown in Fig. 3.29, Fig. 3.30, and Fig. 3.31, respectively. According to these results, the F1-scores are improved with less numbers of parameters by using dataset including only data for a particular ion. However, the combinations of feature parameters extracted by ES are different from each other, as shown in Table 3.7. This suggests that the predictor model constructed with data for a particular ion is not applicable for prediction in plasma with other ions.

Using the same method as described in section 3.1.3, the collapse likelihoods have been quantified with each combination of feature parameters shown in Table 3.7. The ion species used to estimate likelihood is expressed as a subscript, e.g., $\mathrm{Likelihood}_{\mathrm{H}}$ means likelihood for hydrogen plasma. To construct the likelihood which is applicable for collapses in plasma with any ions, these likelihoods

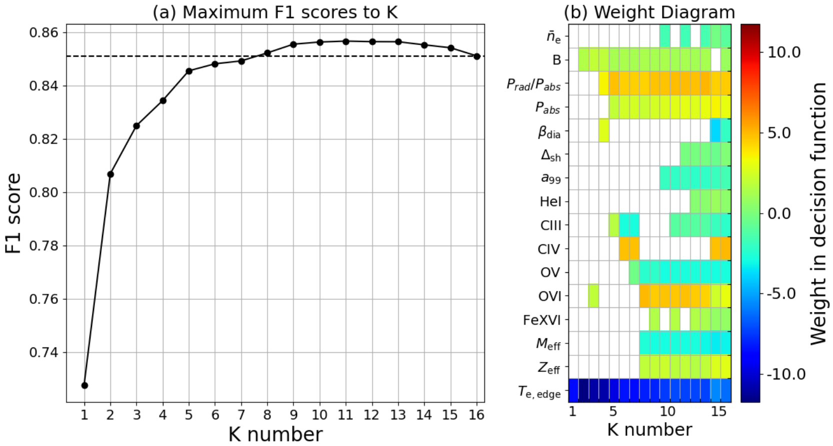

Figure 3.28: The result summary of ES with dataset considering hydrogen, deuterium, and helium plasmas. The left graph shows the best F1-score among combinations of K parameters. The horizontal dashed line shows the F1-score with all 16 parameters ($K = 16$). The right diagram shows the combination that gives the best F1-score among combinations of K parameters, which correspond to the left graph. The color bar corresponds to the weight w' in eq. 2.12.

Table 3.7: Feature parameters extracted from data for each ion.

Species	Feature parameters
H	P_{abs}, OVI, $T_{\text{e,edge}}$
D	B, CIV, $T_{\text{e,edge}}$
He	B, β_{dia}, OVI

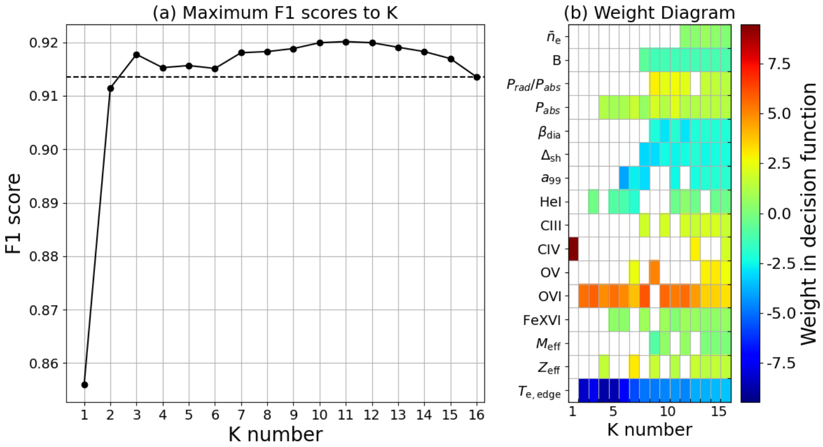

Figure 3.29: The result summary of ES with dataset with only hydrogen plasma. The left graph shows the best F1-score among combinations of K parameters. The horizontal dashed line shows the F1-score with all 16 parameters ($K = 16$). The right diagram shows the combination that gives the best F1-score among combinations of K parameters, which correspond to the left graph. The color bar corresponds to the weight w' in eq. 2.12.

have been integrated by taking the average weighted by the abundance ratio of each ion. The weighted-mean likelihood $\mathrm{Likleihood_{WM}}$ is denoted as follows:

$$\begin{aligned}\mathrm{Likelihood_{WM}} &= \frac{H}{H+D+He} \times \mathrm{Likelihood_{H}}\left(P_{\mathrm{abs}}, \mathrm{OVI}, T_{\mathrm{e,edge}}\right) \\ &= \frac{D}{H+D+He} \times \mathrm{Likelihood_{D}}\left(B, \mathrm{CIV}, T_{\mathrm{e,edge}}\right) \\ &= \frac{He}{H+D+He} \times \mathrm{Likelihood_{He}}\left(B, \beta, \mathrm{OVI}\right).\end{aligned} \tag{3.14}$$

Here, the ratio of H, D, and He ions are calculated by line intensities of H_α, D_α, and HeI.

The weighted-mean likelihood has been validated by the same method as section 3.1.4. The discharges in deuterium and helium plasma have been added to the target discharges in the validation. In total, 108 collapse discharges and 785 stable discharges have been considered in the validation.

Figure 3.32 shows the results of verification fixing threshold value to 0.8. According to this figure, the weighted-mean likelihood has shown the better performance than other likelihood. In Fig. 3.33, these likelihoods are compared with the conventional one in helium discharge with collapse, which was missed

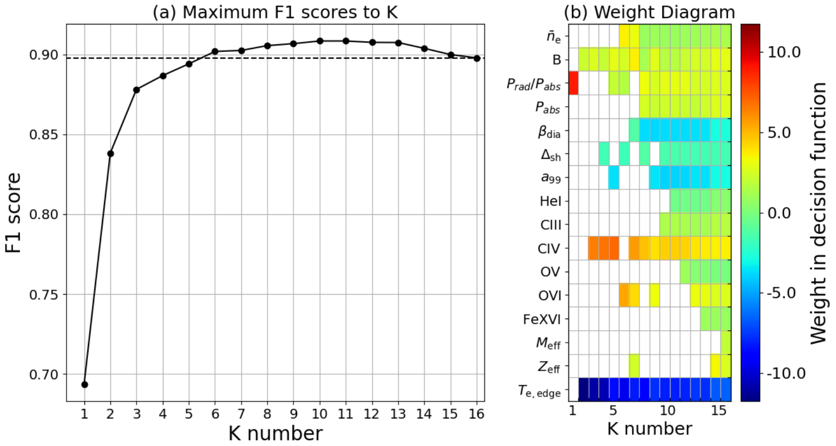

Figure 3.30: The result summary of ES with dataset with only deuterium plasma. The left graph shows the best F1-score among combinations of K parameters. The horizontal dashed line shows the F1-score with all 16 parameters ($K = 16$). The right diagram shows the combination that gives the best F1-score among combinations of K parameters, which correspond to the left graph. The color bar corresponds to the weight w' in eq. 2.12.

in verification with the conventional likelihood. The weighted-mean likelihood $\text{Likleihood}_{\text{WM}}$ and the convectional one Likleihood are shown in the the bottom panel by solid and dashed lines, respectively. The increase of $\text{Likleihood}_{\text{WM}}$ is earlier than that of Likleihood and it can be said that the prediction of collapse in helium discharge is improved by using weighted-mean method.

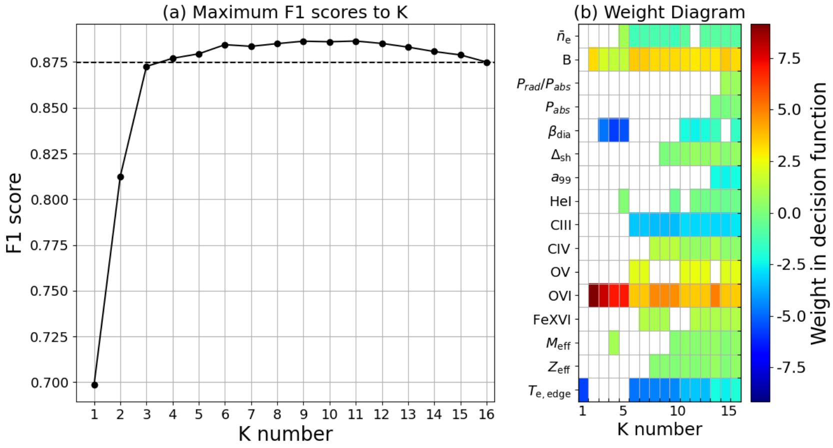

Figure 3.31: The result summary of ES with dataset with only helium plasma. The left graph shows the best F1-score among combinations of K parameters. The horizontal dashed line shows the F1-score with all 16 parameters ($K = 16$). The right diagram shows the combination that gives the best F1-score among combinations of K parameters, which correspond to the left graph. The color bar corresponds to the weight w' in eq. 2.12.

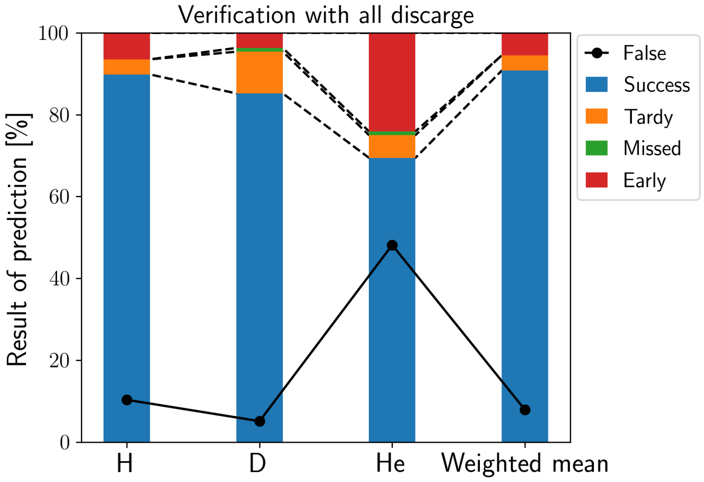

Figure 3.32: Verification results for $\text{Likelihood}_\text{H}$, $\text{Likelihood}_\text{D}$, $\text{Likelihood}_\text{He}$, and $\text{Likelihood}_\text{WM}$ fixing threshold value to 0.8.

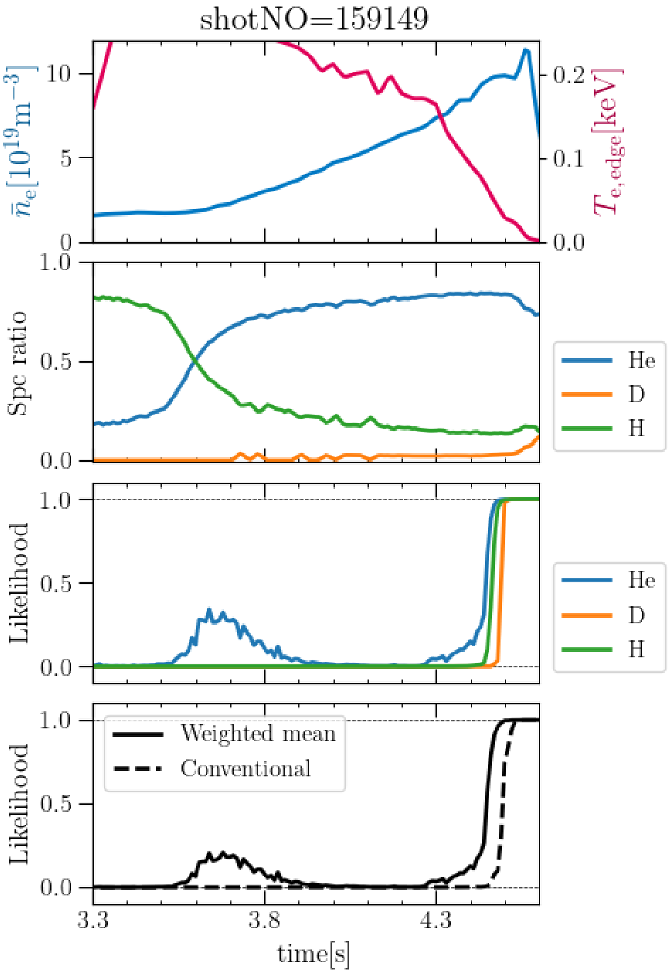

Figure 3.33: The waveforms of likelihood in helium discharge (#159149).

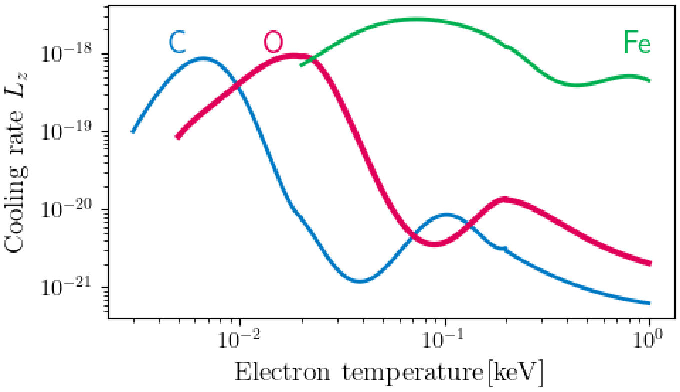

Figure 3.34: Cooling rate of carbon (C), oxygen (O), and iron (Fe) against electron temperature (based on [5]).

3.4 Discussion of physical background of radiative collapse

According to the decision function (3.1), light impurities, especially carbon, seem to be important. This result agrees with previous theoretical research [19]. The light impurities are main radiators at the plasma edge region, and $T_{\mathrm{e,edge}}$ has been selected by ES. Especially in LHD, carbon is major radiator since the plasma facing material of divertor plates is isotropic graphite [80]. It should be noted that most of the $T_{\mathrm{e,edge}}$ values used in the dataset are distributed around 100 eV, while the radiation rate of carbon has the first peak around 10 eV in equilibrium state, as shown in Fig. 3.34 [5].

The behaviors of plasma and carbon impurities outside the LCFS have been evaluated by the EMC3-EIRENE [81–83] code. EMC3-EIRENE solves a steady-state distribution of the plasma and impurity using fluid equations along magnetic field lines and with cross-field diffusion, and determines a distribution of the neutral particles by the Monte-Carlo scheme. The calculations were conducted eight time slices in the discharge with a radiative collapse in LHD, which is shown in Fig. 3.35. The magnetic configuration of this discharge is as follows: the magnetic axis position was R_{ax} =3.6 m and the magnetic field at the magnetic axis in vacuum was 1.375 T. Around 4.6 s, a radiative collapse occurred and the plasma went to termination. The dotted lines in the figure correspond to the time slices when the plasma behavior is calculated by the EMC3-EIRENE. The calculation time window has been selected to cover the time range when the collapse likelihood grew from zero to one. In these simulations, the diffusion coefficient of carbon D_C and the carbon sputtering yield were fixed so that the distribution of C^{6+} ion becomes close to that was measured by charge exchange spectroscopy [84] at 4.31 s. Note that the impurity source is at the divertor plates. The absorbed power of NBI heating is estimated by TASK3D, which is an integrated transport simulation code [85], for each time slice. It has been confirmed that the total radiation power calculated at each time slice (shown by crosses) agrees with those measured by a bolometer, shown in the bottom panel of Fig. 3.35.

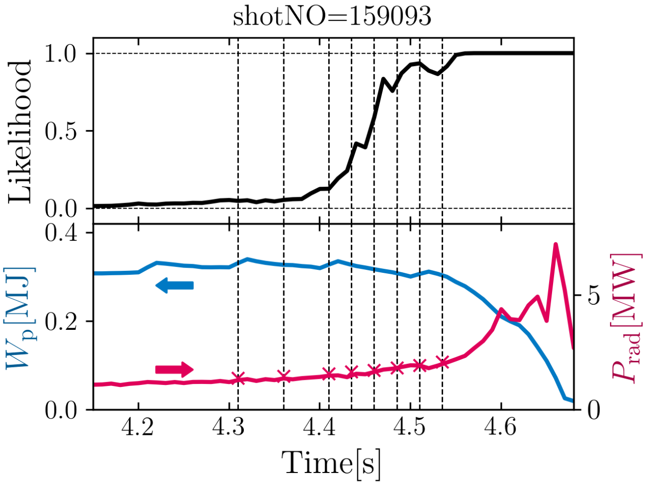

Figure 3.35: The waveform of reference discharge with radiative collapse for EMC3-EIRENE simulation. The crossed in the bottom panel shows the total radiation power calculated at each time slice.

Since the CIV line emission has been selected as the feature parameter by ES, the behavior of C^{3+} ion, which corresponds to the CIV line emission, has been mainly investigated. Figure 3.36 shows the calculated distributions of C^{3+} ion near the outer X-point at the horizontally elongated cross-section with double null points on the equatorial plane for each time slice. The regions where C^{3+} ions are accumulated expand as time goes. Then two peaks appear above and below the midplane, and finally, these two separated peaks marge on the midplane.

Figure 3.37 shows the distributions of electron density, electron temperature, cooling rate of C^{3+} ion ($L_{\mathrm{C}^{3+}}$), C^{3+} ion density, $n_{\mathrm{C}^{3+}}$, and radiation power by C^{3+} ($P_{\mathrm{C}^{3+}}$), at the beginning (4.31 s) and the end (4.51 s) of the change of the likelihood. Here, $L_{\mathrm{C}^{3+}}$ has been calculated based on atomic data in OPEN-ADAS [86], and $P_{\mathrm{C}^{3+}}$ is used as an alternative of CIV line emission in this discussion. As the plasma is getting close to the collapse, electron density n_e

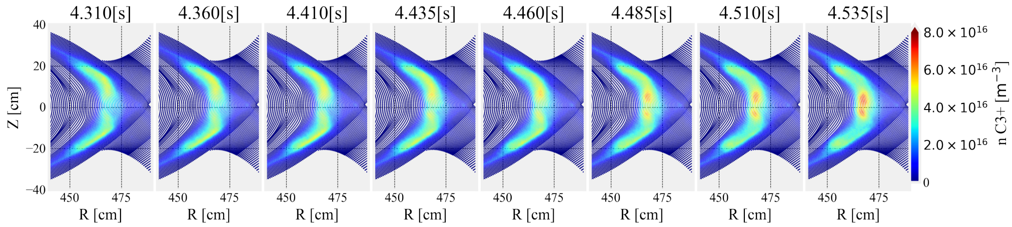

Figure 3.36: The calculated distributions of $n_{\mathrm{C}^{3+}}$ near the outer X-point of LHD at each time points shown by dotted lines in Fig. 3.35.

and temperature T_{e} increased and decreased respectively. The distributions of $n_{\mathrm{C}^{3+}}$ and $P_{\mathrm{C}^{3+}}$ at 4.51 s are similar to each other, while those at 4.31 s are quite different.

There are two major difference between the relationships of $n_{\mathrm{C}^{3+}}$ and $P_{\mathrm{C}^{3+}}$ at 4.31 s and 4.51 s. The first one is that $P_{\mathrm{C}^{3+}}$ at 4.31 s and 4.51 s are different in the region with similar $n_{\mathrm{C}^{3+}}$ of about $4 \times 10^{16}\,\mathrm{m}^{-3}$. According to (1.15), the radiation power is defined not only by the impurity ion density n_{imp} but also electron density n_{e} and cooling rate L_Z, which is a function of T_{e} [19]. Therefore $P_{\mathrm{C}^{3+}}$ increases while $n_{\mathrm{C}^{3+}}$ stays similar in time because of the change of n_{e} and T_{e} in this region. In the region where $P_{\mathrm{C}^{3+}}$ increases, n_{e} increases to around $4 \times 10^{19}\,\mathrm{m}^{-3}$ and T_{e} decreases to around 10 eV or less, according to Fig. 3.37. This results is consistent with the temperature at the maximum cooling rate of carbon. This temperature range lies below the region subject to the present estimation of the likelihood and the previous researches of density limit [18]. Note that the decrease in T_{e} is not equal to the increase in $L_{\mathrm{C}^{3+}}$, as shown in Fig. 3.37 (c) and (h). Therefore, the increase in n_{e} in this region seems to play an important role in the occurrence of radiative collapse.

The second one is that there are two peaks in distributions of $n_{\mathrm{C}^{3+}}$ and $P_{\mathrm{C}^{3+}}$ at 4.51 s. This indicates the increased concentration of C^{3+} ions can cause high radiation. To understand the cause of the peaking of C^{3+} ion, the profiles of $n_{\mathrm{C}^{3+}}$ and ionization rate from C^{2+} to C^{3+}, which is the main source of the C^{3+} ion, along the flux tube which goes through the peak of $n_{\mathrm{C}^{3+}}$ in $z > 0\,\mathrm{m}$ at 4.51 s have been investigated. The 3D view of the flux tube along which these profiles have been investigated is shown in Fig. 3.38, and the temporal changes of these profiles are shown in Fig. 3.39. The flow of C^{3+} ion has the negative direction along the flux tube, which means the flow direction is against the direction of toroidal magnetic field. The zero points of horizontal axes in Fig. 3.39 corresponds to the peak in horizontally elongated cross-section shown in Fig. 3.36. The density at the peak increased with time, while the ionization rate has a peak upstream of the peak of the density. The peak of ionization

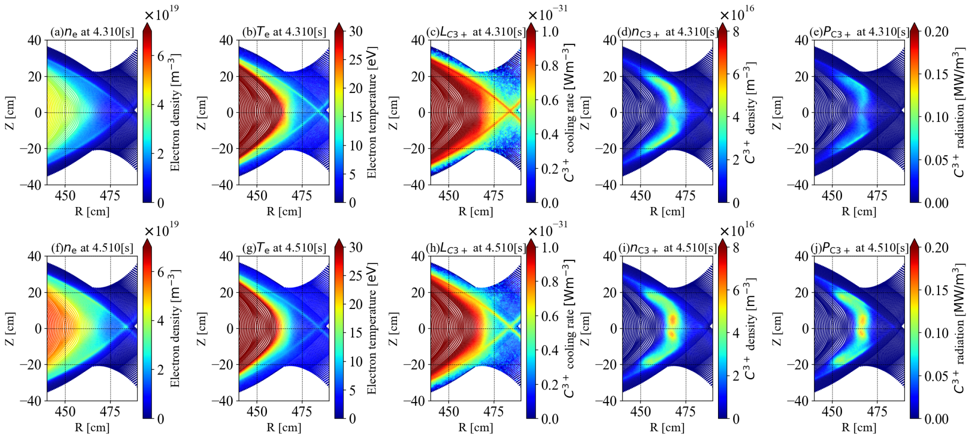

Figure 3.37: Simulation results near the outer X-point of LHD of (a, f) electron density, (b, g) electron temperature, (c, h) C^{3+} cooling rate, (d, i) C^{3+} ion density, and (e, j) radiation power by C^{3+} ion at (a, b, c, d, e) 4.31 s and (f, g, h, i, j) 4.51 s.

rate has the largest value at 4.485 s, which corresponds to the largest change of $n_{C^{3+}}$ occurred between 4.46 s and 4.485 s. This similarity indicates that the distribution of C^{3+} ion is defined by the change of upstream transport of C^{3+} ion. Here, the ionization rate from C^{2+} to C^{3+} depends on $n_{C^{2+}}$ as well as n_e and T_e. Therefore, more investigation of 3D impurity transport considering atomic model in stochastic layer is necessary to understand the role of carbon impurity leading to radiative collapse.

Validity of simulation results

To validate the reliability of the simulation results, synthetic reproduction of the measured values of feature parameters ($\bar{n}_e$, CIV, OV, and $T_{e,edge}$) from the calculation results of EMC3-EIRENE has been attempted. Using these reconstructed values, the collapse likelihood has been estimated based on the simulation results to compare with the likelihood calculated based on the measured value.

For $\bar{n}_e$ and $T_{e,edge}$, the lines of sight of FIR measurement and Thomson scattering measurement have been reproduced as shown in Fig. 3.40. $T_{e,edge}$ is defined as an mean value of T_e at inboard and outboard sides of LCFS at vacuum, shown as crosses in Fig. 3.40 (b) , which is as same as the definition used in construction of the dataset.

In the simulation, the abundance of oxygen impurities is negligibly small. Therefore contribution of OVI line emission to the likelihood is neglected in

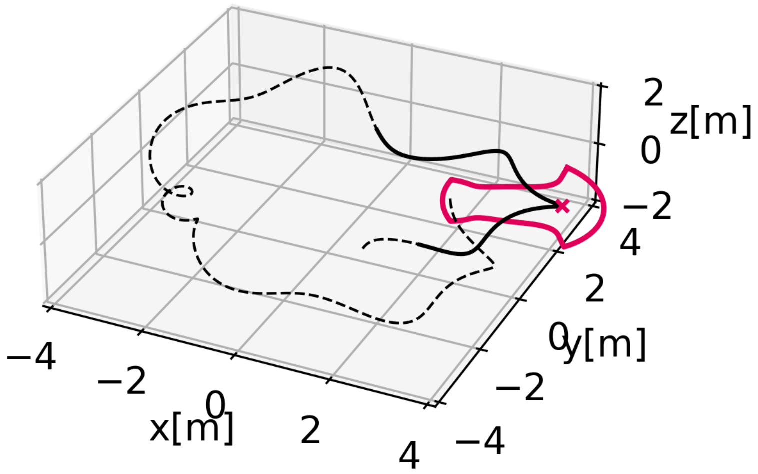

Figure 3.38: 3D model of the flux tube along which the profiles of $n_{\mathrm{C}^{3+}}$ and ionization rate from C^{2+} to C^{3+} have been investigated. The black solid line represents the range of the flux tube shown in Fig. 3.39. The red cross shows the peak of $n_{\mathrm{C}^{3+}}$ in the horizontally elongated cross-section, which corresponds to the zero points of horizontal axes in Fig. 3.39. The inner wall structure of the horizontally elongated cross-section is drawn with red line.

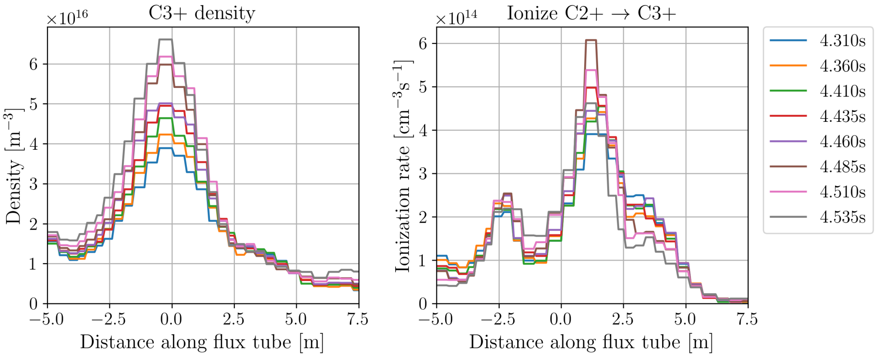

Figure 3.39: The temporal changes of profiles of $n_{\mathrm{C}^{3+}}$ and ionization rate from C^{2+} to C^{3+} along the flux tube which goes through the peak of $n_{\mathrm{C}^{3+}}$ at 4.51 s in the simulation.

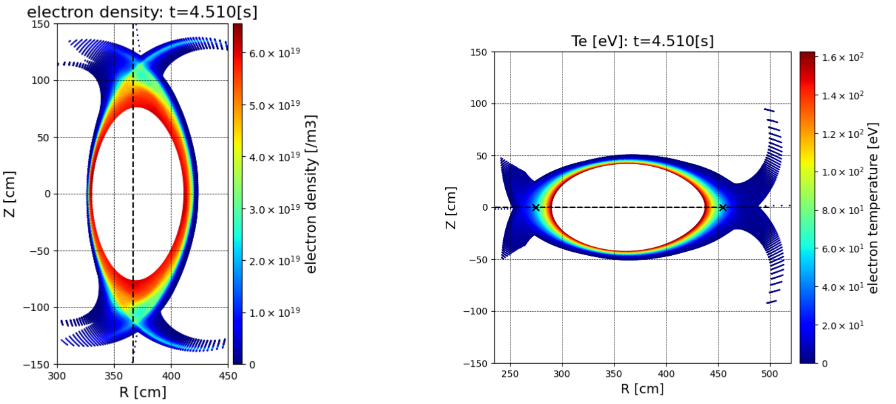

(a) n_e and line of sight of FIR measurement.

(b) T_e and line of sight of Thomson scattering measurement.

Figure 3.40: Line of sight (LoS) of (a) FIR measurement and (b) Thomson scattering measurement reproduced on EMC3-EIRENE result at 4.51 s. The X points in (b) correspond to the position of the LCFS in vacuum on the LoS.

this validation. Besides, CIV line emission measurement has been estimated by reproducing the viewing area of VUV spectroscopy measurement. The detail of the viewing area of VUV spectroscopy system is described in [87]. Figure 3.41 shows the reproduced viewing area as the region between black solid lines. As estimation of CIV measurement, CIV line emission in the viewing area has been summed up.

Figure 3.42 shows the comparison between measured value in the experiment and EMC3-EIRENE results. As shown in panels (c) and (d) in Fig. 3.42, estimated $\bar{n}_\mathrm{e}$ and $T_{\mathrm{e,edge}}$ approximately match to the measured values. It is reasonable that the estimated and measured $\bar{n}_\mathrm{e}$ values are similar since the n_e profile at each time slice is given as a input parameter to the simulation code. On the other hand, the increase of the estimated CIV line intensity by time is smaller than that of the measured value, as shown in panel (e) in Fig. 3.42. Here, the estimated CIV line intensity has been normalized to make it match with the measured value at the first time slice (4.31 s).

The collapse likelihood and the decision function value are shown in Fig. 3.42 (a) and (b), respectively. According to these graphs, the estimated values are also increasing during the time when the actual values are increasing. However, the amount of the rise in the reproduced likelihood and the decision function are smaller than these of the actual values. At the final time slice (4.51 s), the likelihood reached only 0.64. It seems that the cause of the lower likelihood than the actual one is the fact that the estimated increase in CIV line emission is less

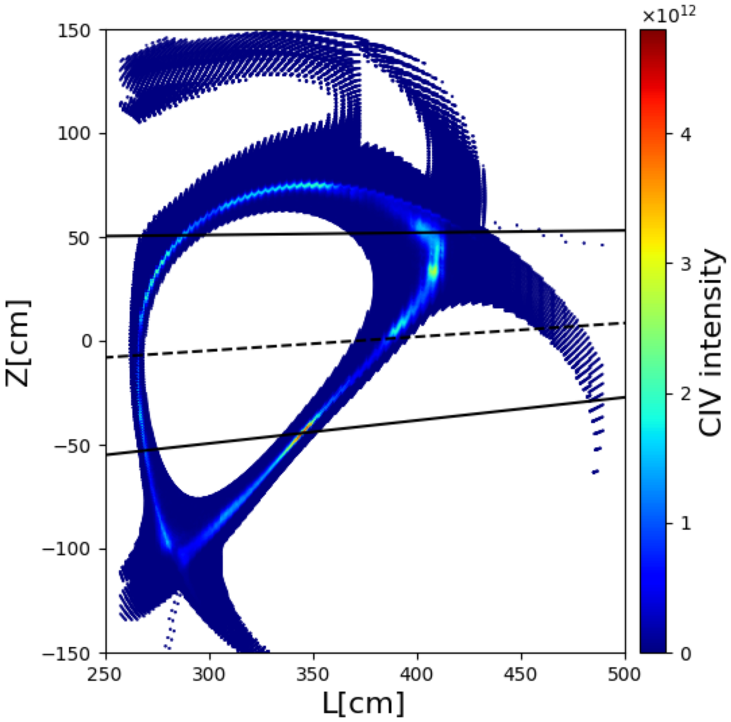

Figure 3.41: Reproduced viewing area (between black solid lines) and CIV line emission on the plane including optical axes of the VUV spectrometer.

than the measured value.

One possible reason why the increase in the measured CIV line emission is greater than the reproduced one is the existence of a non-linear event while plasma approaches the collapse. Figure 3.43 shows raw and resampled signals of CIII, CIV, OV, and OVI line emissions. The resampled signals are usually used in the present study and shown in Fig. 3.42 as “EGdata.” At around 4.5 s, impurity line emission signals increased temporally, which is different from the reproduced CIV line emission shown in Fig. 3.42 (e). While the reason for this transient change has not been specified yet, there seemed to be some non-linear event, such as a change of diffusion coefficient by turbulence, which the EMC3-EIRENE cannot simulate. This hypothesis is supported by the observation described in section 3.2.3.

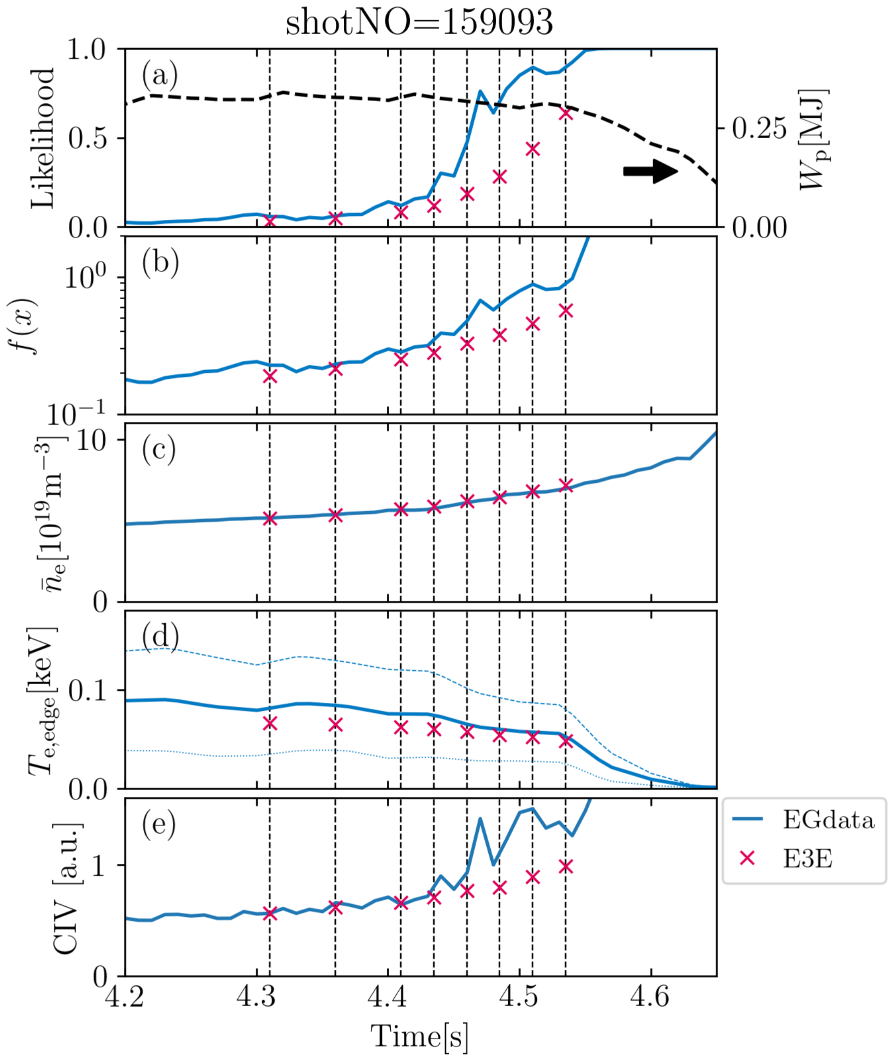

Figure 3.42: Comparison between real (measured) value (blue lines) and EMC3-EIRENE results (red crosses) of (a) collapse likelihood, (b) value of decision function, (c) $\bar{n}_\mathrm{e}$, (d) $T_\mathrm{e,edge}$, and (e) CIV. The black line in (a) represents W_p.

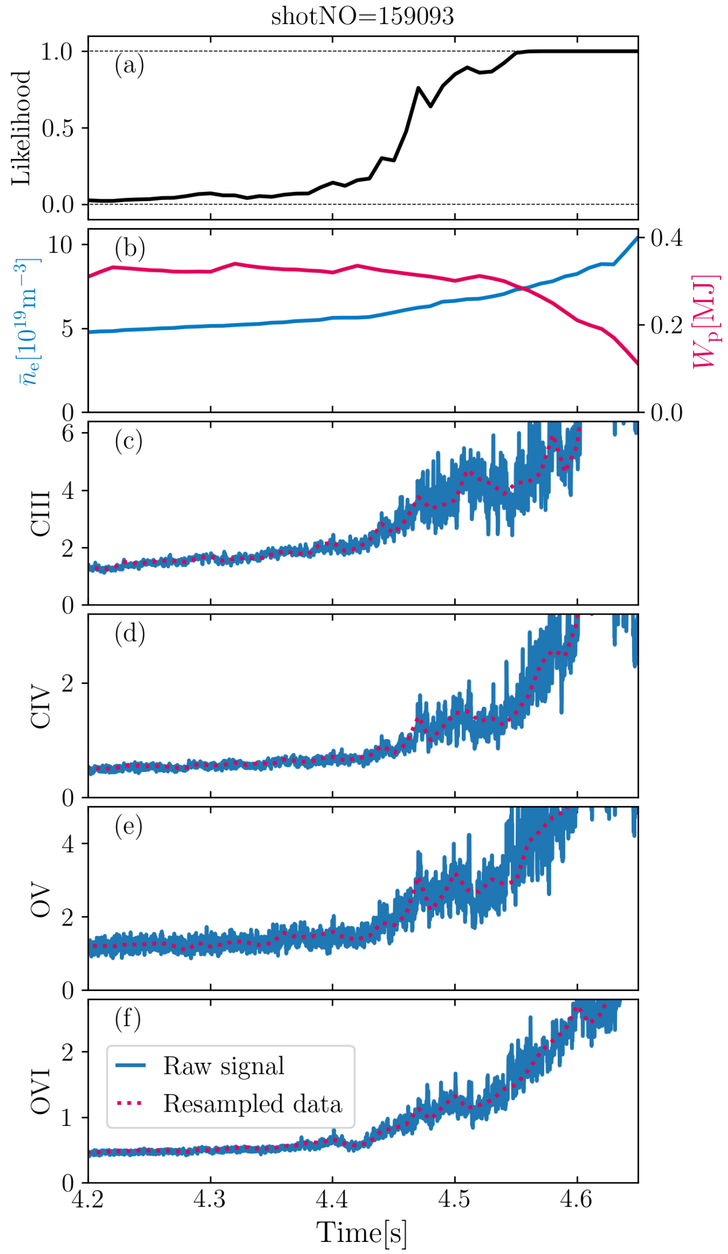

Figure 3.43: Temporal changes of (a) collapse likelihood, (b) line averaged electron density $\bar{n}_\mathrm{e}$ and stored energy W_p, (c) CIII line emission, (d) CIV line emission, (e) OV line emission, and (f) OVI line emission. Blue and red lines in panels (c)–(f) represents raw and resampled signals, respectively.

Chapter 4

Prediction and feature extraction of high-beta disruption in tokamak plasmas

4.1 Disruption prediction in JT-60U

4.1.1 High-beta experiment in JT-60U

Disruptions in high-beta plasma in JT-60U has been mainly investigated in the present research. It is known that high-beta disruption has less obvious precursors than other types of disruptions such as density-limit disruptions and vertical displacement event (VDE) disruptions [88]. The difficulty of detection of precursors is catenated with difficulties in predicting disruption and identifying beta limit.

To construct the dataset to train a machine-learning model, the experiments in which suppression of the resistive wall mode (RWM) has been attempted by driving toroidal rotation of plasma with neutral beam injection (NBI) have been considered. Here, the RWM is one of magnetohydrodynamic (MHD) instabilities which grows with a growth time corresponding to the skin time of the resistive wall. Normalized beta β_{N} (1.13) is limited by ideal kink-ballooning instability, which is a MHD instability with a low toroidal mode number n. This limit of operational beta is called "no-wall" beta limit $\beta_{\mathrm{N}}^{\text{no-wall}}$. In ideal MHD case, the kink-ballooning instability is stabilized by eddy current in a conducting wall with perfect conductivity. The operational beta limit with the ideal-conducting wall is called "ideal-wall" limit $\beta_{\mathrm{N}}^{\text{ideal-wall}}$. In the realistic devices which have conducting wall with a finite resistivity, the eddy current in the wall will be disappear and the stabilizing effect is lost. The finite resistivity of the conducting wall induces another instability, that is, the RWM. It is shown that the RWM is suppressed by plasma rotation in DIII-D [89].

In this study, 36 plasma discharges were identified as "disruptive" discharge with the criterion that plasma currents shut down with their decay times shorter than 40 ms. Here, only current quenches during the flattop phase with an I_p of 0.9 MA have been taken into account. The occurrence of current quench is defined as the time at which plasma current falls below 95% of the flattop current. The decay time is defined as the time divided by 0.6 from the occurrence of current quench to the time plasma current falls below 40% of flattop current [90]. By this criterion, 5% of available discharges in which plasma current shut down have been employed in the dataset. The discharges taken into the dataset are 75% of available discharges in which plasma current shut down. On the other hand, 61 plasma discharges in which the plasma current is controlled to be stationary at 0.9 MA, are defined as "non-disruptive" discharges.

In the present experiments, no-wall limit and ideal-wall limits are given as $\beta_\mathrm{N}^\text{no-wall} \sim 3l_\mathrm{i}$ and $\beta_\mathrm{N}^\text{ideal-wall} \sim 4l_\mathrm{i}$ by stability analysis using MARG2D [91–93]. Here, l_i is the internal inductance defined as follows:

$$l_\mathrm{i} = \frac{\langle B_\mathrm{p}^2 \rangle}{B_\mathrm{p}^2(a)}, \tag{4.1}$$

where B_p is the poloidal magnetic field, a is the minor radius, and the angular brackets signify taking a volume average. Since the l_i depends on the profile of B_p, l_i corresponds to the profile of plasma current profile. Figure 4.1 shows normalized beta β_N plotted against the internal inductance l_i for discharges in the dataset. According to Fig. 4.1 the data are disruptive discharges mainly distribute above dashed line, which corresponds to the no-wall beta limit.

The 14 plasma parameters listed in Table 4.1 have been considered in the dataset. For some of these parameters, such as β_N and q_{95} are obtained by equilibrium calculation, and the $|B_\mathrm{r}^{n=1}|$ value is the amplitude of $n = 1$ mode on magnetic fluctuation B_r. It is the Fourier-decomposed magnetic fluctuation signal B_r, which was detected by toroidally distributed saddle loops [92].

In JT-60U, it is shown that the rotation at the $q = 2$ surface can suppress the RWM [94]. Therefore, four radial profile parameters at around the $q = 2$ rational surface consist of V_t, T_i, $\rho_{q=2}/a$, and s, where q is the safety factor, are taken into account. For these parameters, the volume-averaged minor radius ρ is used as a radial index and is calculated as follows:

$$\rho = \sqrt{\frac{V(\Psi)}{2\pi^2 R}}. \tag{4.2}$$

Here, $V(\Psi)$ is plasma volume surrounded by magnetic surface Ψ and R is the major radius. Ion temperature T_i at the $q = 2$ rational surface is around 2 keV

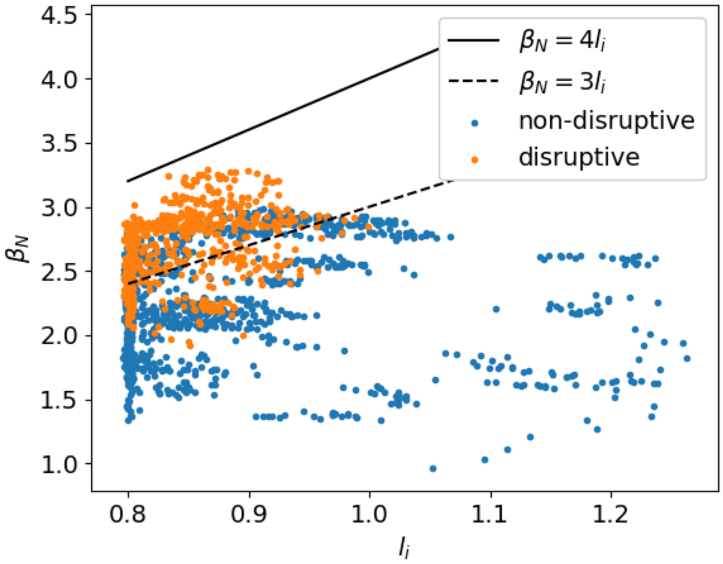

Figure 4.1: Normalized beta β_N against the internal inductance l_i in the analyzed dataset. Orange and blue dots show data points from disruptive and non-disruptive discharges, respectively. The dashed and solid lines show no-wall beta limit and ideal-wall beta limit, respectively.

Table 4.1: Plasma parameters used in the machine learning model [3]

		Range of training data	
Name of parameters	Expression	Min.	Max.
Plasma current [MA]	I_{p}	0.70	1.01
Normalized beta	β_{N}	0.58	3.29
Plasma internal inductance	l_{i}	0.80	1.26
Safety factor at 95% of poloidal flux	q_{95}	3.07	4.33
Plasma triangularity	δ	0.28	0.46
Plasma elongation	κ	1.30	1.49
Magnetic perturbation amplitude ($n = 1$) [mT]	$\lvert B_{\mathrm{r}}^{n=1}\rvert$	0.00	1.44
Ratio of electron density to the Greenwald density limit	$f_{\mathrm{GW}} = \bar{n}_{\mathrm{e}}/n_{\mathrm{GW}}$	0.31	1.66
Ratio of radiated power to total input power	$f_{\mathrm{rad}} = P_{\mathrm{rad}}/P_{\mathrm{input}}$	0	0.47
Speed of toroidal plasma rotation[$\times 10^5$m/s] *	$\lvert V_{\mathrm{t}}\rvert$	0.00	0.60
Direction of toroidal plasma rotation* **	$\exp(V_{\mathrm{t}}/\lvert V_{\mathrm{t}}\rvert)$	$1/e$	e
Ion temperature[keV] *	T_{i}	0.59	3.21
Radial location of $q = 2$ rational surface normalized by the minor radius of plasma surface a	$\rho_{q=2}/a$	0.46	0.80
Magnetic shear*	s	0.56	2.10

* For those parameters, values on rational surface where safety factor equal two, which is obtained by equilibrium calculation assuming $q = 1$ at plasma center, are used.

** For taking logarithms of this parameter in training process, exponential of the value has been taken.

and is distributed from 0.59 keV to 3.21 keV. In order to take logarithms of the velocity of toroidal rotation V_t, V_t has been separated into two parameters, that is, the speed of rotation $|V_\mathrm{t}|$ and the direction of rotation $V_\mathrm{t}/|V_\mathrm{t}|$. Note that the profile of q is obtained by equilibrium calculation assuming $q = 1$ at plasma center in this process.

Although there are some data with a high (over 1) f_GW value or high (over 1 mT) $|B_\mathrm{r}^{n=1}|$ value, those data will be ignored in the training of machine learning models and these discharges will be judged as extraordinary discharges in the evaluation.

4.1.2 Feature extraction of disruption in JT-60U

Evaluation of predictive performance

In the ES to extract feature parameters of disruption prediction in JT-60U, the combinations of parameters have been compared each other in not F1-score but prediction performance. A disruption predictor is required to predict disruptions faster and more accurately and not to issue an alarm accidentally if it is not disruption. For measuring the prediction performance, the prediction success rate (PSR) and the false alarm rate (FAR) have been used in this chapter, defined as follows:

$$\begin{aligned}
&\textit{Prediction Success Rate (PSR)}\\
&\qquad = \frac{\textit{Number of shots correctly judged as disruptive}}{\textit{Total number of disruptive shots}}, && (4.3)\\
&\textit{False Alarm Rate (FAR)}\\
&\qquad = \frac{\textit{Number of shots incorrectly judged as disruptive}}{\textit{Total number of non-disruptive shots}}. && (4.4)
\end{aligned}$$

PSR is the ratio of the number of shots correctly judged as disruptive by the specific time of interest to the total number of disruptive shots. On the other hand, FAR is the ratio of the number of shots incorrectly judged as disruptive by the specific time of interest to the total number of non-disruptive shots. These measures were used in previous studies to predict high-β disruptions using artificial neural networks [26, 30].

When the predictor shows the ideal performance, $PSR = 100\%$ and $FAR = 0\%$. Therefore, the distance from the ideal performance is defined as follows:

$$\textit{Distance} \equiv \sqrt{(100 - \textit{PSR})^2 + \textit{FAR}^2}. \qquad (4.5)$$

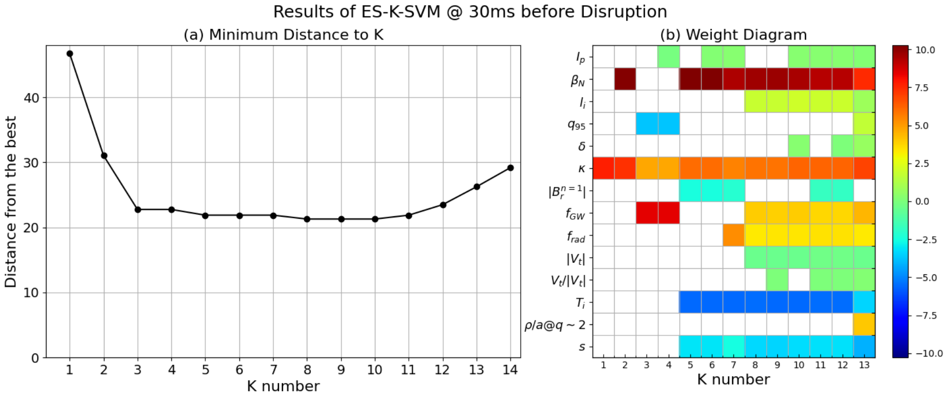

Figure 4.2: The summary of ES-K-SVM. The left graph shows the minimum distance from the ideal performance among combinations of K parameters. The right diagram shows the combination that gives the minimum distance from the ideal performance among combinations of K parameters, which correspond to the left graph. The color bar corresponds to the weight w' in eq. 2.12.

Result of feature extraction of disruption in JT-60U

Figure 4.2 shows the summary of the result of ES-K using SVM (ES-K-SVM). Here, the prediction performances have been compared at 30 ms before the reference time. The left graph of Fig. 4.2 shows the minimum distance from the ideal performance among combinations of K parameters. According to the graph, the distance from the ideal performance almost saturated at around $K = 4$, and it becomes worse using 11 or more parameters. The right diagram shows the combination that gives the minimum distance from the ideal performance among combinations of K parameters, which correspond to the left graph. Each column corresponds to each combination and the colored parameters mean to be included in the combination. The color bar corresponds to the weight w' in (2.12).

Figure 4.3 (a) is referred to as a two-dimensional (2D) density of state (2D-DoS) diagram, which is a 2D histogram with PSR as the vertical axis and FAR as the horizontal axis. The left top corner corresponds to the ideal performance ($PSR = 100\%$ and $FAR = 0\%$). The color of each square corresponds to the number of combinations within the square. Figure 4.3 (b) shows the parameters included in the top 20 combinations in Fig. 4.3 (a) and is referred to as a weight diagram. The color bar corresponds to the weight w' in (2.12).

According to Fig. 4.3, a combination of four parameters, that is, β_N, κ, T_i, and s, is dominant in the in the top 10 combinations. This means these parameters are the key parameters to predict disruption and it is implied that

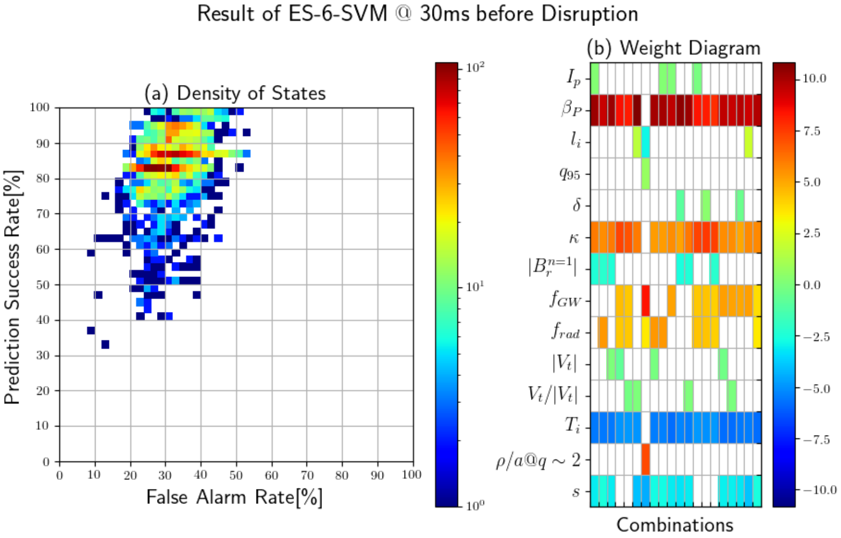

Figure 4.3: (a) 2D-DoS diagram and (b) corresponding weight diagram of ES-6-SVM at 30 ms before disruption occurs [3].

these parameters could characterize the condition of disruption. Using those four parameters, the equation of decision boundary between disruptive and non-disruptive classes is obtained as $f_{\text{exp}}(\boldsymbol{x}) = 1$, where f_{exp} is as follows:

$$f_{\text{exp}} = \exp(-19.1)\ \beta_{\text{N}}^{6.32} \kappa^{39.6} T_{\text{i}}^{-2.48} s^{-2.43}. \tag{4.6}$$

4.1.3 Disruption likelihood

Using these four extracted parameters, the characteristics of high-beta disruption in JT-60U has been discussed in terms of disruption likelihood. This likelihood is different from the "disruptivity", which was discussed in previous studies about the operational limit against disruptions [45, 46].

The calculation procedure of disruption likelihood is as same as that of collapse likelihood, described in section 3.1.3. Figure 4.4, the distribution of values of the decision function (4.6) in the dataset is shown in the bottom panel. Here, the value of the decision function corresponds to the distance from the decision boundary between the disruptive and non-disruptive regions. In the upper panel of Fig. 4.4, the percentage of disruptive data in each region of bars is shown with its fitted curve by a sigmoid function. The approximate function is expressed as follows:

$$y_{\text{fit}} = \frac{1}{1 + \exp\left\{-4.02\left(\log_{10} f_{\text{exp}}(\boldsymbol{x}) + 0.1319\right)\right\}}. \tag{4.7}$$

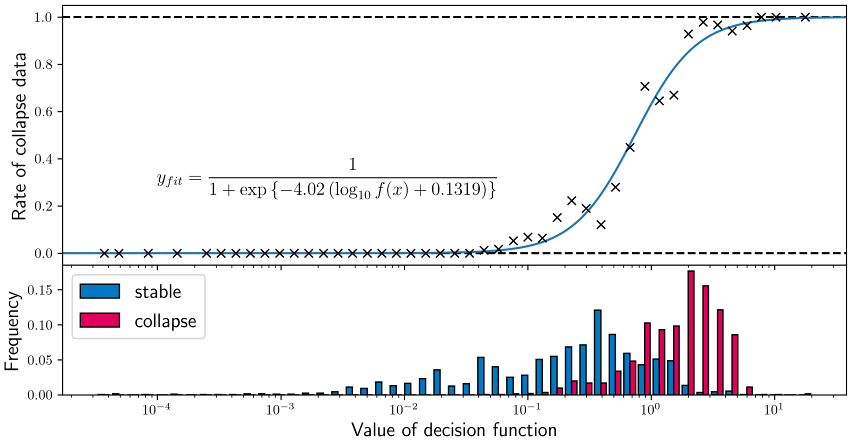

Figure 4.4: (lower) The distribution of values of the decision function shown in (4.6) when each data in the dataset is input and (upper) the percentage of disruptive data in each region of bars. The curve in the upper figure is a fitted curve of the percentage of disruptive data. The function being expressed is also shown in the figure [3].

This likelihood is the expansion of the binary classifier to the predictor model with continuous value expression. The identified expression of likelihood quantifies the proximity to disruption, in other words, the risk of disruption. The likelihood expressed by measurable parameters is prerequisite for development of the control system to avoid disruption by means of multiple actuators [95].

In Fig. 4.5, the likelihood is expressed as a color contour on the plane of β_{N} and the term of other extracted parameters, that is, κ, T_{i}, and s along with (2.2). The likelihood shows that the higher ion temperature and magnetic shear can extend the β_{N} region with low disruption likelihood. Although this seems to go against the knowledge that the high elongation raises β_{N}, it should be pointed out that this trend means that lower elongation could bring a safer high β_{N} discharge but not that lower elongation leads to higher β_{N}.

Figure 4.6 shows the typical discharge with disruption in JT-60U and the disruption likelihood approaches unity before the occurrence of disruption. The data points correspond to the points calculated for the dataset.

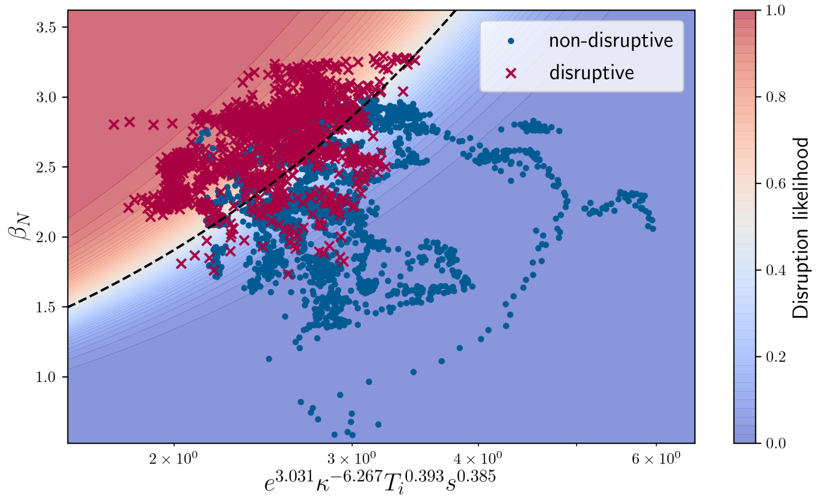

Figure 4.5: The contour plot of the likelihood of disruption against β_{N} and the terms of other extracted parameters. The red crosses and blue dots show data points from disruptive and non-disruptive discharges, respectively. Note the e in the label of vertical axis is Napier's constant [3].

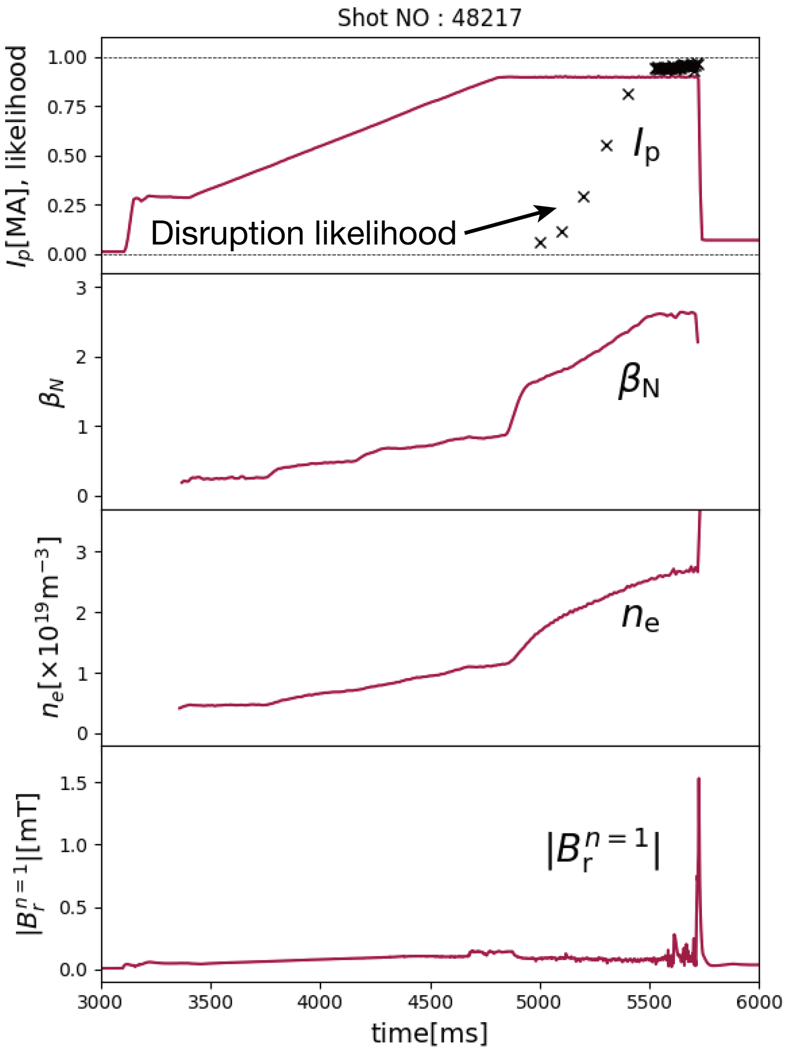

Figure 4.6: Typical discharge with disruption in the JT-60U plasma experiment targeted in this research. The black crosses in the top panel shows the disruption likelihood, which is estimated within 200 ms before the current quench [3].

4.2 Comparison of extracted features of disruptions in JT-60U and DIII-D

4.2.1 Feature extraction of disruption in DIII-D

High-beta disruptions in DIII-D

In the present research, the features of high-beta disruptions have been compared between JT-60U and DIII-D. The purpose of cross-machine comparison of feature extraction is to examine whether the extracted feature from a device is device-specific or universal.

DIII-D is a tokamak device in San Diego, US, which is smaller than JT-60U. The major and minor radii for DIII-D are 1.67 m and 0.67 m, respectively, while they are 3.4 m and 1.1 m, respectively, for JT-60U [96, 97].

From DIII-D database, high-beta disruptions, in which maximum β_{N} is larger than three times l_{i}, has been selected to construct a dataset. For all shots, the data were sampled every 25 ms, starting from 100 ms after the discharge starts. In disruptive shots, additional sampling with interval of 2 ms for the 100 ms before the disruption. The parameters used in the dataset have followed the case of JT-60U (shown in Table 4.1), while $\rho_{q=2}/a$ and s were omitted because of missing data.

Result of feature extraction

In the ES using DIII-D dataset, the combinations of parameters have been compared in F1-score. Figure 4.7 shows the summary of the result of ES-K-SVM using DIII-D dataset. According to the graph, the F1-score exceeds that with all parameters and almost saturated at $K = 5$. Around $K = 5$, some parameters are included in common in the top combination for each K, that is, β_{N}, q_{95}, $|V_{\mathrm{t}}|$, and T_{i}.

Figure 4.8 shows the result of ES-6, which is ES-K with $K = 6$. The blue bars in the left diagram show the distributions of F1-score using five parameters. Among most of the top combinations of ES-6 results, β_{N}, q_{95}, $|V_{\mathrm{t}}|$, and T_{i} are included in common. In addition, the red bars in the left diagram show the combinations including these four parameters and these combination shows the better F1-score than other combinations. Therefore, these four parameters are relevant to the prediction of radiative collapse as the key parameters. The equation of decision boundary between disruptive and non-disruptive classes is obtained as $f_{\mathrm{exp}}(\boldsymbol{x}) = 1$ with these four parameters, where f_{exp} is as follows:

$$f_{\mathrm{exp}} = \exp\left(-3.47\right)\, \beta_{\mathrm{N}}^{-1.40} q_{95}^{-3.01} T_{\mathrm{i}}^{1.53} |V_{\mathrm{t}}|^{-0.862}. \tag{4.8}$$

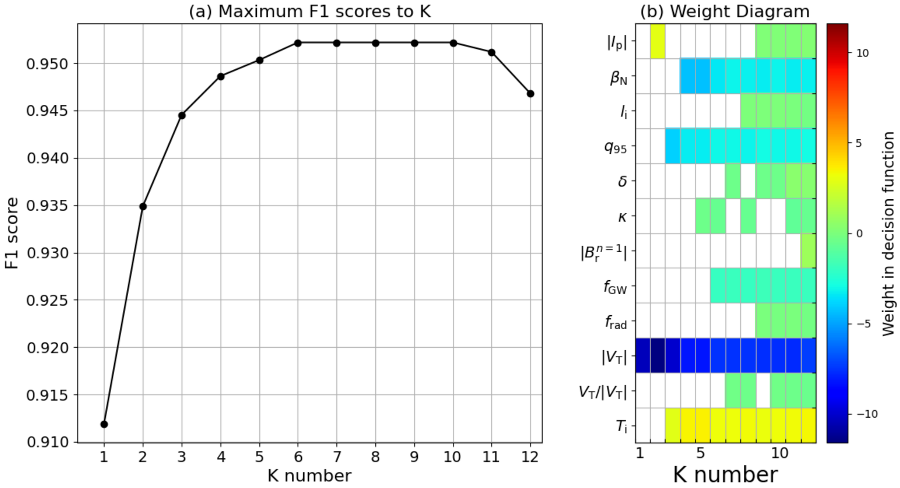

Figure 4.7: The result summary of ES. The left graph shows the best F1-scores for each K. The right diagram shows the parameters included in the each combinations correspond to the left diagram. The color bar corresponds to the weight w' in eq. 2.12.

In the previous study in DIII-D, the disruption prediction using random forests (DPRF) was developed and it showed a F1-score of 0.87 with a validation dataset [39]. In this study, normalized perturbed radial field of non-rotating modes, safety factor at the 95% flux surface, and Greenwald density fraction were selected as the most contributing parameters. Although the training dataset used to develop DPRF was broader than that in the present study, the extracted feature is totally different and the F1-score achieved in the present study is better than that of DPRF. This result suggests that it is possible to predict disruptions more accurately by using feature parameters particular to the causes of disruptions.

4.2.2 Comparison of extracted features between JT-60U and DIII-D

Comparing the result of ES and decision functions shown in (4.6) and (4.8), there are two major difference between extracted features of high-β disruptions in JT-60U and DIII-D.

The first one is the sign of the weight of β_N and T_i. In JT-60U case, the decision function (4.6) can be interpreted as the higher β_N and the lower T_i lead to disruption. On the other hand, the signs of weights of β_N and T_i in the

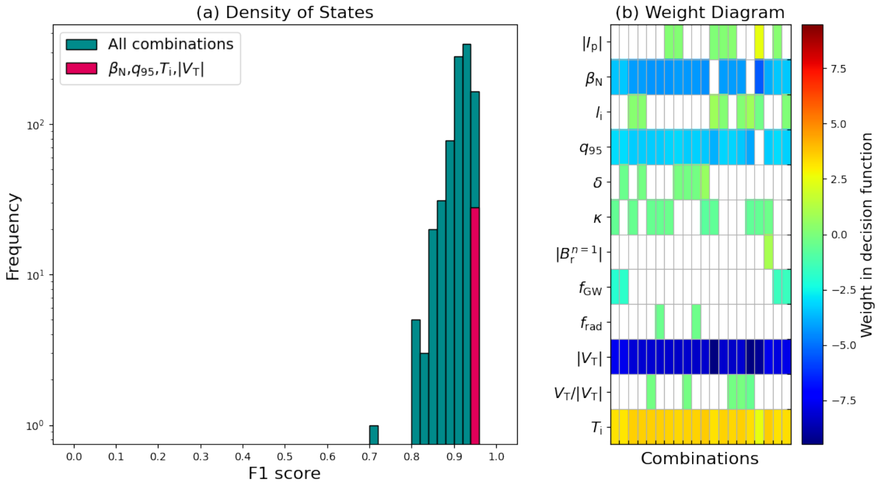

Figure 4.8: The result of ES when $K = 6$. The blue and red bars in the left diagram show the distributions of F1-score with five parameters and that with the combinations including β_N, q_{95}, $|V_t|$, and T_i, respectively. The right diagram shows the parameters included in th top 20 combinations in the F1-score. The color bar corresponds to the weight w' in eq. 2.12.

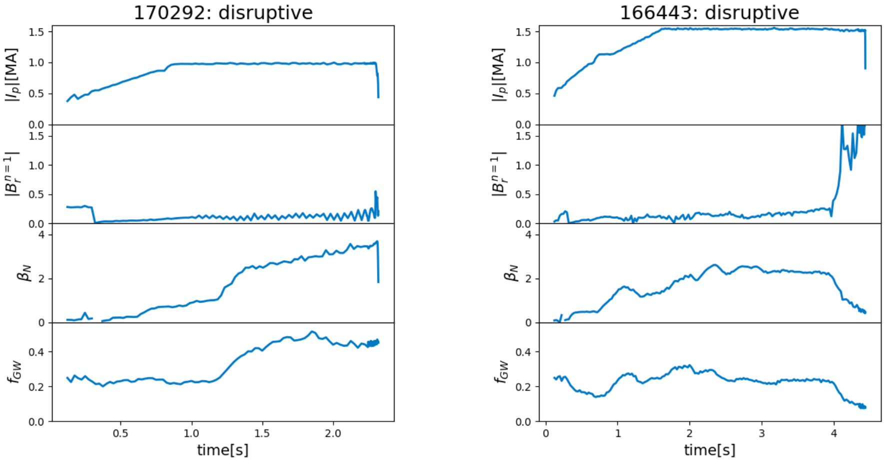

(a) Disruption from high-β_{N} (b) Disruption with early β_{N} decay

Figure 4.9: Waveforms of disruptions in DIII-D.

decision function of DIII-D case (4.8) are opposite to those in (4.6). Especially, the negative weight of β_{N} seems not reasonable with physical knowledge.

One possible reason why this difference occurred is that there may be more than one cause of disruptions in the DIII-D dataset. Figure 4.9 shows two disruptive discharges in DIII-D included in the dataset. Figure 4.9 (a) shows a disruption from high-β state, which is mainly considered in JT-60U case. On the other hand, in the disruption shown in Fig. 4.9 (b) , a decay of β_{N} (thermal collapse) and increase of $|B_{\mathrm{r}}^{n=1}|$ occurred in advance of collapse of I_{p}. It is necessary to consider whether these disruptions have the same cause or not to explain the difference between JT-60U and DIII-D results.

The second big difference is that the rotation velocity $|V_{\mathrm{t}}|$ is not included in feature parameters in JT-60U case while $|V_{\mathrm{t}}|$ has been extracted as one of key parameters in DIII-D case.

Since the dataset used in JT-60U case consists of high-β experiments in which suppression of RWM has been attempted by plasma rotation, it was expected that $|V_{\mathrm{t}}|$ is extracted as a key parameter. In these experiments in JT-60U, those local values at the $q = 2$ rational surface have been used since the mode structure of precursor oscillation is localized at the $q = 2$ rational surface. This mode is the energetic particle driven wall mode (EWM), which is thought to be one cause of RWM and lead to disruption in these experiments [92]. Here, the position of the $q = 2$ rational surface is provisionally evaluated by the equilibrium analysis assuming $q(\rho = 0) = 1$ while direct measurement of the poloidal magnetic field by the motional Stark effect (MSE) shows that $q(\rho = 0)$ is larger than unity, as shown in Fig. 4.10. Therefore, the real location of the $q = 2$ surface would be located inside this provisional estimate. However, it is pointed out that the profiles of V_{t} and T_{i} are peaked and s increases monotonically with the minor radius and local values used in the present analysis change gradually in space. Since the ambiguity of the location of $q = 2$ surface and accompanied errors of local values are systematically in the same direction, even the present analysis would not lead to qualitative misunderstanding. In DIII-D case, q profile by MSE measurement has been used to find out $q = 2$ position. For further discussions, precise identification of the location of the $q = 2$ surface is required.

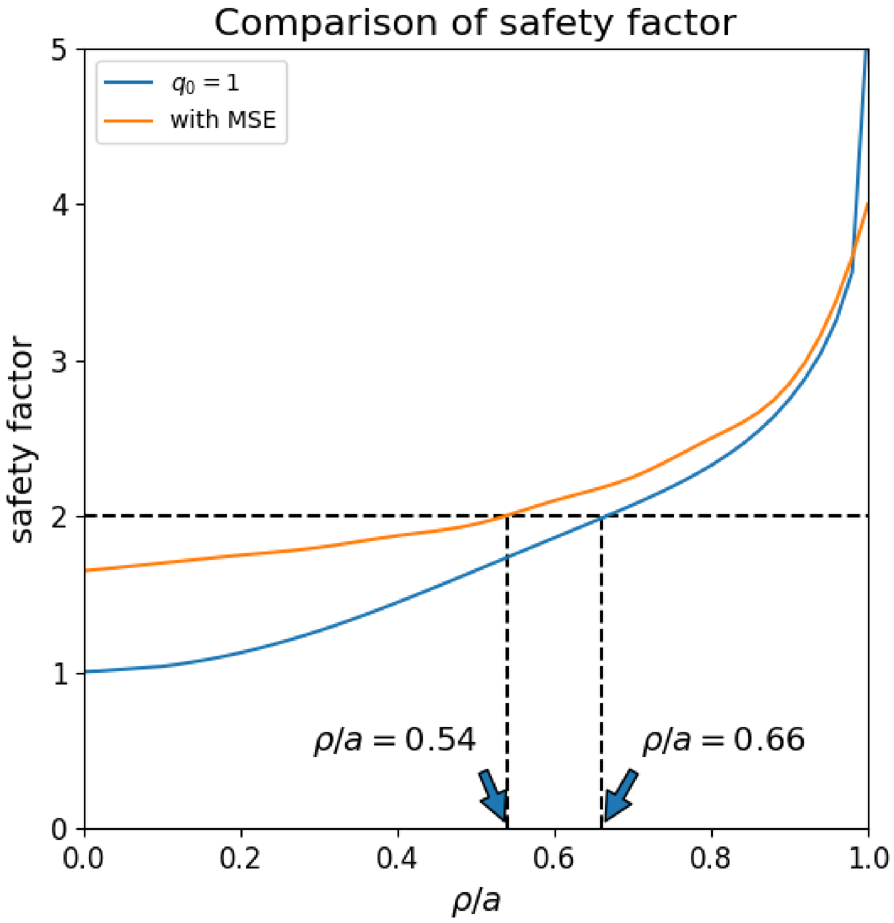

Figure 4.10: Profile of safety factor q obtained by (blue) equilibrium calculation assuming $q = 1$ at plasma center and (orange) direct measurement of the poloidal magnetic field by the motional Stark effect.

Chapter 5

Conclusion

To realize a fusion reactor, it is necessary to avoid the occurrence of abrupt termination events such as radiative collapses in stellarator-heliotron plasmas and disruptions in tokamak plasmas. Since the mechanism of the collapses has not been completely elucidated yet, data-driven predictions of the occurrence of collapses have been studied based on experiment data using machine learning techniques.

In the present study, prediction and feature extraction of radiative collapses in LHD and high-beta disruptions in JT-60U are discussed to show that the data-driven approach can be applied to a variety of abrupt terminations phenomena. The prediction has been treated as a classification problem that divides data into two classes, that is, stable or approaching the termination. To improve the prediction performance and facilitate the physical discussion of the prediction results, exhaustive search (ES) , which is one of the sparse modeling techniques, has been employed. Moreover, the likelihood of abrupt terminations has been quantitatively evaluated using the feature parameters, which makes it easy and flexible to apply the binary classifier model to prediction and control.

In chapter 2, machine learning techniques that are used in the present study are explained. A linear support vector machine has been trained with logarithmic data to express the boundary between two classes as a exponential-formed equation. While the number of combinations that are compared in ES exponentially increases when the number of parameters increase, a extension of ES named “ES-K” has been employed to avoid this combination explosion risk.

Chapter 3 describes prediction and feature extraction study of radiative collapses in high-density experiments in LHD. A predictor model has been developed based on feature parameters extracted by ES, that are, $\bar{n}_\mathrm{e}$, CIV, OV, and $T_\mathrm{e,edge}$, and the collapse likelihood has been quantitatively evaluated using these feature parameters. The predictor which calculates the likelihood in real time has been used to avoid radiative collapse in LHD experiments. Changes in plasma leading to collapse have been discussed and it has been suggested that the growth of the fluctuation (or turbulence) in the edge region plays an important role in the mechanism of the occurrence of the radiative collapse. It has been also discussed that the behaviors of plasma and carbon impurities in the edge region when the plasma approaching the collapse using EMC3-EIRENE code. The existence of a non-linear phenomenon, which the EMC3-EIRENE cannot simulate, when plasma approaches collapse has been suggested by comparing the simulation results and the experimental results.

In chapter 4, prediction and feature extraction of disruptions in high-beta experiments in JT-60U has been described. By ES, feature parameters of high-beta disruption in JT-60U has been extracted and the disruption likelihood has been quantified. The extracted features have been compared withe those of high-beta disruptions in DIII-D tokamak. Because of the ambiguity of the location of $q = 2$ surface, precise identification of q profile is required to discuss the physical linkage between the occurrence of disruptions and the local parameters such as $|V_{\mathrm{t}}|$ in detail.

This thesis has shown that the data-driven approach is useful to predict a variety of abrupt termination phenomena, such as radiative collapses and disruptions, for avoidance and mitigation. It has been also shown that the sparse expressions extracted from data is helpful to discuss physical mechanisms of these abrupt termination phenomena. More investigation using data-driven approaches, especially feature extraction techniques, will reveal the common physical background which underlies the abrupt termination events. For this purpose, comparison of extracted features over various fusion devices will be important.

Appendix A

Extrapolability of radiative collapse prediction

High extrapolability is one of the desired properties of the collapse predictor. To evaluate the extrapolability of the collapse predictor developed in chapter 3, the ES-SVM has been conducted again with the low density data, in which line-averaged electron density limited to $n_\mathrm{e} < 6.0 \times 10^{19}\,\mathrm{m}^{-3}$. Here, the limited-data is equivalent to 80% of the dataset described in section 3.1.

As a result of ES-SVM, four parameters have been selected as feature parameters, that is, $\bar{n}_\mathrm{e}$, $P_\mathrm{rad}/P_\mathrm{abs}$, Δ_sh, and $T_\mathrm{e,edge}$, which is different from the result described in section 3.1. Table A.1 shows the performance of SVMs trained with low-density data consisting of two combinations of parameters, evaluated with low-density($n_\mathrm{e} < 6.0 \times 10^{19}\,\mathrm{m}^{-3}$) and high-density ($n_\mathrm{e} > 6.0 \times 10^{19}\,\mathrm{m}^{-3}$) data, respectively. The first combination is the combination which is extracted by ES-SVM with low-density data, that is, $\bar{n}_\mathrm{e}$, $P_\mathrm{rad}/P_\mathrm{abs}$, Δ_sh, and $T_\mathrm{e,edge}$. The second one is the parameters selected based on the whole dataset, that is, $\bar{n}_\mathrm{e}$, $P_\mathrm{rad}/P_\mathrm{abs}$, Δ_sh, and $T_\mathrm{e,edge}$, described in section 3.1.

Trained with the first combination, the SVM shows 0.967 accuracy and 0.844

Table A.1: Results of classification by SVM trained with $n_\mathrm{e} < 6.0 \times 10^{19}\,\mathrm{m}^{-3}$ data.

Parameters	Data range	F1-score	Accuracy
$\bar{n}_\mathrm{e}$, $P_\mathrm{rad}/P_\mathrm{abs}$, Δ_sh, and $T_\mathrm{e,edge}$	$n_\mathrm{e} < 6.0 \times 10^{19}\,\mathrm{m}^{-3}$	0.844	0.967
	$n_\mathrm{e} > 6.0 \times 10^{19}\,\mathrm{m}^{-3}$	0.824	0.811
$\bar{n}_\mathrm{e}$, CIV, OV, and $T_\mathrm{e,edge}$	$n_\mathrm{e} < 6.0 \times 10^{19}\,\mathrm{m}^{-3}$	0.802	0.963
	$n_\mathrm{e} > 6.0 \times 10^{19}\,\mathrm{m}^{-3}$	0.860	0.858

F1-score against the low-density data. Against the high-density data, both accuracy and F1-score becomes worse. This fact implies the feature parameters extracted based on low-density data have low extrapolability.

Note that the decision boundary using the second combination does not match with (3.1). Nevertheless, the SVM trained with the second combination shows a higher F1-score against the high-density data than that against the low-density data. The accuracy against the high-density data is worse than against the low-density data, while it is better than that of SVM trained with the first combination. This result suggests that this combination is reflecting the feature of radiative collapse in not only low-density but also high-density plasma.

In consequence, the extrapolability of the ES-SVM technique is not so high, therefore it is desirable to extract features from wide range of data.

Bibliography

[1] Yokoyama T, Yamada H, Masuzaki S, Miyazawa J, Mukai K, Peterson B J, Tamura N, Sakamoto R, Motojima G, Ida K, Goto M, Oishi T, Kawamura G, Kobayashi M and LHD Experiment Group 2021 *Plasma and Fusion Research* **16** 2402010

[2] Yokoyama T, Yamada H, Masuzaki S, Miyazawa J, Mukai K, Peterson B J, Tamura N, Sakamoto R, Motojima G, Ida K, Goto M, Oishi T and LHD experiment Group 2020 *Journal of Fusion Energy* **39** 500–511

[3] Yokoyama T, Yamada H, Isayama A, Hiwatari R, Ide S, Matsunaga G, Miyoshi Y, Oyama N, Imagawa N, Igarashi Y, Okada M and Ogawa Y 2021 *Plasma and Fusion Research* **16** 1402073

[4] Yokoyama T, Miyoshi Y, Hiwatari R, Isayama A, Matsunaga G, Oyama N, Igarashi Y, Okada M and Ogawa Y 2019 *Fusion Engineering and Design* **140** 67–80

[5] Post D, Jensen R, Tarter C, Grasberger W and Lokke W 1977 *Atomic Data and Nuclear Data Tables* **20** 397–439

[6] Lawson J D 1957 *Proceedings of the Physical Society. Section B* **70** 6–10

[7] Whesson J 2004 *Tokamaks — Third Edition* (OXFORD UNIVERSITY PRESS)

[8] Iiyoshi A, Komori A, Ejiri A, Emoto M, Funaba H, Goto M, Ida K, Idei H, Inagaki S, Kado S, Kaneko O, Kawahata K, Kobuchi T, Kubo S, Kumazawa R, Masuzaki S, Minami T, Miyazawa J, Morisaki T, Morita S, Murakami S, Muto S, Mutoh T, Nagayama Y, Nakamura Y, Nakanishi H, Narihara K, Nishimura K, Noda N, Ohdachi S, Ohyabu N, Oka Y, Osakabe M, Ozaki T, Peterson B, Sagara A, Sakakibara S, Sakamoto R, Sasao H, Sasao M, Sato K, Sato M, Seki T, Shimozuma T, Shoji M, Suzuki H, Takeiri Y, Tanaka K, Toi K, Tokuzawa T, Tsumori K, Tsuzuki K, Watanabe K, Watari T, Yamada

H, Yamada I, Yamaguchi S, Yokoyama M, Akiyama R, Chikaraishi H, Haba K, Hamaguchi S, Iima M, Imagawa S, Inoue N, Iwamoto K, Kitagawa S, Kodaira J, Kubota Y, Maekawa R, Mito T, Nagasaka T, Nishimura A, Takahashi C, Takahata K, Takita Y, Tamura H, Tsuzuki T, Yamada S, Yamauchi K, Yanagi N, Yonezu H, Hamada Y, Matsuoka K, Murai K, Ohkubo K, Ohtake I, Okamoto M, Satoh S, Satow T, Sudo S, Tanahashi S, Yamazaki K, Fujiwara M and Motojima O 1999 *Nuclear Fusion* **39** 1245–1256

[9] Boozer A H 2012 *Physics of Plasmas* **19** 058101

[10] Yoshino R, Kondoh T, Neyatani Y, Itami K, Kawano Y and Isei N 1997 *Plasma Physics and Controlled Fusion* **39** 313–332

[11] Hender T, Wesley J, Bialek J, Bondeson A, Boozer A, Buttery R, Garofalo A, Goodman T, Granetz R, Gribov Y, Gruber O, Gryaznevich M, Giruzzi G, Günter S, Hayashi N, Helander P, Hegna C, Howell D, Humphreys D, Huysmans G, Hyatt A, Isayama A, Jardin S, Kawano Y, Kellman A, Kessel C, Koslowski H, Haye R L, Lazzaro E, Liu Y, Lukash V, Manickam J, Medvedev S, Mertens V, Mirnov S, Nakamura Y, Navratil G, Okabayashi M, Ozeki T, Paccagnella R, Pautasso G, Porcelli F, Pustovitov V, Riccardo V, Sato M, Sauter O, Schaffer M, Shimada M, Sonato P, Strait E, Sugihara M, Takechi M, Turnbull A, Westerhof E, Whyte D, Yoshino R, Zohm H and the ITPA MHD, Disruption and Magnet Group 2007 *Nuclear Fusion* **47** S128–S202

[12] Gruber O, Lackner K, Pautasso G, Seidel U and Streibl B 1993 *Plasma Physics and Controlled Fusion* **35** B191–B204

[13] Wesson J A, Gill R D, Hugon M, Schüller F C, Snipes J A, Ward D J, Bartlett D V, Campbell D J, Duperrex P A, Edwards A W, Granetz R S, Gottardi N A O, Hender T C, Lazzaro E, Lomas P J, Cardozo N L, Mast K F, Nave M F F, Salmon N A, Smeulders P, Thomas P R, Tubbing B J D, Turner M F and Weller A 1989 *Nuclear Fusion* **29** 641–666

[14] Greenwald M 2002 *Plasma Physics and Controlled Fusion* **44** R27–R53

[15] Troyon F, Gruber R, Saurenmann H, Semenzato S and Succi S 1984 *Plasma Physics and Controlled Fusion* **26** 209–215

[16] Sudo S, Takeiri Y, Zushi H, Sano F, Itoh K, Kondo K and Iiyoshi A 1990 *Nuclear Fusion* **30** 11–21

[17] Peterson B J, Miyazawa J, Nishimura K, Masuzaki S, Nagayama Y, Ohyabu N, Yamada H, Yamazaki K, Kato T, Murakami I, Ashikawa N, Xu Y, Kostrioukov A Y, Liu Y, Sakamoto R, Goto M, Narihara K, Osakabe M, Tanaka K, Tokuzawa T, Shoji M, Funaba H, Morita S, Morisaki T, Kaneko O, Kawahata K, Komori A, Sudo S, Motojima O and the LHD Experiment Group 2006 *Plasma and Fusion Research* **1** 045–045

[18] Miyazawa J, Sakamoto R, Masuzaki S, Peterson B, Tamura N, Goto M, Yamada I, Narihara K, Tanaka K, Tokuzawa T, Shoji M, Kobayashi M, Arimoto H, Kondo K, Murakami S, Funaba H, Sakakibara S, Osakabe M, Morita S, Nagayama Y, Ohyabu N, Yamada H, Komori A, Motojima O and the LHD Experiment Group 2008 *Nuclear Fusion* **48** 015003

[19] Itoh K, Itoh S I and Giannone L 2001 *Journal of the Physical Society of Japan* **70** 3274–3284

[20] Zanca P, Sattin F, Escande D and JET Contributors 2019 *Nuclear Fusion* **59** 126011

[21] Itoh K and Itoh S I 1988 *Journal of the Physical Society of Japan* **57** 1269–1272

[22] Hirsch M, Baldzuhn J, Beidler C, Brakel R, Burhenn R, Dinklage A, Ehmler H, Endler M, Erckmann V, Feng Y, Geiger J, Giannone L, Grieger G, Grigull P, Hartfuß H J, Hartmann D, Jaenicke R, König R, Laqua H P, Maaßberg H, McCormick K, Sardei F, Speth E, Stroth U, Wagner F, Weller A, Werner A, Wobig H and Zoletnik S 2008 *Plasma Physics and Controlled Fusion* **50** 053001

[23] Giannone L, Brakel R, Burhenn R, Ehmler H, Feng Y, Grigull P, McCormick K, Wagner F, Baldzuhn J, Igitkhanov Y, Knauer J, Nishimura K, Pasch E, Peterson B J, Ramasubramanian N, Rust N, Weller A, Werner A and the W7-AS Team 2003 *Plasma Physics and Controlled Fusion* **45** 1713–1731

[24] Peterson B J, Xu Y, Sudo S, Tokuzawa T, Tanaka K, Osakabe M, Morita S, Goto M, Sakakibara S, Miyazawa J, Kawahata K, Ohyabu N, Yamada H, Kaneko O and Komori A 2001 *Physics of Plasmas* **8** 3861–3864

[25] Ozeki T, Clement S and Nakajima N 2014 *Fusion Engineering and Design* **89** 529–531

[26] Wroblewski D, Jahns G and Leuer J 1997 *Nuclear Fusion* **37** 725–741

[27] Pautasso G, Tichmann C, Egorov S, Zehetbauer T, Gruber O, Maraschek M, Mast K F, Mertens V, Perchermeier I, Raupp G, Treutterer W, Windsor C and Team A U 2002 *Nuclear Fusion* **42** 100–108

[28] Cannas B, Fanni A, Marongiu E and Sonato P 2003 *Nuclear Fusion* **44** 68–76

[29] Yoshino R 2003 *Nuclear Fusion* **43** 1771–1786

[30] Yoshino R 2005 *Nuclear Fusion* **45** 1232

[31] Rattá G, Vega J, Murari A, Vagliasindi G, Johnson M, de Vries P and JET EFDA Contributors 2010 *Nuclear Fusion* **50** 025005

[32] Vega J, Dormido-Canto S, López J M, Murari A, Ramírez J M, Moreno R, Ruiz M, Alves D, Felton R and JET-EFDA Contributors 2013 *Fusion Engineering and Design* **88** 1228–1231

[33] Rattá G, Vega J, Murari A and JET-EFDA Contributors 2012 *fusion Engineering and Design* **87** 1670–1678

[34] Moreno R, Vega J, Dormido-Canto S, Pereira A, Murari A and JET Contributors 2016 *Fusion Science and Technology* **69** 485–494

[35] Murari A, Lungaroni M, Peluso E, Gaudio P, Vega J, Dormido-Canto S, Baruzzo M, Gelfusa M and JET Contributors 2018 *Nuclear Fusion* **58** 056002

[36] Murari A, Lungaroni M, Gelfusa M, Peluso E, Vega J and JET Contributors 2019 *Nuclear Fusion* **59** 086037

[37] Rea C, Granetz R S, Montes K, Tinguely R A, Eidietis N, Hanson J M and Sammuli B 2018 *Plasma Physics and Controlled Fusion* **60** 084004

[38] Breiman L 2001 *Machine Learning* **45** 5–32

[39] Rea C, Montes K, Erickson K, Granetz R and Tinguely R 2019 *Nuclear Fusion* **59** 096016

[40] Murari A, Rossi R, Peluso E, Lungaroni M, Gaudio P, Gelfusa M, Ratta G, Vega J and and 2020 *Nuclear Fusion* **60** 056003

[41] Rea C and Granetz R S 2018 *Fusion Science and Technology* 1–12

[42] Rea C, Montes K J, Pau A, Granetz R S and Sauter O 2020 *Fusion Science and Technology* **76** 912–924

[43] Montes K J, Rea C, Tinguely R A, Sweeney R, Zhu J and Granetz R S 2021 *Nuclear Fusion* **61** 026022

[44] Hu W, Rea C, Yuan Q, Erickson K, Chen D, Shen B, Huang Y, Xiao J, Chen J, Duan Y, Zhang Y, Zhuang H, Xu J, Montes K, Granetz R, Zeng L, Qian J, Xiao B and Li J 2021 *Nuclear Fusion* **61** 066034

[45] de Vries P, Johnson M, Segui I and JET EFDA Contributors 2009 *Nuclear Fusion* **49** 055011

[46] Gerhardt S, Bell R, Diallo A, Gates D, LeBlanc B, Menard J, Mueller D, Sabbagh S, Soukhanovskii V, Tritz K and Yuh H 2013 *Nuclear Fusion* **53** 043020

[47] Lawless J F 2011 *Statistical Models and Methods for Lifetime Data* vol 362 (John Wiley & Sons)

[48] Olofsson K, Sammuli B and Humphreys D 2019 *Fusion Engineering and Design* **146** 1476–1479 sI:SOFT-30

[49] Igarashi Y, Ichikawa H, Nakanishi-Ohno Y, Takenaka H, Kawabata D, Eifuku S, Tamura R, Nagata K and Okada M 2018 *Journal of Physics: Conference Series* **1036** 012001

[50] Cortes C and Vapnik V 1995 *Machine learning* **20** 273–297

[51] Van Rijsbergen C 1979 *Information Retrieval* (Butterworths, London)

[52] George E I 2000 *Journal of the American Statistical Association* **95** 1304–1308

[53] Igarashi Y, Nagata K, Kuwatani T, Omori T, Nakanishi-Ohno Y and Okada M 2016 *Journal of Physics: Conference Series* **699** 012001

[54] Igarashi Y, Takenaka H, Nakanishi-Ohno Y, Uemura M, Ikeda S and Okada M 2018 *Journal of the Physical Society of Japan* **87** 044802

[55] Miyazawa J, Yasui K and Yamada H 2008 *Fusion Engineering and Design* **83** 265–268 proceedings of the 6th IAEA Technical Meeting on Control, Data Acquisition, and Remote Participation for Fusion Research

[56] Akiyama T, Kawahata K, Tanaka K, Tokuzawa T, Ito Y, Okajima S, Nakayama K, Michael C A, Vyacheslavov L N, Sanin A, Tsuji-Iio S and LHD Experiment Group 2010 *Fusion Science and Technology* **58** 352–363

[57] Murakami S, Nakajima N and Okamoto M 1995 *Fusion Technology* **27** 256–259

[58] Tsujimura T I, Kubo S, Takahashi H, Makino R, Seki R, Yoshimura Y, Igami H, Shimozuma T, Ida K, Suzuki C, Emoto M, Yokoyama M, Kobayashi T, Moon C, Nagaoka K, Osakabe M, Kobayashi S, Ito S, Mizuno Y, Okada K, Ejiri A and Mutoh T 2015 *Nuclear Fusion* **55** 123019

[59] Peterson B J, Kostrioukov A Y, Ashikawa N, Liu Y, Xu Y, Osakabe M, Watanabe K Y, Shimozuma T, Sudo S and the LHD Experiment Group 2003 *Plasma Physics and Controlled Fusion* **45** 1167–1182

[60] Sakakibara S, Yamada H and LHD Experiment Group 2010 *Fusion Science and Technology* **58** 471–481

[61] Oishi T, Morita S, Huang X, Zhang H, Goto M and the LHD Experiment Group 2015 *Plasma and Fusion Research* **10** 3402031–3402031

[62] Masuzaki S, Morisaki T, Ohyabu N, Komori A, Suzuki H, Noda N, Kubota Y, Sakamoto R, Narihara K, Kawahata K, Tanaka K, Tokuzawa T, Morita S, Goto M, Osakabe M, Watanabe T, Matsumoto Y, Motojima O and the LHD Experimental group 2002 *Nuclear Fusion* **42** 750–758

[63] Yamada I, Narihara K, Funaba H, Minami T, Hayashi H, Kohmoto T and LHD Experiment Group 2010 *Fusion Science and Technology* **58** 345–351

[64] Hirshman S and Betancourt O 1991 *Journal of Computational Physics* **96** 99–109

[65] Yamada H, Harris J, Dinklage A, Ascasibar E, Sano F, Okamura S, Talmadge J, Stroth U, Kus A, Murakami S, Yokoyama M, Beidler C, Tribaldos V, Watanabe K and Suzuki Y 2005 *Nuclear Fusion* **45** 1684–1693

[66] Tsujimura T I, Mizuno Y, Yanai R, Tokuzawa T, Ito Y, Nishiura M, Kubo S, Shimozuma T, Yoshimura Y, Igami H, Takahashi H, Tanaka K, Yoshinuma M and Ohshima S 2020 *Fusion Engineering and Design* **153** 111480

[67] Tsujimura T I, Yanai R, Mizuno Y, Tanaka K, Yoshimura Y, Tokuzawa T, Nishiura M, Sakamoto R, Motojima G, Kubo S, Shimozuma T, Igami H, Takahashi H, Yoshinuma M and Ohshima S 2021 *Nuclear Fusion* **61** 026012

[68] Yanai R, Tsujimura T, Kubo S, Yoneda R, Yoshimura Y, Nishiura M, Igami H, Takahashi H and Shimozuma T 2021 *Plasma and Fusion Research* **16** 2402084

[69] Fujii K, Goto M and Morita S 2015 *Nuclear Fusion* **55** 063029

[70] Tanaka K, Michael C A, Vyacheslavov L N, Sanin A L, Kawahata K, Akiyama T, Tokuzawa T and Okajima S 2008 *Review of Scientific Instruments* **79** 10E702

[71] Michael C A, Tanaka K, Vyacheslavov L, Sanin A and Kawahata K 2015 *Review of Scientific Instruments* **86** 093503

[72] Tanaka K, Ohtani Y, Nakata M, Warmer F, Tsujimura T, Takemura Y, Kinoshita T, Takahashi H, Yokoyama M, Seki R, Igami H, Yoshimura Y, Kubo S, Shimozuma T, Tokuzawa T, Akiyama T, Yamada I, Yasuhara R, Funaba H, Yoshinuma M, Ida K, Goto M, Motojima G, Shoji M, Masuzaki S, Michael C, Vacheslavov L, Osakabe M and Morisaki T 2019 *Nuclear Fusion* **59** 126040

[73] Ehmler H, Turkin Y, Beidler C, Maaßberg H, Dinklage A, Klinger T and W7-AS Team 2003 *Nuclear Fusion* **43** L11–L13

[74] Schirmer J, Conway G, Zohm H, Suttrop W and the ASDEX Upgrade Team 2006 *Nuclear Fusion* **46** S780–S791

[75] Horton W 1999 *Reviews of Modern Physics* **71** 735–778

[76] Riemann J, Kleiber R and Borchardt M 2016 *Plasma Physics and Controlled Fusion* **58** 074001

[77] Biglari H, Diamond P H and Terry P W 1990 *Physics of Fluids B: Plasma Physics* **2** 1–4

[78] Burrell K H, Allen S L, Bramson G, Brooks N H, Callis R W, Carlstrom T N, Chu M S, Colleraine A P, Content D, DeBoo J C, Dominguez R R, Ferron J R, Freeman R L, Gohil P, Greenfield C M, Groebner R J, Haas G, Heidbrink W W, Hill D N, Hinton F L, Hong R M, Howl W, Hsieh C L, Jackson G L, Jahns G L, James R A, Kellman A G, Kim J, Lao L L, Lazarus E A, Lehecka T, Lister J, Lohr J, Luce T C, Luxon J L, Mahdavi M A, Matsumoto H, Mayberry M, Moeller C P, Neyatani Y, Ohkawa T, Ohyabu N, Okazaki T, Osborne T H, Overskei D O, Ozeki T, Peebles A, Perkins S, Perry M, Petersen P I, Petrie T W, Philipona R, Phillips J C, Pinsker R, Politzer P A, Porter G D, Prater R, Rensink M E, Schaffer M J, Schissel D P, Scoville J T, Seraydarian R P, Shimada M, Simonen T C, Snider R T, Staebler G M, Stallard B W, Stambaugh R D, Stav R D, John H S, Stockdale R E, Strait E J, Taylor P L, Taylor T S, Trost P K, Stroth U, Waltz R E, Wolfe S M, Wood R D and Wroblewski D 1989 *Plasma Physics and Controlled Fusion* **31** 1649–1664

[79] Ida K and Hidekuma S 1990 *Physical Review Letters* **65** 1364–1367

[80] Masuzaki S, Shoji M, Tokitani M, Murase T, Kobayashi M, Morisaki T, Yonezu H, Sakamoto R, Yamada H and Komori A 2010 *Fusion Engineering and Design* **85** 940–945 proceedings of the 1st International Workshop on Lithium Applications for the Boundary Control in Fusion Devices

[81] Feng Y, Sardei F, Kisslinger J, Grigull P, McCormick K and Reiter D 2004 *Contributions to Plasma Physics* **44** 57–69

[82] Reiter D, Baelmans M and Börner P 2005 *Fusion Science and Technology* **47** 172–186

[83] Kawamura G, Tanaka H, Mukai K, Peterson B, Dai S Y, Masuzaki S, Kobayashi M, Suzuki Y, Feng Y and LHD Experiment Group 2018 *Plasma Physics and Controlled Fusion* **60** 084005

[84] Ida K and Hidekuma S 1989 *Review of Scientific Instruments* **60** 867–871

[85] Yokoyama M, Suzuki C, Seki R, Osakabe M, Yoshinuma M, Sato M, Wakasa A, Murakami S, Fukuyama A, Suzuki Y, Ida K, Lee H and LHD Experiment Group 2013 *Plasma and Fusion Research* **8** 2403016

[86] OPEN-ADAS https://open.adas.ac.uk/

[87] Oishi T, Morita S, Kobayashi M, Mukai K, Kawamura G, Masuzaki S, Hayashi Y, Suzuki C, Kawamoto Y, Goto M and the LHD Experiment Group 2021 *Plasma and Fusion Research* **16** 2402006–2402006

[88] Ishida S, Matsuoka M, Kikuchi M, Tsuji S, Nishitani T, Koide Y, Ozeki T, Fujita T, Nakamura H, Hosogane N *et al.* 1993 *PLASMA PHYSICS AND CONTROLLED NUCLEAR FUSION RESEARCH: Proceedings of 14th IAEA Fusion Energy Conference* **1** 219

[89] Taylor T S, Strait E J, Lao L L, Mauel M, Turnbull A D, Burrell K H, Chu M S, Ferron J R, Groebner R J, La Haye R J, Rice B W, Snider R T, Thompson S J, Wròblewski D and Lightly D J 1995 *Physics of Plasmas* **2** 2390–2396

[90] Sweeney R, Choi W, Haye R L, Mao S, Olofsson K and and F V 2016 *Nuclear Fusion* **57** 016019

[91] Howl W, Turnbull A, Taylor T, Lao L, Helton F, Ferron J and Strait E 1992 *Physics of Fluids B: Plasma Physics* **4** 1724–1734

[92] Matsunaga G, Shinohara K, Aiba N, Sakamoto Y, Isayama A, Asakura N, Suzuki T, Takechi M, Oyama N, Urano H *et al.* 2010 *Nuclear Fusion* **50** 084003

[93] Tokuda S and Watanabe T 1999 *Physics of Plasmas* **6** 3012–3026

[94] Takechi M, Matsunaga G, Aiba N, Fujita T, Ozeki T, Koide Y, Sakamoto Y, Kurita G, Isayama A and Kamada Y 2007 *Physical Review Letters* **98** 055002

[95] Miyoshi Y and Ogawa Y 2014 *Plasma and Fusion Research* **9** 1405015–1405015

[96] Luxon J 2002 *Nuclear Fusion* **42** 614–633

[97] Ninomiya H, Ando T, Horie T, Horiike H, Koizumi K, Kushima T, Matsukawa M, Neyatani Y and M Yamamoto 1990 *Plasma Devices and Operations* **1** 43–65

Related works

学術雑誌等に発表した論文

（査読有り）

1. Tatsuya Yokoyama, Takamitsu Sueyoshi, Yuya Miyoshi, Ryoji Hiwatari, Yasuhiko Igarashi, Masato Okada, and Yuichi Ogawa, "Disruption Prediction by Support Vector Machine and Neural Network with Exhaustive Search," Plasma and Fusion Research **13**, 3405021 (2018).

2. Tatsuya Yokoyama, Yuya Miyoshi, Ryoji Hiwatari, Akihiko Isayama, Go Matsunaga, Naoyuki Oyama, Yasuhiko Igarashi, Masato Okada, and Yuichi Ogawa, "Prediction of high-beta disruptions in JT-60U based on sparse modeling using exhaustive search," Fusion Engineering and Design **140**, 67–80 (2019).

3. Tatsuya Yokoyama, Hiroshi Yamada, Suguru Masuzaki, Junichi Miyazawa, Kiyofumi Mukai, Byron J. Peterson, Naoki Tamura, Ryuichi Sakamoto, Gen Motojima, Katsumi Ida, Motoshi Goto, Tetsutaro Oishi, and LHD Experiment Group, "Prediction of Radiative Collapse in Large Helical Device Using Feature Extraction by Exhaustive Search," Journal of Fusion Energy **39**, 500–511 (2020).

4. Tatsuya Yokoyama, Hiroshi Yamada, Suguru Masuzaki, Junichi Miyazawa, Kiyofumi Mukai, Byron J. Peterson, Naoki Tamura, Ryuichi Sakamoto, Gen Motojima, Katsumi Ida, Motoshi Goto, Tetsutaro Oishi, Gakushi Kawamura, Masahiro Kobayashi, and LHD Experiment Group, "Data-Driven Approach on the Mechanism of Radiative Collapse in the Large Helical Device," Plasma and Fusion Research **16**, 2402010 (2021).

5. Tatsuya Yokoyama, Hiroshi Yamada, Akihiko Isayama, Ryoji Hiwatari, Syunsuk Ide, Go Matsunaga, Yuya Miyoshi, Naoyuki Oyama, Naoto Imagawa, Yasuhiko Igarashi, Msato Okada, and Yuichi Ogawa,

"Likelihood identification of high-beta disruption in JT-60U," Plasma and Fusion Research **16**, 1402073 (2021).

6. Tatsuya Yokoyama, Hiroshi Yamada, Suguru Masuzaki, Byron J. Peterson, Ryuichi Sakamoto, Motoshi Goto, Tetsutaro Oishi, Gakushi Kawamura, Masahiro Kobayashi, Toru Ii Tsujimura, Yoshinori Mizuno, Junichi Miyazawa, Kiyofumi Mukai, Naoki Tamura, Gen Motojima, and Katsumi Ida, "Data-driven Control for Radiative Collapse Avoidance in Large Helical Device," Plasma and Fusion Research, *under review.*

（査読なし）

1. Tatsuya Yokoyama, Takamitsu Sueyoshi, Yuya Miyoshi, Ryoji Hiwatari, Akihiko Isayama, Go Matsunaga, Naoyuki Oyama, Yasuhiko Igarashi, Masato Okada, and Yuichi Ogawa, "Disruption prediction with sparse modeling by exhaustive search," The 45th European Physical Society Conference on Plasma Physics, P2.1079 (2018).

2. 若月 琢馬，横山 達也，大山 直幸，山田 弘司，「プラズマ・インフォマティクス-データ駆動科学のプラズマへの応用 4. トカマクプラズマ運転への応用展開」，プラズマ・核融合学会誌 **95**，548–553 (2019).

招待講演

1. ◯Tatsuya Yokoyama, Hiroshi Yamada, Suguru Masuzaki, Byron J. Peterson, Ryuichi Sakamoto, Motoshi Goto, Tetsutaro Oishi, Gakushi Kawamura, Masahiro Kobayashi, Toru Ii Tsujimura, Yoshinori Mizuno, Junichi Miyazawa, Kiyofumi Mukai, Naoki Tamura, Gen Motojima, and Katsumi Ida, "Data-driven prediction of radiative collapse for avoidance in fusion plasmas," 1st Workshop on Artificial Intelligence in Plasma Science, hybrid (Aix-en-Provence, France and online), September 2021.

2. ◯Tatsuya Yokoyama, Hiroshi Yamada, Suguru Masuzaki, Byron J. Peterson, Ryuichi Sakamoto, Motoshi Goto, Tetsutaro Oishi, Gakushi Kawamura, Masahiro Kobayashi, Toru Ii Tsujimura, Yoshinori Mizuno, Junichi Miyazawa, Kiyofumi Mukai, Naoki Tamura, Gen Motojima, and Katsumi Ida, "Data-driven prediction and control of radiative collapse in stellarator-heliotron plasmas," 5th Asia Pacific Conference on Plasma Physics, MF1-I40, online, September 2021.

国際会議における発表

口頭発表，査読なし

1. ◯Tatsuya Yokoyama, Yuya Miyoshi, Ryoji Hiwatari, Akihiko Isayama, Go Matsunaga, Naoyuki Oyama, Yasuhiko Igarashi, Masato Okada, Naoto Imagawa, Yuichi Ogawa, and Hiroshi Yamada, “Data-driven study of high-beta disruption prediction in JT-60U using exhaustive search,” 3rd Asia-Pacific Conference on Plasma Physics, MF2-O41, Hefei, China, November 2019.

2. ◯Tatsuya Yokoyama, Hiroshi Yamada, Suguru Masuzaki, Junichi Miyazawa, Kiyofumi Mukai, Byron J. Peterson, Naoki Tamura, Ryuichi Sakamoto, Gen Motojima, Katsumi Ida, Motoshi Goto, Tetsutaro Oishi, Masahiro Kobayashi, Gakushi Kawamura, and LHD experiment group, “Feature extraction and prediction of radiative collapse in Large Helical Device using sparse modeling,” 4th Asia-Pacific Conference on Plasma Physics, MF2-O13, online, Octover 2020.

3. ◯Tatsuya Yokoyama, Hiroshi Yamada, Suguru Masuzaki, Junichi Miyazawa, Kiyofumi Mukai, Byron J. Peterson, Naoki Tamura, Ryuichi Sakamoto, Gen Motojima, Katsumi Ida, Motoshi Goto, Tetsutaro Oishi, Masahiro Kobayashi, Gakushi Kawamura, and LHD experiment group, “Feature extraction and likelihood estimation of radiative collapse in Large Helical Device using sparse modeling,” 3rd International Conference on Data-Driven Plasma Science, O-2, online, March 2021.

4. ◯Tatsuya Yokoyama, Hiroshi Yamada, Suguru Masuzaki, Byron J. Peterson, Ryuichi Sakamoto, Motoshi Goto, Tetsutaro Oishi, Gakushi Kawamura, Masahiro Kobayashi, Toru Ii Tsujimura, Yoshinori Mizuno, Junichi Miyazawa, Kiyofumi Mukai, Naoki Tamura, Gen Motojima, and Katsumi Ida, “Data-driven control for radiative collapse avoidance in Large Helical Device,” The 30th International Toki Conference on Plasma and Fusion Research, 17Be6, online, November 2021.

ポスター発表，査読あり

1. ◯Tatsuya Yokoyama, Hiroshi Yamada, Suguru Masuzaki, Junichi Miyazawa, Kiyofumi Mukai, Byron J. Peterson, Naoki Tamura, Ryuichi Sakamoto, Gen Motojima, Katsumi Ida, Motoshi Goto, Tetsutaro Oishi, and LHD experiment group, “Characterization and sparse modeling of ra-

diation collapse and density limit in LHD," 28th IAEA Fusion Energy Conference, EX/P6-21, online, May 2021.

ポスター発表，査読無し

1. ◯Tatsuya Yokoyama, Takamitsu Sueyoshi, Yuya Miyoshi, Ryoji Hiwatari, Yasuhiko Igarashi, Masato Okada, and Yuichi Ogawa, "Disruption prediction by Deep Neural Network with Exhaustive Search," Plasma Conference 2017, 23P-106, Himeji, Japan, November 2017.

2. ◯Takamitsu Sueyoshi, Tatsuya Yokoyama, Yuya Miyoshi, Ryoji Hiwatari, Yasuhiko Igarashi, Masato Okada, and Yuichi Ogawa, "An Exhaustive Search with Support Vector Machine for Prediction of Disruption," Plasma Conference 2017, 23P-107, Himeji, Japan, November 2017.

3. ◯Tatsuya Yokoyama, Takamitsu Sueyoshi, Yuya Miyoshi, Ryoji Hiwatari, Yasuhiko Igarashi, Masato Okada, and Yuichi Ogawa, "Disruption prediction by Support Vector Machine and Neural Network with Exhaustive Search," Joint meeting of the 26th International Toki Conference and the 11th Asia Plasma and Fusion Association Conference, P2-044, Toki, Japan, December 2017.

4. ◯Tatsuya Yokoyama, Takamitsu Sueyoshi, Yuya Miyoshi, Ryoji Hiwatari, Akihiko Isayama, Go Matsunaga, Naoyuki Oyama, Yasuhiko Igarashi, Masato Okada, and Yuichi Ogawa, "Disruption prediction with sparse modeling by exhaustive search," The 45th European Physical Society Conference on Plasma Physics, P2.1079, Prague, Czech Republic, July 2018.

5. ◯Tatsuya Yokoyama, Takamitsu Sueyoshi, Yuya Miyoshi, Ryoji Hiwatari, Akihiko Isayama, Go Matsunaga, Naoyuki Oyama, Yasuhiko Igarashi, Masato Okada, Hiroshi Yamada, and Yuichi Ogawa, "Feature extraction using exhaustive search in disruption prediction based on JT-60U experimental data," 2nd International Conference on Data Driven Plasma Science, P1.11, Marseille, France, May 2019.

6. ◯Tatsuya Yokoyama, Hiroshi Yamada, Suguru Masuzaki, Junichi Miyazawa, Kiyofumi Mukai, Byron J. Peterson, Naoki Tamura, and LHD experiment group, "Data-driven study on density limit and radiation collapse in stellarator-heliotron plasmas on LHD," 61st Annual Meeting of the APS Division of Plasma Physics, GP10.67, FL, the US, October 2019.

7. ◯Tatsuya Yokoyama, Yuya Miyoshi, Ryoji Hiwatari, Akihiko Isayama, Go Matsunaga, Naoyuki Oyama, Yasuhiko Igarashi, Masato Okada, Naoto

Imagawa, Yuichi Ogawa, and Hiroshi Yamada, “Applied study of feature extraction using exhaustive search on high-beta disruption in JT-60U,” 3rd Asia-Pacific Conference on Plasma Physics, MF-P13, Hefei, China, November 2019.

8. ◯Tatsuya Yokoyama, Hiroshi Yamada, Suguru Masuzaki, Junichi Miyazawa, Kiyofumi Mukai, Byron J. Peterson, Naoki Tamura, Ryuichi Sakamoto, Gen Motojima, Katsumi Ida, Motoshi Goto, Tetsutaro Oishi, Masahiro Kobayashi, Gakushi Kawamura, and LHD experiment group, “Data-driven approach on the mechanism of radiative collapse in Large Helical Device,” The 29th International Toki Conference on Plasma and Fusion Research, Poster-2-F2-7, online, October 2020.

9. ◯Tatsuya Yokoyama, Hiroshi Yamada, Suguru Masuzaki, Junichi Miyazawa, Kiyofumi Mukai, Byron J. Peterson, Naoki Tamura, Ryuichi Sakamoto, Gen Motojima, Katsumi Ida, Motoshi Goto, Tetsutaro Oishi, Masahiro Kobayashi, Gakushi Kawamura, and LHD experiment group, “Interpretation and application of extracted features of radiative collapse in Large Helical Device with sparse modeling,” 62nd Annual Meeting of the APS Division of Plasma Physics, JP20.8, online, November 2020.

国内学会・シンポジウム等における発表

口頭発表，査読無し

1. ◯横山 達也, 山田 弘司, 増崎 貴, 宮澤 順一, 向井 清史, Byron J. Peterson, 田村 直樹，坂本 隆一，本島 巌，LHD実験グループ,「LHDにおける放射崩壊のデータ駆動型アプローチによる特徴抽出と密度限界モデルの構築」，第36回プラズマ・核融合学会年会，30Aa07，春日井，2019年11月.

2. ◯横山 達也, 山田 弘司, 増崎 貴, 宮澤 順一, 向井 清史, Byron J. Peterson, 田村 直樹，坂本 隆一，本島 巌，居田 克巳，後藤 基志，大石 鉄太郎，LHD実験グループ,「LHDにおける放射崩壊と密度限界のデータ駆動型研究」，日本物理学会第75回年次大会，16pD11-10，現地開催中止（要旨掲載のみ），2020年3月.

3. ◯横山 達也, 山田 弘司, 増崎 貴, 宮澤 順一, 向井 清史, Byron J. Peterson, 田村 直樹，坂本 隆一，本島 巌，居田 克巳，後藤 基志，大石 鉄太郎，小林 政弘，河村 学思，LHD実験グループ，「LHDにおける放射崩壊の予知と物理背景のデータ駆動型研究」，日本物理学会2020年秋季大会，9pB2-13，オンライン，2020年9月.

4. ◯横山 達也，山田 弘司，増崎 貴，宮澤 順一，向井 清史，Byron J. Peterson，田村 直樹，坂本 隆一，本島 厳，居田 克巳，後藤 基志，大石 鉄太郎，河村 学思，小林 政弘，LHD 実験グループ，「データ駆動アプローチを用いた大型ヘリカル装置における放射崩壊の発生予知と発生過程の研究」，第 37 回プラズマ・核融合学会年会，03Ep05，オンライン，2020 年 12 月.
5. ◯横山 達也，山田 弘司，増崎 貴，宮澤 順一，向井 清史，Byron J. Peterson，田村 直樹，坂本 隆一，本島 厳，居田 克巳，後藤 基志，大石 鉄太郎，小林 政弘，河村 学思，LHD 実験グループ，「データ駆動アプローチとシミュレーションを合わせた放射崩壊前駆現象の考察」，日本物理学会第 76 回年次大会，13pB2-8，オンライン，2021 年 3 月.
6. ◯横山 達也，山田 弘司，増崎 貴，Byron J. Peterson，坂本 隆一，後藤 基志，大石 鉄太郎，河村 学思，小林 政弘，辻村 亨，水野 嘉識，宮澤 順一，向井 清史，田村 直樹，本島 厳，居田 克巳，「データ駆動型アプローチを用いた大型ヘリカル装置における放射崩壊の予知と回避」，第 38 回プラズマ・核融合学会年会，24Cp02，オンライン，2021 年 11 月.

ポスター発表，査読無し

1. ◯横山 達也，末吉 孝充，三善 悠矢，日渡 良爾，諫山 明彦，松永 剛，大山 直幸，五十嵐 康彦，岡田 真人，小川 雄一，「全状態探索による特徴抽出を用いたディスラプション予知」，第 12 回核融合エネルギー連合講演会，28P-76，滋賀，2018 年 6 月.
2. ◯横山 達也，三善 悠矢，日渡 良爾，諫山 明彦，松永 剛，大山 直幸，五十嵐 康彦，岡田 真人，今川 直人，小川 雄一，「全状態探索によるデータ駆動アプローチを用いた JT-60U の高ベータディスラプション予知と物理背景の抽出」，第 35 回プラズマ・核融合学会年会，3P48，大阪，2018 年 12 月.

受賞歴

1. 先端エネルギー工学優秀賞，東京大学大学院新領域創成科学研究科先端エネルギー工学専攻修士論文，2019 年 3 月.
2. 第 36 回プラズマ・核融合学会年会 若手学会発表賞（学生会員部門），2019 年 12 月.
3. 2020 年秋季大会 日本物理学会学生優秀発表賞，2020 年 10 月.
4. 第 76 回年次大会（2021 年） 日本物理学会学生優秀発表賞，2021 年 3 月.

Acknowledgement

First of all, I would like to express my deepest appreciation to Prof. Hiroshi Yamada, my supervisor. He taught me not only knowledge of plasma physics and experiment but also how a researcher should be. I really appreciate his patient support through my Ph.D. course.

I would also like to thank Prof. Yuichi Ogawa, who was my supervisor in the master course. He taught me the fundamental of plasma physics and fusion engineering.

In the radiative collapse study in LHD, I highly appreciate all of my collaborators at National Institute for Fusion Science (NIFS). Especially, discussions with Prof. Suguru Masuzaki, Prof. Masahiro Kobayashi, Prof. Motoshi Goto, Prof. Gakushi Kawamura, and Prof. Katsumi Ida were fruitful. Prof. Ryuichi Sakamoto helped me a lot with everything about using LHD experiment data and doing experiments in LHD. I am also indebted to Prof. Kenji Tanaka for using the 2D-PCI measurement data. In addition, I thank Prof. Toru Tsujimura, Mr. Yoshinori Mizuno, and Mr. Kazuki Nagahara for their kind cooperation in the collapse avoidance control experiment.

I would like to express my appreciation to Dr. Yuki Okamoto in National Institute of Advanced Industrial Science and Technology for his great advice for developing the collapse avoidance control system. I am also particularly grateful to Dr. Keisuke Fujii at Kyoto University for his kind cooperation in using a neutral diffusion model.

I am deeply grateful to Dr. Akihiko Isayama, Dr. Go Matsunaga, Dr. Naoyuki Oyama, and Dr. Shunsuke Ide in Naka fusion institute, QST for their kind support in the study on disruption in JT-60U. Also, I would like to thank Dr. Yuya Miyoshi and Dr. Ryoji Hiwatari for their cooperation in starting the disruption prediction study.

Dr. Edward Strait took care of my visit in General Atomics (GA) and study on disruption in DIII-D. I would like to thank him deeply. I regret that I have had no chance to visit GA again because of COVID-19 pandemic.

I would also like to express my appreciation to Prof. Masato Okada at the University of Tokyo and Prof. Yasuhiko Igarashi at Tsukuba University for teaching me about machine learning and sparse modeling. This work could not be without their support.

I would like to thank the past and present members of the Yamada and Ogawa laboratories and all my friends. Thanks to them, my life in the Kashiwanoha campus has been enriched both in research and personal life.

Finally, I am deeply grateful to my family for their kind support and encouragement through my Ph.D. course.